MULTIPLE SCATTERING SUPPRESSION APPLIED TO PARTICLE SIZING IN NON-FLOWING AND FLOWING MEDIA

By

SANJAY SUNDARESAN

Bachelor of Engineering

Manonmaniam Sundaranar University

Tirunelveli, India

1997

Submitted to the Faculty of the
Graduate College of the
Oklahoma State University
in partial fulfillment of
the requirements for
the Degree of
MASTER OF SCIENCE
December, 1999

MULTIPLE SCATTERING SUPPRESSION

APPLIED TO PARTICLE SIZING

IN NON-FLOWING AND

FLOWING MEDIA

Thesis Approved:

Ronald L. Daugherty
Thesis Adviser

H. J. Yhaja

B

Wayne B. Powell
Dean of the Graduate College

ACKNOWLEDGEMENTS

I wish to express my sincere and deep appreciation to my adviser, Dr. Ronald L. Dougherty, for his intelligent supervision, constructive guidance, encouragement and support. He is a man that I truly admire and respect. He has been a role model for me during my stay at OSU. He cares for his students not only in the academic context, but also outside of school. I still remember the night my car ran out of gas, and how he helped me and my companions get back on our way that night. His generous support throughout my stay here is immeasurable. I consider myself very fortunate to have him as my adviser. I have best wishes for him.

I would also like to thank my research adviser, Dr. Bruce J. Ackerson, for his guidance in this project. He has been around always to help me whenever I had a problem on the project that was too difficult for me to handle. I would like to thank him for his generous support during the last year. Without his immense knowledge and "magic touch", my research would never have tasted this success.

I would also like to thank Dr. Afshin J. Ghajar for setting on my thesis committee. I will cherish the memories of the class I took with him. I remember him saying, "One bad performance does not mean the end. Even the best have a bad day", when I was going through a bad phase one semester. His words of encouragement put me back on the track to success.

I wish to express my sincere gratitude to my colleagues, Ulf Nobbmann, Dorri-

Nowkoorani, Kiley Benes, and Ryan Cambern. Ulf was my mentor when I started working on this project, and transformed me from a novice to a person capable of finishing this project. I would like to make a special mention of Ryan, who has been my partner on this project for the last two years. He has been a caring, hardworking and a very intelligent partner, and has been by me and lived through my complaints whenever I had problems. I will always remember his apt sense of humor, and will cherish the memories of the conversations we have had. Even in the greatest of fortunes, I could not have asked for a better partner.

I would like to thank the entire faculty and staff at the School of Mechanical and Aerospace Engineering for having contributed to my successful stay at OSU. My special appreciation goes to Ms. Janet Smith and Ms. Sarah Wells, who have always been there to support me. Their constant encouragement has been a significant factor to the success of this research.

Next, I would like to thank my friends Suraj Bhat and Rajesh Krishnamoorthy. They have been my best friends during the last year. Their help and words of encouragement "If you can't do it, nobody can", helped me complete my thesis successfully. All of the help rendered by the duo is greatly appreciated.

I would like to express my greatest appreciation for my parents, who have been loving and supportive of me throughout my life. Without them, I would never have made it this far. Their ideals of no compromise on perfection, and their encouragement, love and support have been greatly responsible for all of the success I have had in my life. I love them, and I dedicate this thesis to my parents.

I thank God for all his blessings, protection, and kindness. May God bless us all.

TABLE OF CONTENTS

LIST OF TABLES

LIST OF FIGURES

Figure Page

Figure Page

Figure Page

Figure Page

Figure Page

NOMENCLATURE

A	amount of multiple scattering
B	amount of single scattering
D_h	hydraulic diameter of the flowing fluid test cell (mm or m)
D_o	diffusion constant of particles (m^2/s)
E	magnitude of the electric field (N/C)
E*	complex conjugate of the electric field (N/C)
f	focal length of the lens (mm)
g^1	normalized electric field correlation function
g^2	normalized intensity correlation function
h	height of the flow test cell (mm)
i	complex number ($\sqrt{-1}$)
I	intensity ($W/m^2/K^4$ and kHz in experiments)
j	second constant used for a two cumulant fit
k_B	Boltzmann constant (1.380658×10^{-23} J/°K)
k_i	magnitude of the incident beam wave vector (m^{-1})
k_s	magnitude of the scattered beam wave vector (m^{-1})
$\vec{\mathbf{k}}_i$	incident beam wave vector (m^{-1})
$\vec{\mathbf{k}}_s$	scattered wave vector (m^{-1})
l*	effective transport mean free path (μm)
Le_v	hydrodynamic entrance length (mm)
n	index of refraction
n_W	index of refraction of water (1.33)
n_A	index of refraction of air (1.0)
np	number of particles with which the viewed particle interacts
Np	number of particles in the detection volume
P	particle form factor
q	magnitude of the scattering wave vector (resultant between incident and scattered wave vectors) (m^{-1})
$\vec{\mathbf{q}}$	scattering wave vector (m^{-1})
$\dot{Q}$	flow rate (m^3/s)
r	magnitude of a spatial position vector (m)
$\vec{\mathbf{r}}$	spatial position vector (m)
r_p	radius of the particle (m)
Re_{Dh}	Reynolds number ($=\rho D_h v_{avg}/\mu$)
$\vec{\mathbf{s}}$	unit vector (m)
t	correlation time (ms)
T	absolute temperature (K)

T_e	total experiment run time (s)
u	first constant used for a two cumulant fit
$\bar{\mathbf{v}}$	fluid velocity vector (mm/s)
v_{avg}	fluid velocity (mm/s)
$v_{centerline}$	centerline fluid velocity (mm/s)
w	width of the test cell (mm)
w_f	radius of focused beam (mm)
w_0	radius of incident laser beam (mm)
X	denotes translation of the top fiber mount in the x-direction
Y	denotes translation of the top fiber mount in the y-direction

Greek

α	angle through which the laser (α_L) and detector (α_D) may travel (degrees or radians)
α_t	inverse of the square of the detection cylinder radius (m^{-2})
β	angle (β_L for laser and β_D for detector) used in calculation of θ for the flowing fluid setup (degrees)
β_t	inverse of the square of the focused beam radius (m^{-2})
γ	complex degree of coherence
γ^2	signal-to-noise ratio or Y-intercept
Γ	decay rate (ms^{-1})
δ	rotation angle of test cell for flow measurement setup (degrees or radians)
δ_t	inverse of the square of the radius of the multiple scattering area (m^{-2})
η	kinematic viscosity of the sample solvent (m^2/s)
θ	scattering angle (degrees or radians)
κ	experimental proportionality constant in DWS backscattering model
λ	wavelength of the incident laser beam (nm)
μ	dynamic viscosity (Pa-s)
π	numerical constant (3.1415926…)
ρ	fluid density (kg/m^3)
τ	correlation delay time (ms)
$\tau_{Doppler}$	time between fluctuations of two particles moving at different velocities (ms)
ϕ	tilt angle (degrees or radians)

Abbreviations

BM	denotes back micrometer for top fiber mount
CT	correlation transfer theory
DLS	dynamic light scattering
DWS	diffusing wave spectroscopy
FM	denotes front micrometer for top fiber mount
FOQELS	fiber optic quasi-elastic light scattering

GRIN	graded-index lenses
He-Ne	helium neon
KCl	potassium chloride
Nd: YAG	neodymium-yttrium-silver
PMMA	polymethylmethacrylate
PMT	photomultiplier tube
PSL	polystyrene latex
RT	radiative transfer theory
S/N	signal-to-noise ratio

Subscripts

L	laser arm
D	detector arm

Superscripts

1	electric field correlation function
2	intensity correlation function

CHAPTER I

INTRODUCTION

1.1 Background

It is important to be able to determine and control the size of micron size particles in a wide variety of industrial applications. Examples of such industrial applications include pharmaceutical drugs, paints, and fuel/oil filters [Dorri-Nowkoorani (1995)]. Pharmaceutical drugs are required to meet standards of drug content uniformity and quality. This ensures that the product will deliver the intended dose, thereby achieving the desired effects. To achieve a well-dispersed system, the drug material must be reduced to a very fine particle diameter. Regarding paint applications, properties of pigment dispersions such as penetration, stability and film-forming ability are critically controlled by the diameter of the constituent particles. Companies which produce filtering systems, such as automobile fuel/oil filters, need to be able to measure the particle sizes as well as concentrations in order to determine the efficiency of the filters as a function of particle diameter.

There are four types of techniques by which particle sizing is done. They are off-line, on-line, in-line and in-situ testing [Dorri-Nowkoorani (1995)]. The first three types have procedural limitations in them. These include a necessity to remove the sample from the process and to investigate it in the laboratory, or to allow a sample taken from a flowing system to stagnate prior to analysis, or to dilute the sample. These limitations bring into question the validity of the techniques because of the differences that may exist between the analysis environment and the actual manufacturing environment; and hence lead to the argument that such results may not be representative of the actual process. The fourth type of technique, viz., in-situ testing, is by far the better of the four because it can be a non-intrusive testing method.

One form of in-situ, non-intrusive testing makes use of the theory of Dynamic Light Scattering (DLS) [Berne and Pecora (1976)]. Scattering occurs when a light beam interacts with a particle. Depending upon the circumstances, two types of scattering can occur. When the incident light beam is scattered by only one particle in the medium before it leaves the medium, the phenomenon is called single scattering. When the incident light beam is scattered by more than one particle in the medium before it leaves the medium, the phenomenon is called multiple scattering. Usually both types of scattering occur together, but multiple scattering is more dominantly observed in most industrial applications. There is a well-developed theory that can interpret single scattering data and predict the particle size accurately [Berne and Pecora (1976)]. But multiple scattering data is more difficult to interpret [Lock (1997a)]. Multiple scattering must be eliminated or substantially suppressed [Weise and Horn (1991)] in order to enable accurate data interpretation with the well developed single scattering theory. Otherwise, there must be a reliable multiple scattering theory [Dorri-Nowkoorani *et al.* (1993)] that can be implemented with reasonable ease in the laboratory.

Many techniques have been developed that can eliminate or reduce the effects of multiple scattering. Some of these techniques make use of a two-color laser beam system [Schätzel *et al.* (1990)], or a 3-D cross-correlation system [Aberle *et al.* (1998)], which are very difficult to align and are very expensive. Meyer *et al.* (1997a and 1997b) developed a simple technique for multiple scattering suppression by making use of a single laser beam and two slightly separated detectors; and the cross-correlation of the two signals showed substantial suppression of multiple scattering. This technique was experimentally verified and proved effective by those authors. Nobbmann *et al.* (1997) experimentally verified that the technique proposed by Meyer *et al.* (1997a and 1997b) followed the proposed theory, by experimenting on static (non-flowing) samples at two different volume fractions.

1.2 Objectives

The first major objective of this research was to continue the work done by Nobbmann *et al.* (1997) in the static case, by experimenting with different particle sizes, volume fractions, scattering angles and sample cell cross-sections, in order to determine the effects of these parameters on the accuracy of the results obtained. Studies were also done to verify the accuracy of the theoretical prediction of the signal-to-noise (S/N) ratio [Nobbmann *et al.* (1997)], by comparing the theoretical S/N ratio with experimental data. The second major objective was to extend the theory of multiple scattering suppression to flowing media. Experiments were also performed to determine the effects of particle size, flow rate, position of the detection volume within the test cell, tilt of the test cell, and scattering angle.

A brief review of the work done by other researchers in the areas of multiple scattering suppression and flow suppression will be provided in Chapter II. A list of references will be provided so that the reader can investigate further if desired. To implement the first objective, the theory behind multiple scattering suppression will be discussed in Chapter III. A brief mention of the flow suppression theory will also be made. Chapter IV will discuss the experimental setup for the static system. The equipment used for the experiments, the systematic alignment procedure, and the experimental procedure will be explained.

Chapter V will focus on the second objective of multiple scattering suppression in flowing systems. The experimental setup, the alignment procedure and the experimental procedure will be explained.

A detailed discussion of the results of the experiments performed in pursuit of both objectives will follow in Chapter VI. Work done in verifying the accuracy of the theoretical prediction of the S/N ratio by using the experimental data will also be presented. And finally, in Chapter VII, some recommendations regarding future work that can be done will be given.

CHAPTER II

LITERATURE REVIEW

2.1 Introduction

The research of interest in this paper consists of two aspects, viz., multiple scattering suppression and flow suppression. In this chapter, a brief review of work done by several researchers in the two areas will be provided. As outlined in Chapter I, multiple scattering is very complex and has to be eliminated or substantially suppressed in order to interpret data accurately with the single scattering theory. Alternatively, a well developed multiple scattering theory must exist, that can accurately interpret multiple scattering data and predict particle sizes accurately.

The second section of this chapter will discuss the previous work that has been done in multiple scattering suppression. The technique described in this section, however, is not the technique used in this research. Also discussed will be the work done in developing a technique that, instead of suppressing multiple scattering, makes use of it in order to characterize particles.

The third section of this chapter will discuss the one-beam and two-detector cross-correlation technique of multiple scattering suppression used in this research. A review of work done using this technique by three researchers will be provided.

The fourth section of this chapter will discuss the second aspect of this research, viz., flow suppression. References will be provided so that the reader can investigate further if desired.

2.2 Multiple Scattering

Multiple scattering, which occurs predominantly when laser light passes through a dense sample, interferes with the interpretation of the data using the well-developed single scattering theory. A number of researchers have worked for years in this area and have studied how multiple scattering affects particle characterization and how to overcome the difficulties.

Phillies (1981) was the first to show that a cross-correlation technique can be used to suppress multiple scattering. He showed theoretically that, for strongly scattering fluids, multiple scattering has a smaller effect on the two-detector cross-correlation spectrum than on the single-detector auto-correlation spectrum. He first considered a single-beam, single-detector geometry and derived the intensity of the singly and doubly scattered light. He then considered a two-beam, two-detector geometry, and derived the single and double scattered intensities. He concluded that the double scattering contribution to the cross-correlation function is less than the contribution to the auto-correlation function by a factor of $(np/Np)^2$, where Np is the number of particles in the scattering volume, and np is the number of particles interacting with a given particle. He described several experimental considerations regarding the two-detector experiment:

1. The scattering vector defined by the two beam-detector combinations must be the same, requiring beam alignment to be within 0.5 mrad.
2. The placement and orientation of the focusing and collecting lenses must be

exact in order to prevent spherical wavefronts of the incident or scattered waves from forming inside the scattering volume.

3. A second scattering vector may be produced if the photons are scattered into the wrong detector. If two lasers of different wavelengths are used, appropriate interference filters should be placed in front of the two detectors, so that each detector will be sensitive to light scattered through a unique scattering vector.

Dhont and de Kruif (1983) developed a scheme to correct static and dynamic light scattering data for double scattering. They also described how Phillies overlooked a second order term for double scattering. They developed expressions for the field strength of higher order scattered light and made a rigorous theoretical treatment of the cross-correlation experiment. They concluded that in first order, the same correlation function is obtained in both the auto- and cross-correlation setup. Up to the second order of scattering, the cross-correlation function is essentially the first order function, i.e., the double scattering does not contaminate the experimental cross-correlation function. The intensity auto-correlation function however may be affected considerably by double scattering events. They also noted that experimentally, the cross-correlation technique could only be used at a 90° scattering angle. Otherwise, one would have to use two lasers with different wavelengths and position the two detectors at different scattering angles, which would make it very difficult to align both the lasers and the detectors properly.

Mos *et al.* (1986) described the experimental setup that they used to verify the theory of multiple scattering suppression by Dhont and de Kruif (1983). The experimental setup consisted of one laser beam operating at a wavelength of 514.5 nm.

The beam was split into two beams of equal intensity using a cube beam-splitter. The scattered signal was fed to the two detectors facing each other at scattering angles of 90° and 270° with respect to either beam. The alignment procedure was described. They fitted all correlation functions with a single exponential function and a second cumulant to account for polydispersity. They used polystyrene latex particles of 176 nm diameter suspended in water with concentrations ranging from 0.005 to 0.1 g/cc. Also used were stable, non-aqueous dispersions of monodisperse spherical silica particles in xylene and toluene with concentrations ranging from 0.005 to 0.2 g/cc. Experimental results showed that, for samples with turbidity beyond 0.1 cm^{-1}, the auto-correlation functions were not a single exponential, and the cumulants were of the order of 0.10. When the signals were cross-correlated, the correlation functions were exponential, and the cumulants were of the order of 0.01, showing the effectiveness of the cross-correlation technique in suppressing multiple scattering effects.

Brown (1987) describes the effectiveness of using monomode optical fibers in Dynamic Light Scattering (DLS) over a conventional light scattering apparatus. A single mode fiber propagates a pure mode of light without significant degradation of spatial coherence. The experimental setup that Brown used to demonstrate the usefulness of monomode fibers consisted of a Helium-Neon laser operating at a wavelength of 633 nm. The beam was transmitted through 1 m of York VSOP Hi-birefringence polarization preserving monomode optical fiber. The light was passed through a sample cell containing a monodisperse suspension of polystyrene spheres of diameter 0.27 μm and at a concentration of approximately 10^5 $mliter^{-1}$. At a scattering angle of 90°, a monomode fiber of identical specifications to the first fiber was used, and its other end was connected to a PMT. The results were compared to the experiments he conducted using a conventional DLS apparatus fitted with Pusey optics [Brown (1987)]. The correlogram slopes were found to match and the $g^2(0)$ value was found to be consistently higher, testifying to the fiber's spatial filtering ability. He concluded by discussing some applications of single mode fibers in DLS.

Schätzel *et al.* (1990) devised a dual-color cross-correlation technique of multiple scattering suppression that overcame the limitation of the technique used by Phillies (1981), in that this technique was not limited to a scattering angle of 90°. The setup consisted of an argon-ion laser that operated at both the 488 nm and 514 nm wavelengths, a dichroitic double köster's prism to separate the two wavelengths, lenses and optical fibers connected to two PMTs. They used a sample of polystyrene latex spheres (49.2 nm radius) in a KCl solution (5-mmol l^{-1}) at a volume fraction of 0.0028. The experimental results showed a strong curvature in the logarithmic plot of the g^1 function for the auto-correlation, and particle sizes 20% lower than the actual values. The dual color cross-correlation yielded an almost perfect single exponential, and produced particle sizes within 2% accuracy. Measurements at higher volume fractions (up to 0.01) yielded similar results.

Wiese and Horn (1991) showed the effectiveness of single mode fibers in Fiber Optic Quasi-Elastic Light Scattering (FOQELS). They used a single mode fiber to transmit laser light into the sample. The same fiber transmitted backscattered light to the detectors. Thus, the path that the light had to travel within the dispersion was very short. This feature suits FOQELS ideally for studying the dynamics of concentrated systems. They used a helium-neon laser operating at a wavelength of 632.8 nm, and a single mode optical fiber with a core diameter of 4 μm and a numerical aperture of 0.1, which gives a cutoff wavelength of 523 nm. Polymer latex suspensions of size 41 to 326 nm diameter were tested, with concentrations ranging from 1 to 40% by weight. They found experimentally that, with increasing concentration, the decay rate of the 41 and 63 nm particles increased considerably. The decay rate of the 115 nm particles remained unaffected by changes in concentration up to 30%, but then dropped off. The decay rates of the 199 and 326 nm particles decreased with increased concentration. The reason for the deviation from the single exponential behavior at higher concentrations has been cited as due to the non-Gaussian behavior of particle displacements at higher concentrations. It is surprising that, at the extremely high volume fractions used, particles diffused to enable light scattering measurements.

Aberle *et al.* (1998) discussed the principle, design and operation of a 3-D cross-correlation setup to suppress multiple scattering effects. Their experimental setup made use of a helium-neon laser operating at a wavelength of 632.8 nm, and a beam splitter/mirror arrangement to split the beams into two parallel beams of equal intensity. The two beams were separated by a tilt of 2.4°. The beams were focused into the sample by an achromatic corrected lens with a focal length of 16 cm. On the detection side, two monomode fibers and a mirror were aligned to ensure that they received light from scattering processes with equal scattering vectors. They claimed that the alignment was critical and difficult. Experiments were performed on monodisperse suspensions of polystyrene latex particles in deionized water. The particle diameters were 69 (with unspecified error), 107 ± 10.5, 236 ± 6.8, 453 ± 9, and 481 ± 1.8 nm. Concentrations covered a range of optical transmissions from 0.7% to 99.3% at a temperature of 20.6 ±

0.2 °C. The scattering angle was varied from 10° to 135°. The cross-correlation functions were found to be single exponential and predicted the correct radii at all concentrations where auto-correlation failed.

Pine *et al.* (1988) described the use of a new technique in quasielastic light scattering. The new technique was called diffusing-wave spectroscopy (DWS), and it was meant to extend the use of quasielastic light scattering to multiple scattering media. Their theory dealt with backscattering and transmission auto-correlation functions for a diffusive media. They used one variable parameter, l* (effective transport mean free path) in their transmission model, and two variable parameters, l* and κ in their backscattering model. These parameters were determined by fitting the transmission and backscattering models to the experimental data. They conducted experiments on suspensions of 0.497 μm polystyrene latex particles using a laser with a wavelength of 488 nm. Their transmission model fit the experimental data very well for an l* value of 1.43 μm. Their backscattering model fit the experimental data well when values of 1.43 μm and 2.0 were used for l* and κ respectively. Experiments were also conducted on mixtures of two different interacting and non-interacting particle sizes (0.312 μm and 0.497 μm diameter) in optically thick media. They observed that the correlation function for the non-interacting particles decayed slower in both backscattering and transmission.

As stated earlier, multiple scattering has to be suppressed or eliminated in order to use the well-developed single scattering theory to predict the radius accurately. Alternatively, a well developed multiple scattering theory must be developed to interpret the multiple scattering data correctly. The papers discussed so far covered the work done in suppressing multiple scattering by different techniques. A review of the work done in developing a multiple scattering theory for accurate particle characterization follows.

Dougherty *et al.* (1991) and Ackerson *et al.* (1992) developed a correlation transfer (CT) equation for multiple scattering of light. Since, the CT equation is formally similar to the radiative transfer transport equation, radiative transport solution techniques were applied to obtain solutions for the field correlation functions in isotropic one-dimensional media, assuming small correlation delay times and optically thick media. Comparisons were made between the correlation function predicted by the CT solution and the experimental data, and were found to agree well. Another paper describing this work by Dougherty *et al.* (1994) is also listed in the References section of this thesis.

Dorri-Nowkoorani *et al.* (1993) experimentally verified the work of Dougherty *et al.* (1991) and Ackerson *et al.* (1992). They used two laser beams, viz., an argon-ion laser (514.5 nm wavelength) and a DPY diode laser (532 nm wavelength) to illuminate monodisperse suspensions of polystyrene latex particles in water. Particles tested were of 0.091 and 0.3 μm diameter. Correlation function measurements for optical thicknesses 5, 10, and 25 were compared to those predicted by the CT theory. These comparisons showed good agreement. They also concluded from preliminary results that, at an optical thickness of ~ 0.05, transition from single scattering to multiple scattering begins.

2.3 Multiple Scattering Suppression by a Single-Beam, Two-Detector Cross-Correlation Technique

The earlier techniques of multiple scattering suppression made use of the two-beam, two-detector cross-correlation approach. This approach, though effective in suppressing the effects of multiple scattering, has a serious drawback, that of alignment. The two laser beams and the two detectors must be aligned very carefully in order to ensure that the two detectors "see" the same scattering vectors. This condition leads to levels of alignment that are difficult to handle. This situation led to the pursuit of techniques that are equally effective in suppressing multiple scattering but do not overburden the procedure with complicated alignment. A major breakthrough came in 1997 when a single-beam, two-detector approach was applied by some researchers with encouraging results.

Meyer *et al.* (1997b) argued that single scattering arises from a tightly focused incident beam, whereas multiple scattering tends to arise from a larger fuzzy sort of halo around the incident beam. Thus, the time-dependent speckle field corresponding to single scattering can be expected to have a high spatial coherence over a larger region than does the speckle field of multiply scattered light. So multiple scattering is correlated over a smaller spatial distance transverse to the beam. By collecting light from two locations slightly separated in the direction transverse to the beam direction, it is possible to strongly favor single scattering over multiple scattering by cross-correlating the two detector outputs. To prove this claim, they performed experiments using an argon-ion laser operating at a wavelength of 514.5 nm. Two single mode optical fibers were placed at a distance of 170 mm from the system axis, and were capable of being separated by distances of 0.25, 0.50, or 0.75 mm at the cores. Experiments used monodisperse suspensions of polystyrene latex particles (diameters 0.107 and 0.204 μm) in water, with concentrations ranging from 0.0017 to 5% by weight. Their experimental results showed that decay time had little dependence on the separation distance between the fibers. The auto-correlation function exhibited non-exponentiality with increasing concentration and consistently predicted lower particle radii. The cross-correlation function, however, clearly exhibited exponentiality and predicted radii correctly. Another article by those authors [Meyer *et al.* (1997a)] describing the same experiment is also listed in the References section of this thesis.

Lock (1997b) proved theoretically the effectiveness of the one-beam, two-detector setup used by Meyer et al. (1997b) to suppress the effects of multiple scattering. He began by describing the scattering geometry and the notation followed. He then derived the singly scattered and the doubly scattered electric fields at the detectors. Next, he derived the single scattering and double scattering contributions to the electric field cross-correlation function. Treatment of the equation was limited to volume fractions less than 0.1. Finally, the intensity cross-correlation function was calculated, the degree of double scattering suppression was determined, and the time dependencies of auto-correlation and cross-correlation functions were established. He demonstrated the suppression of double scattering and by inference all multiple scattering. He concluded with the result that multiple scattering occurs over a relatively large region in the direction transverse to that of beam propagation, than does single scattering. If the two detectors focus on the same single scattering coherence area but on different multiple scattering coherence areas, single scattering should be strongly cross-correlated, but multiple scattering should not be correlated. Another paper by the same author [Lock (1997a)] dealing with the same subject has been cited in the References section of this thesis. The first paper had a preliminary version of the calculations shown in the second paper and ignored both the polarization and the angular dependence of scattered light.

The main basis of the research pursued in this thesis is the work done by Nobbmann *et al.* (1997). The work described in that paper was an extension to the work done by Meyer *et al.* (1997b). The greatest feature of the Nobbmann *et al.* work was the development of a setup that showed the effect of multiple scattering suppression with increasing separation (or tilt angle) between the fibers. The setup used by Nobbmann *et al.* was similar to that used by Meyer *et al.* (1997b), with one major difference. Nobbmann *et al.* used a beam splitter to divide the scattered beam into two approximately equal beams. The two beams were directed to the two single mode fibers that used GRIN lenses for better detection. This setup separated the two detectors by 90° physically, but they were effectively separated by only a few milliradians.

Experiments were performed on suspensions of polystyrene latex particles (0.107 μm diameter) at volume fractions of 0.15 and 0.25%, for a scattering angle of 90°. A study of the multiple scattering suppression with increasing tilt angles (separation) between the fibers was conducted. From the experimental results, they were able to conclude that when the tilt angle was equal to 0 mrad, the cross-correlation function decayed faster than that of single scattering. The predicted radius was found to be consistently lower than the actual radius. At a tilt angle of approximately 1 mrad, the effects of multiple scattering had been suppressed, and the radii were found to be accurate. They also derived an expression to predict the signal-to-noise ratio by assuming Gaussian fields of view for the fibers. The agreement of the values predicted by the theory with the experimental data was found to be good.

2.4 Flow Effect Suppression

The second objective of this research was the extension of multiple scattering suppression to flowing media. The presence of flow complicates the data analysis and interpretation by adding a Doppler beating term to the field correlation function. Suppression of flow effects is necessary in order to enable easy application of light scattering analyses. Unfortunately, not much work has been done on the applicability of DLS to flowing systems, and only a few articles on the subject are available. A paper by Ackerson and Clark (1981) studying the applicability of DLS to determine the intensity correlation function for dense system of particles subjected to a low rate of shear is listed in the References section of this thesis. Another article by Hoppenbrouwers and van de Water (1998) on the same subject is also listed. A detailed review of the work done in the study of flow effects suppression is given by Cambern (1999).

CHAPTER III

THEORETICAL BACKGROUND

3.1 Introduction

The pursuit of the two objectives in this research is based upon two major ideas, viz., multiple scattering suppression and flow suppression. In the first section of this chapter, an outline of Dynamic Light Scattering theory will be given, along with some major equations. The second section will deal with the concept of multiple scattering suppression and the theoretical idea behind it. The third section will deal with the problems caused by the effect of flow on particle sizing and the theoretical explanation of suppression of flow effects. Finally, the theoretical prediction of the signal-to-noise ratio by Nobbmann *et al.* (1997) will be outlined in the fourth section of this chapter.

3.2 Dynamic Light Scattering

Light is scattered by a particle in a medium. Since the particles in the fluid suspensions of interest in this thesis are in constant random (or Brownian) motion, their positions are continually changing. Thus, the intensity of coherent scattered light received by a detector viewing a given volume is also continually changing. Figure 1 shows schematically a typical plot of the intensity of scattered light with time [Weiner

(1984)]. It consists of a time-averaged part and a temporally fluctuating part. The dynamic information of interest is contained in the fluctuations, and the fluctuations are conveniently described by a time-dependent correlation function. The most efficient way to analyze the intensity fluctuations is to average the product of the intensity of the signal from a detector and a time delayed version of the intensity as a function of that delay time, τ [Berne and Pecora (1976)]. The normalized intensity correlation function is defined as follows.

$$g^2(\tau) = \frac{\langle I_1(t) I_2(t+\tau) \rangle}{\langle I_1(t) \rangle \langle I_2(t) \rangle} \tag{3-1}$$

$$= \frac{\lim_{T_e \to \infty} \frac{1}{T_e} \int_0^{T_e} I_1(t) I_2(t+\tau) dt}{\left(\lim_{T_e \to \infty} \frac{1}{T_e} \int_0^{T_e} I_1(t) dt \right) \left(\lim_{T_e \to \infty} \frac{1}{T_e} \int_0^{T_e} I_2(t) dt \right)} \tag{3-2}$$

where the intensities I_1 and I_2 have, in general, different values at times t and t+τ. The angular brackets indicate the time average of the quantity over the total experiment duration, T_e as in Eq. (3-2), or the ensemble average over space. If only one detector is used to detect only one signal, then I_2 is replaced by I_1 in the two equations above, and the function is called an intensity auto-correlation function. If two detectors are used for the experiment to detect two different signals, then the function is called an intensity cross-correlation function. The intensity correlation function is measured experimentally by commercially available correlator hardware and software, that multiply the shifted intensities of the signal(s) together and average the result. For delay times that are large compared to the characteristic time for the fluctuation of I, I(t) and I(t+τ) are expected to become totally uncorrelated, and the intensity correlation function decays from $\langle I^2 \rangle$ to

$\langle I\rangle^2$ [Berne and Pecora (1976)]. The intensity correlation function is shown in Fig. 2. The scattered electric field, which is a function of particle position, is also continuously changing. The intensity is given in terms of the electric field as

$$I(t) \propto |E(t)|^2 \tag{3-3}$$

The electric field correlation function is defined as [Berne and Pecora (1976)]

$$g^1(\tau) = \frac{\langle E(t)E^*(t+\tau)\rangle}{\langle E(t)\rangle^2} \tag{3-4}$$

where E* is the complex conjugate of the electric field E.

If the scattered beam has Gaussian statistics, the intensity correlation function is related to the field correlation function by the Siegert relation [Wiese and Horn (1991)]

$$g^2(\tau) = 1 + \gamma^2 |g^1(\tau)|^2 \tag{3-5}$$

The correlation function amplitude γ^2 is an instrumental constant known as signal-to-noise ratio ($0 \le \gamma^2 \le 1$). It should be equal to one when the detector intercepts less than one coherence area of the far field speckle pattern of the scattered light.

If light is scattered by a large number of independently diffusing particles of equal and spherical size [Weise and Horn (1991)], then

$$g^1(\tau) = \exp(-\Gamma\,\tau) \tag{3-6}$$

where Γ is the decay rate of the correlation function. The decay rate is related to the free particle diffusion coefficient (when the scattered light is not mixed with unscattered light) as

$$\Gamma = 2D_0q^2 \tag{3-7}$$

Figure 3 shows the wave vector geometry. $\vec{\mathbf{k}}_i$ and $\vec{\mathbf{k}}_s$ are the incident and the scattered wave vectors, respectively, and their magnitudes are given by

$$k_i = k_s = \frac{2\pi n}{\lambda} \tag{3-8}$$

$\vec{q}$ is the scattering wave vector, and is the resultant of the incident and the scattered wave vectors. The magnitude of $\vec{q}$ is given by

$$q = \frac{4\pi n}{\lambda}\sin\left(\frac{\theta}{2}\right) \tag{3-9}$$

where n is the refractive index of the medium, θ is the scattering angle (see Fig. 3), and λ is the wavelength of the laser light in a vacuum.

The diffusion constant D_o is given by the Stokes-Einstein relation for spherical particles [Weiner (1984)]

$$D_o = \frac{k_B T}{6\pi\eta r_p} \tag{3-10}$$

where k_B is the Boltzmann constant, T is the absolute temperature, η is the viscosity of the solvent, and r_p is the radius of the particle.

The theory mentioned above holds well for purely single scattering and predicts the radius very accurately. Multiple scattering however leads to non-exponential decay of the correlation function. So, in order to predict particle sizes from scattering events that are not pure single scattering from monodisperse diffusing particles, the electric field correlation function is fitted with a two-cumulant expansion [Nobbmann *et al.* (1997)]

$$g^1(\tau) = \exp(-2u\tau + 2j\tau^2) \tag{3-11}$$

where the first cumulant (u) is $D_o q^2$. The normalized second cumulant (j/u^2) is an indicator of the quality of the fit, which shows the amount of non-exponentiality of the correlation function, and hence the amount of polydispersity, statistical error, or multiple scattering present. For absolutely monodisperse spherical particles in single scattering, the normalized second cumulant should vanish.

This concludes the brief outline of the theoretical background and the procedure by which particle sizes can be estimated based on the fluctuating intensities measured. In the following section, the technique used in this research to suppress multiple scattering effects will be discussed.

3.3 Multiple Scattering Suppression

In order to gain a theoretical understanding of the technique of multiple scattering suppression used in this research, a fundamental knowledge of the characteristics of single and multiple scattering is important.

Scattering occurs when a light beam interacts with a particle. Depending upon the circumstances, two types of scattering can occur. When the incident light beam is scattered by only one particle in the medium before it exits the medium, the phenomenon is called single scattering. When the incident light beam is scattered by more than one particle before it exits the medium, the phenomenon is called multiple scattering. Usually, both types of scattering occur together, but multiple scattering is more dominantly observed in most practical applications.

When scattering takes place, a speckle pattern is often observed. This complex pattern results from interference of electromagnetic radiation that originates from a coherent source but follows different paths in reflecting or scattering to the detector

[Nobbmann *et al.* (1997)]. At some points on the detector, the total field reflected from the surface will add constructively and be bright, whereas at other points, the total field will add destructively and be dark. If the laser beam is focused into a small region on the scattering surface, the speckle size increases in dimension at the detector, in a direction normal to the direction of beam propagation. This is the diffraction effect, which is similar to single-slit diffraction, wherein the diffraction pattern width increases as the slit width decreases.

For a fairly narrow (e.g. 0.1 mm or less) illuminating laser beam, singly scattered light results from the volume of the incident beam, whereas the overwhelming majority of multiply scattered light stems from the halo surrounding the incident beam, and so is diffused throughout the sample medium. Since the coherence area of a light source is inversely proportional to the area of the source, at the detector, the singly scattered light will have a larger coherence area when compared to that of multiply scattered light. Consequentially, the singly scattered light will have a broader speckle as compared to that of the multiply scattered light. So, multiply scattered light will be correlated over a smaller distance transverse to the direction of beam propagation, when compared to that of the singly scattered light.

The technique proposed by Meyer *et al.* (1997), and later experimentally verified by Nobbmann *et al.* (1997), exploits the fact mentioned above. Two detectors are placed with sufficiently large spatial (or angular) separation, in such a way that one of the detectors is viewing within the multiple scattering speckle, and the other is viewing within the single scattering speckle but outside the multiple scattering speckle. Since multiply scattered light has a smaller coherence area when compared to that of singly scattered light, when the two detectors are separated, the singly scattered signals will be strongly cross-correlated, whereas the multiply scattered signals will not. This technique was found to be effective in suppressing the effects of multiple scattering and is followed in this research. It was however important to know the extent of angular separation of the detectors required, before multiple scattering ceased to be correlated. Therefore, experiments were performed to sweep through increasing angular separation distance, and the effects of that distance on multiple scattering effects was studied for various concentrations in this research. Figure 4 shows a typical plot of the Y-intercept, also known as $g^2(0)$, as a function of the tilt angle of separation between the detectors. The plot shows two distinct regions for the Y-intercept curve, viz., the peak and shoulders. The peak is the area where multiple scattering is strongly correlated, whereas at the shoulders, because of the separation between the fibers, multiple scattering ceases to be correlated. The radius is predicted accurately at the shoulders. The effect of concentration on the shape and behavior of the peak and shoulders will be a subject of discussion in Chapter VI.

3.4 Flow Suppression

The theory described in the previous section was for a non-flowing case. The presence of flow affects Dynamic Light Scattering to a significant extent, because particles are not only moving relative to each other in a Brownian motion but are also moving in the direction of the flow.

Ackerson and Clark (1981) studied Dynamic Light Scattering in fluids subjected to low rates of shear. Their theoretical analysis is based on assumptions that restrict the flow velocities to very low Reynolds numbers. Also, assumptions of the system being dense are made in order for Gaussian statistics to prevail. Based on these assumptions, the intensity correlation function for a flowing fluid case has been derived. The signal-to-noise ratio for such a system has also been predicted by the theory.

For a flow case, the field correlation function can be written as follows:

$$g^1(\tau) = \exp\left(-2D_0 q^2 \tau + i\vec{\mathbf{q}} \cdot \vec{\mathbf{v}}(\mathbf{r})\tau\right) \tag{3-12}$$

where $\vec{\mathbf{v}}$ is the flow velocity vector. The second term in the equation above is the flow contribution to the field correlation function, and is known as 'Doppler Beating'. It can be seen that the effect of flow is to incorporate substantial amounts of non-exponentiality in the field correlation function, and by inference, cause incorrect prediction of particle radii.

It can be readily seen from Eq. (3-12) that the Doppler beating term can be eliminated if the dot product of the two vectors $\vec{\mathbf{v}}$ and $\vec{\mathbf{q}}$ is zero. This condition is met when the scattering wave vector is perpendicular to the flow velocity vector. To experimentally achieve this, the angular bisector between the incident beam and the scattered beam should be perpendicular to the direction of the flow. In this case, the dot product vanishes, the exponentiality of the field correlation function is restored, and the effect of flow is eliminated. Figure 5 shows the scattering geometry required for the suppression of flow effects. It is imperative to point out here that, because of practical limitations, it is very difficult to perfectly achieve this perpendicularity condition. So, there is always a minor effect of the Doppler beating term remaining in the field correlation function, and thus flow effects are actually suppressed rather than completely eliminated. The Doppler time constant is a measure of how misalignment affects the calculation of particle diameter, and is defined as [Cambern (1999)]

$$\tau_{\text{Doppler}} = \frac{1}{q\cos(90-\delta)\,v_{\text{centerline}}} \tag{3-13}$$

where δ is the cell rotation angle (described in a later section) by which the geometry required to suppress flow effects is violated, and $v_{\text{centerline}}$ is the velocity along the centerline of the test cell.

Even though flow effects are not completely eliminated, they are suppressed substantially enough to enable accurate particle sizing. This technique was used in this research in pursuit of the second objective, and it was found to be very successful.

3.5 Theoretical Prediction of Signal-to-Noise Ratio

Nobbmann *et al.* (1997) derived an equation to predict the S/N ratio for a single-beam and two-detector cross-correlation setup. The system used by them is shown in Fig. 6. They made use of a laser beam to illuminate a cylindrical sample cell that was held inside an index-matching beaker filled with water. Two spatially separated single mode fibers viewed the same detection volume. The two signals were cross-correlated and the particle radii were accurately predicted. Since the experimental setup used in this research was the same as that used by Nobbmann *et al.*, it was a point of interest to verify the accuracy of the prediction of the S/N ratio. The intensity correlation function for a Gaussian random process is first defined as [Nobbmann *et al.* (1997)]

$$\langle I(\vec{r}_1,t_1)I(\vec{r}_2,t_2)\rangle = \langle I(\vec{r}_1,t_1)\rangle\langle I(\vec{r}_2,t_2)\rangle\left[1+\left|\gamma(\vec{r}_1,\vec{r}_2,t_1-t_2)\right|^2\right] \tag{3-14}$$

where $I(\vec{r},t)$ is the intensity at point $\vec{r}$ and time t, and $\gamma(\vec{r}_1,\vec{r}_2,t_1-t_2)$ is the second order complex degree of coherence. If the intensities originating at different regions in the scattering volume are spatially uncorrelated, then the van Cittert-Zernike theorem [Nobbmann *et al.* (1997)] in the far-field limit gives:

$$\gamma(\vec{r}_1,\vec{r}_2,0) = \frac{\int I(r')\exp\left[-i\vec{k}_s\cdot(\vec{s}_1-\vec{s}_2)r'\right]d^3r'}{\int I(r')d^3r'} \tag{3-15}$$

where $\vec{k}_s$ is the wave vector of the elastically scattered radiation. The two unit vectors $\vec{s}_1$ and $\vec{s}_2$ point from an origin in the scattering volume to the two detector positions. The intensity $I(r')$ is a function of the overlap of the areas of the incident beam, the multiple scattering within the sample volume and the field of view of the detectors. By approximating the fields of view of the two detectors as Gaussian tubes, by representing the finite size of the sample cell by a Gaussian cutoff function, and by combining these functions, Nobbmann *et al.* arrived at an equation for the second order complex degree of coherence term, γ.

In order to evaluate the integrals, some approximations were made. Assumptions were made as follows: a small focused laser beam (related to β_t), an intermediate detection width (related to α_t), and a large sample volume (related to δ_t), i.e., $\beta_t >> \alpha_t >> \delta_t$. β_t is the square of the inverse of the beam waist radius in the sample. The detector field of view was approximated as a cylinder. The diameter of this cylinder was arrived at by multiplying the fiber divergence angle by the fiber distance from the sample. α_t is the square of the inverse of the detection cylinder radius. δ_t is the square of the radius of the multiple scattering volume in the sample. With these simplifications, the expression for γ was reduced to [Nobbmann *et al.* (1997)]

$$\gamma(\phi)=\frac{\mathrm{A}\dfrac{\exp\left(\dfrac{-\mathrm{q}^2\phi^2}{8\alpha_t}\right)}{\left(\alpha_t^{\,2}\left[\dfrac{\alpha_t\phi^2}{4}+\delta_t\right]\right)^{1/2}}+2\mathrm{B}\dfrac{\exp\left(\dfrac{-\mathrm{q}^2\phi^2}{4\beta_t}\right)}{\beta_t\sin(\theta)\sqrt{\alpha_t}}}{\dfrac{\mathrm{A}}{\alpha_t\sqrt{\delta_t}}+\dfrac{2\mathrm{B}}{\beta_t\sin(\theta)\sqrt{\alpha_t}}} \qquad (3\text{-}16)$$

where ϕ is the tilt angle between the two optical fibers (see Fig. 6), and θ is the scattering angle. The quantity A:B is the ratio of the multiple to the single scattering. Note that Eq. (3-16) can be written in terms of the parameter A:B, so that A and B can not be distinguished, i.e., only the ratio of A to B is important. The square of the quantity γ is the signal-to-noise ratio. A detailed account of the work done in verifying the accuracy of the theoretical prediction of the S/N ratio will be presented in Chapter VI.

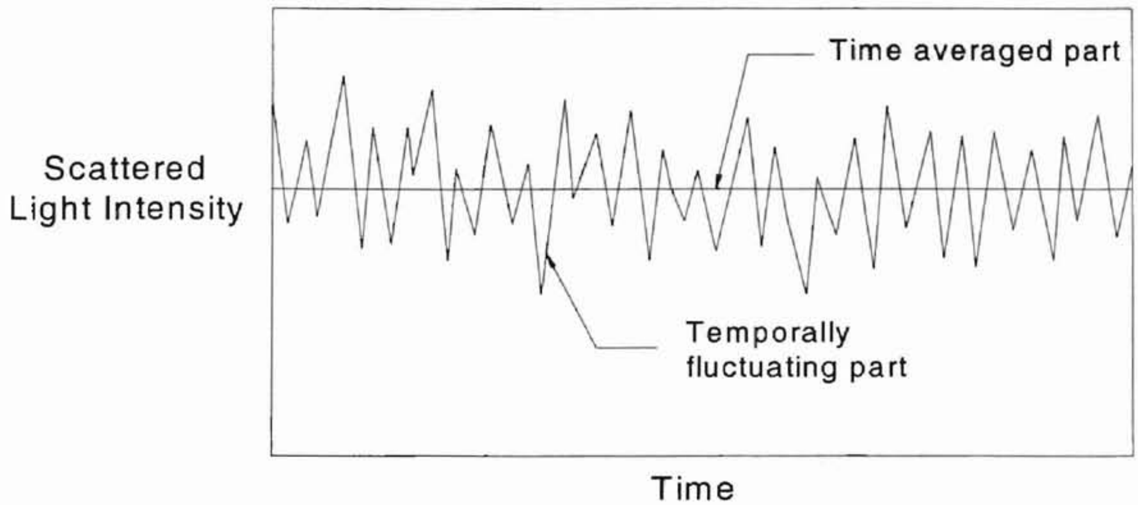

Figure 1: Typical fluctuation of the intensity of scattered light with time.

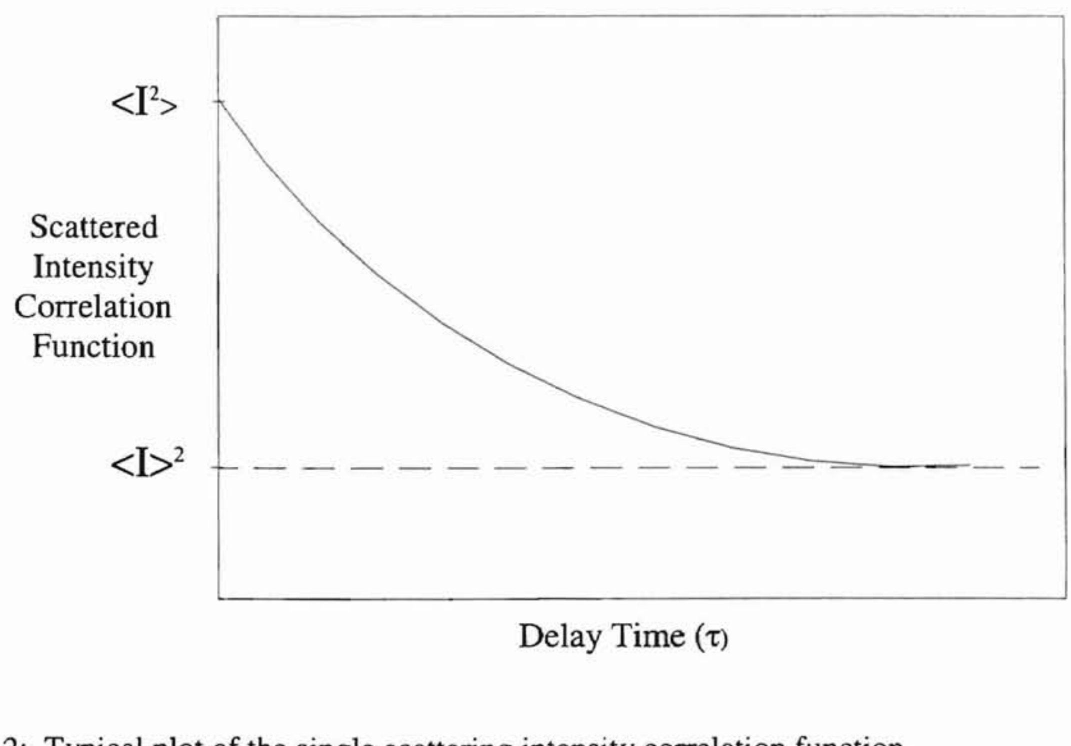

Figure 2: Typical plot of the single scattering intensity correlation function.

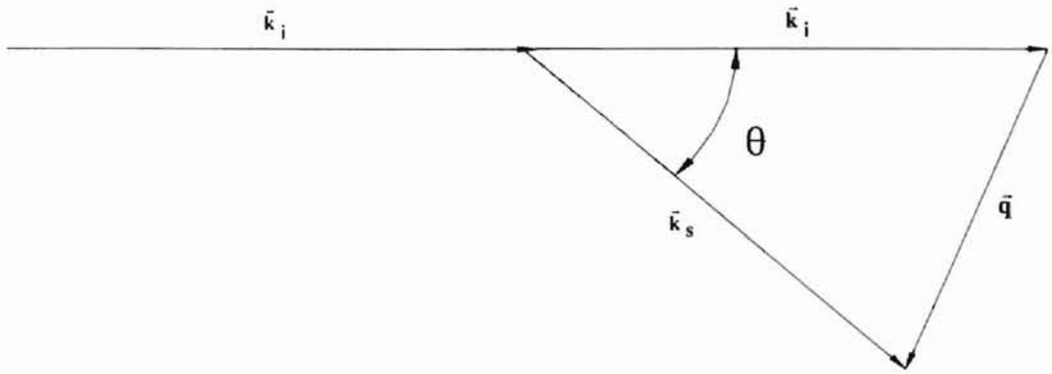

Figure 3: The wave vector geometry used to determine the scattering angle. $\vec{k}_i$ is the incident wave vector, $\vec{k}_s$ is the scattered wave vector, and $\vec{q}$ is the resultant scattering wave vector between $\vec{k}_i$ and $\vec{k}_s$.

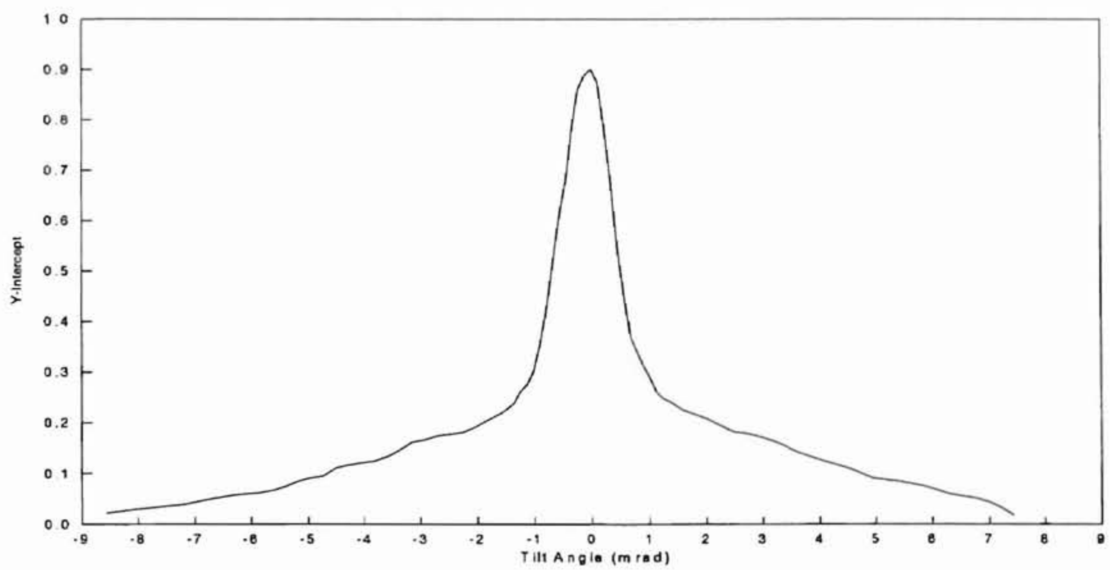

Figure 4: Plot of the Y-intercept as a function of tilt angle to demonstrate the peak and the shoulders. The results correspond to the Y-intercept mapping experiment on 0.107 μm PSL particles at a volume fraction of 0.32 percent. The scattering angle is 90°, and a square cell is used.

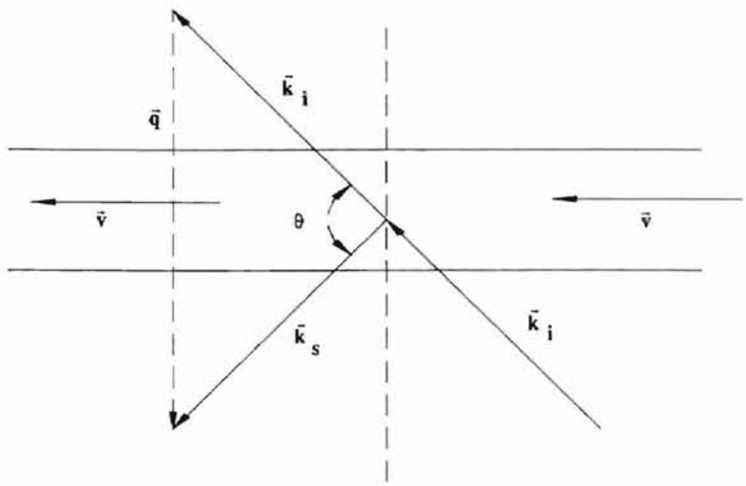

Figure 5: The geometry required to suppress flow effects. $\vec{k}_i$ is the incident wave vector, $\vec{k}_s$ is the scattered wave vector, and $\vec{q}$ is the resultant scattering wave vector. $\vec{v}$ is the flow velocity vector. θ is the scattering angle for this geometry.

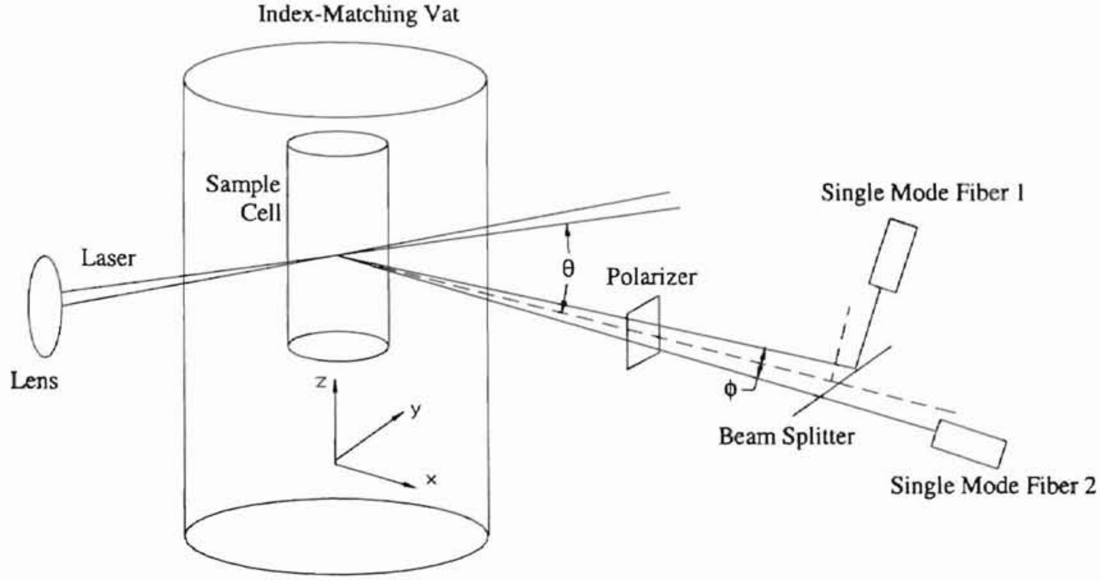

Figure 6: The experimental setup used by Nobbmann *et al.* (1997) for the one-beam, two-detector, cross-correlation experiment for multiple scattering suppression.

CHAPTER IV

NON-FLOWING CASE: EXPERIMENTAL SETUP AND PROCEDURE

4.1 Introduction

This chapter focuses on the first objective of this research, viz., multiple scattering suppression in non-flowing media. The experimental setup used was very similar to that used by Nobbmann *et al.* (1997), who demonstrated the suppression of multiple scattering effects in non-flowing media. Experiments were performed with different sample concentrations in order to expand the work done by Nobbmann *et al.* The second section of this chapter will give a detailed description of the equipment used for the non-flowing experiments. The third section will describe the delicate alignment procedure followed for the experiments. The fourth section will cover the experimental procedures followed.

4.2 Experimental Setup

The main components involved in the experimental setup can be classified into four groups, viz., the goniometer, the light source, the sample, and the detection devices. Figure 7 shows a schematic of the experimental setup used for the non-flowing experiments. Details of the components will also be provided.

Goniometer

The goniometer was the component of the setup that held the three other groups of components. The goniometer had a stationary laser arm, a mobile detector arm and a sample stand (see Fig. 7). The axis of rotation (henceforth referred to as 'the axis') of the detector arm was the geometric axis of the sample stand. The goniometer was rigidly attached to the experiment table. The detector arm was capable of being moved through scattering angles ranging from 0^{o} to 130^{o}.

Laser

The second group is composed of the light source and associated components. A helium- neon laser (see Appendix I) was used as a source of coherent light. The laser operated at a wavelength of 632.8 nm in a vacuum, and its total power was 20 mW. The vertically polarized red light beam had an original beam diameter of 0.68 mm. An aluminum holder was used to position the laser. The holder was mounted on top of two 9 mm thick aluminum plates positioned one on top of the other, which could provide slight vertical adjustments (or tilts), by adjustment of the four screws at the four corners of the plates (see Fig. 7). The holder with plates was attached to the laser arm that was stationary. The eye of the laser was 72 cm from the axis, and was at a height of 24.5 cm above the experiment table.

Attenuator

Also mounted on the laser arm was a variable attenuator, which was used to adjust the power output from the laser to that required by an experiment. The laser output could be attenuated within a range of 0.08 mW to 9.54 mW by the attenuator. A Newport wand type power meter (see Appendix I) was used to determine the range of attenuation by direct measurements. The attenuator was placed 67 cm from the axis and

5 cm from the laser eye.

Lens

A lens (see Fig. 7) was used to focus the beam inside the sample. A 12.7 mm diameter lens with a focal length of 33 mm was used for the experiments. The lens was positioned by a lens holder composed of a dovetail shaped base that could be slid along the laser arm by unclamping the base, and was capable of providing small translations in the x, y and z directions. These translations helped to move the lens around until the beam was focused to its narrowest at the center of the sample. The lens was placed 4 cm from the axis.

Sample Stand

The third group of components was composed of the sample stand, water bath and the sample cell (see Fig. 7). The cylindrical sample stand was made of aluminum, and was mounted on the goniometer at the axis by a cylindrical rod screwed into the bottom of the stand. The height at which the stand was held had a slight degree of freedom, which could be controlled by a setscrew on the shaft. The sample stand was used to hold the water bath.

Water Bath

A water bath was used in the experiments for refractive index matching. Also, the presence of a larger diameter water bath surrounding the sample ensured that slight adjustments had smaller refraction effects on the way the laser beam moved inside the sample. The container holding the water bath had an outer diameter of 66.5 cm, a height of 9 cm and a wall thickness of 2.1 mm. The water bath container was made of glass in the shape of a beaker. The container had a lid and a base ring made of Teflon. Both the lid and the ring, which could be slid to the bottom of the container, were made to fit snugly against the inner walls of the container. The lid and the base ring had thicknesses of 32 mm and 16 mm, respectively. They had circular holes cut through their centers, to hold the sample cell vertically inside the container.

Sample Cell

The sample cell was a cylindrical test tube made of borosilicate glass (see Appendix I). The dimensions of the sample cell were 10 mm outside diameter and 75 mm in length. The sample cell was held at the center of the water bath container by the lid and the base ring.

Beam Splitter

The fourth group of components was composed of the detection equipment. The detection equipment consisted of a non-polarizing, wavelength specific, cube beam-splitter, and two optical fibers. The beam-splitter was used because both detectors looked at the sample volume, being separated only by a few milliradians. This was not physically possible without using a beam-splitter. The beam-splitter had a semi-reflecting surface that reflected a part of the beam by 90^o, while transmitting an equal part. This helped by separating the two detectors by an angular spacing of 90^o, though the detectors were effectively separated angularly only by a few milliradians. This technique was originally conceived and used by Nobbmann *et al.* (1997).

Optical Fibers

The two optical fibers were single-mode, wavelength specific, non-polarization preserving (see Appendix I). The optical fibers helped to transmit the signal from the detectors to the two photomultiplier tubes (PMTs).

Detector Unit

The detector unit was made of aluminum, and had a dovetail shaped base that could be slid along the detector arm of the goniometer when unclamped. Figure 8 shows the side view of the detector housing and its components. The detector housing had a base on which a stand made of Teflon was mounted. The stand was used to hold the beam-splitter without any degree of freedom. The detector housing had provisions to mount the two optical fibers, one at the back to "see" the directly transmitted light, and the other at the top to "see" the beam reflected by the beam-splitter.

The motion of the fiber at the top could be controlled by the use of four micrometers. Two of the micrometers enabled slight translation along the x and y-directions, and the other two enabled slight tilts of the fiber. Figures 9 and 10 show block diagrams of the mount for the top fiber as viewed from the front and the top, respectively. Details of the detector housing and the fiber mounts are given by Cambern (1999). Four setscrews with springs controlled the motion of the back fiber. This provided only limited control over the motion of the back fiber and the absence of micrometers made the recording of specific fiber settings impossible. But since the back fiber was aligned only at the start of the experiment, and was not moved during an experiment, this limitation did not seriously hamper the progress of the experiments. Figures 11 and 12 show block diagrams of the mount for the back fiber in the rear and the top views, respectively. The detector unit was 44.5 cm, from the axis to the closest vertical surface of the beam-splitter.

Calibration of the Tilt Micrometer for the Top Fiber

The rear tilt micrometer controlling the top fiber had to be calibrated in order to determine the angular measure corresponding to each division of tilt. This was accomplished by moving the detector arm to a scattering angle of 0° in order to "see" the direct beam. The rear tilt micrometer was moved in order to "see" the shift in the position of the reflected light from the top fiber through the beam-splitter onto the exit plate of the laser. The micrometer was moved several divisions and repeated measurements were made. Then the average shift in the position of the reflected spot was found to be 6 mm for 25 divisions of tilt of the micrometer. The distance from the eye of the laser to the lens of the fiber was measured and found to be 106.9 cm. The micrometer tilt angle was then calculated using the relation:

$$\tan(2\phi) = \frac{\text{Average Shift per Division}}{\text{Distance}} \tag{4-1}$$

The tilt angle corresponding to each division on the rear tilt micrometer was found to be 0.1125 mrad.

Polarizer

A polarizer was used as part of the detection equipment. The polarizer was placed in the vertically polarizing mode at a distance of 20 cm from the axis (on the detector arm). (The position of the polarizer was not very critical.) The polarizer was used because single scattering is polarization preserving, whereas multiple scattering typically does not preserve polarization. The presence of the polarizer transmitted nearly all of the vertically polarized singly scattered light and some of the multiply scattered light, blocking all of the non-vertically polarized multiply scattered light. This helped to reduce the amount of multiply scattered light reaching the detectors.

Photomultiplier Tubes

The optical fibers were connected to two photomultiplier tubes (see Appendix I).

The PMTs received scattered laser light through the fibers and converted them into digital pulses representing the count rate which is the number count of the photons received per second (and is a measure of the intensity of scattered light). The presence of two PMTs enabled suppression of dead time effects associated with the use of one PMT. These PMTs were powered by two power supply units (see Appendix I). These power supply units maintained a constant supply of 12 volts at 5 amps.

Digital Correlator Hardware

The digital pulses registered by the PMTs were transmitted to the ALV digital correlator board in the computer. The correlator board processed the digital pulses and provided the information for the software to perform data analysis.

Correlator Software

Correlator software was used for the experiments to read the data sent in by the correlator board, process the information and calculate the particle size. The software used was the ALV-5000/E Multiple Tau Digital Correlator (see Appendix I). The version of the software used was designed to run under the MS-DOS operating system.

The count rates received from the PMTs were processed by the ALV program to yield the intensity correlation function, from which the field correlation function was determined. The experimental data for the field correlation function was fit with a theoretical two-cumulant expansion, and the radius of the particles was determined based on the procedure and the Eqs. (3-10) and (3-11) presented in Chapter III.

The software contained four sets of menus with several commands listed under each menu. One set of menus was active under normal operation, and was called the 'main menu'. The second, third and the fourth sets of menus were called by pressing the

'Shift', the 'Control', and the 'Alt' keys on the keyboard respectively.

Table 1 lists the various menus of the software, the parameters associated with some of the menus, and the values set for the parameters. The parameters which are not of interest in this research were not invoked, and are not listed in the table.

Table 1: Various Menus and Parameters of the ALV-5000/E Correlator Software Along with the Values Input for Those Parameters.

Function Key	Subdirectory	Parameter/Description	Value Set
Main Menu			
F1	Help		
F2	Start (Stop)	Start/Stop a Run	
F5	SampOpt	Wavelength [nm]	632.8 or 532.5
		Refractive Index	1.332
		Solvent Viscosity	Auto Calculated
		Probe Temperature [K]	Input
		AutoCorrect for Solvent	Water
F6	Angle	Scattering Angle	Input
F7	Multi	Enable Multiple Runs	Varied [Yes/No]
		Number of Runs	100
		Enable Autoscale of Runs	No
F9	GetDat	Get the Data File	Enter File Name
F10	SavDat	Save the Data File	Enter File Name
Shift Menu			
F8	EdWin	Edit the Size/Position of Window	
F9	GetWin	Get the Saved Window File	c:\sanjay.win
F10	SavWin	Save the Window Specification	
Control Menu			
F2	Scale	Autoscale	
F3	Setup	Duration (s)	Input
		Single/Dual/Fast	Single
		Auto/Cross	Varied
		Channel	Ch 0
		Automatic Autoscale	No
F4	FileOpt	Data File Format	Varied (ASCII/Binary)
Alt Menu			
F7	CumPar	First Evaluated Channel	10
		Last Evaluated Channel	128
F10	SavFit	Save the Fitted Data with the Analysis	Enter File Name

4.3 Alignment Procedure

The alignment of the various components was very critical to the success of the experiments. The alignment was very complex and sensitive, and had to be followed meticulously. Based on experience, a very structured alignment procedure was laid out and consistently maintained for all of the experiments. The alignment procedure will be discussed in detail in this section.

First, the laser was aligned with a level while turned off. The four screws on the aluminum plate were adjusted until the laser was horizontally level along the laser beam axis. From previous experiments, a dot was placed on the wall (facing the laser beam at a distance of 3.61 m from the laser eye), where the beam hit, when the laser was fully aligned with all components connected following the procedure described in this section. As a second check, the laser was turned on, and was checked to see if the beam hit the dot on the wall. If not, the laser was adjusted sideways or horizontally until the beam zeroed in on the dot.

Then the detector arm was moved to 0°, without any of the other components being mounted. The PMTs were turned off. The fibers were disconnected from the PMTs. The back fiber was aligned using the set screws until the light that came out of the fiber was the brightest, as deemed by visual judgement. The top fiber was then aligned using the motion control micrometers until the light passing through that fiber was the brightest, again as deemed by visual judgement.

Then, more accurate alignment was performed using a power meter (see Appendix I). The detection wand of the power meter was clamped to a stand attached to the experiment table. One end of the fiber to be aligned was held by a fiber optic holder, also attached to the experiment table, so that the intensity measurements were consistent. The two fibers were then aligned by adjusting the micrometers or setscrews to get the maximum intensity. From experience, when the power meter read a power of approximately 8 mW for each fiber, the fibers were considered to be aligned well.

Next, the water bath was added. There was a slight clearance between the walls of the water bath container and the sample stand, and the container was rotated until the beam of laser light passed through the water bath and hit the dot on the wall. Then the sample cell was added. The procedure for sample preparation follows this section.

The detector arm was moved to the scattering angle at which the experiment was to be performed. The lens holder was placed 37 mm from the goniometer axis on the laser arm, and was clamped firmly in place. The polarizer was also mounted on the detector arm. The optical fibers were then connected to the PMTs, and the PMTs were turned on. To this point in the procedure, the PMTs were isolated and turned off, because they were very sensitive to light, and even a mild exposure to roomlight could damage them.

The ALV software was launched, the initial parameters set, and the count-rate display mode was activated. The lens was adjusted sideways and vertically in order to maximize the count rates. The back fiber was designated as 'Channel 0' and the top fiber as 'Channel 1' (see Fig. 8), corresponding to the channels through which the ALV software received the data from the PMTs.

The attenuator was then mounted and the count rates (number of photons detected per second, which translate to the intensity of the scattered light) regulated to workable levels by use of the attenuator. The count rates were usually maintained between 50 and 150 kHz. Lower count rates resulted in significant loss of data, while higher count rates overloaded the PMTs. Typically Channel 1 had a count rate about 10 percent higher than Channel 0.

The last step of the procedure was to maximize the signal-to-noise ratio of the intensity cross-correlation function. This was done by alignment of the top fiber. The ALV software was used in the 'run' mode, and multiple runs lasting 8 seconds per run were enabled. The initial delay time was set at 200 nanoseconds. This duration was chosen from experience, since it was long enough to allow the data analysis to stabilize, and short enough to provide quick feedback on how a slight adjustment of the top fiber affected the S/N ratio. The top fiber was aligned until the S/N ratio was the highest, usually around 0.9. The corresponding value of the S/N ratio for the auto-correlation function was usually around 0.97 for both the fibers. The micrometer readings were then noted, and the multiple runs disabled in the program. The alignment was complete, and the experiment was ready to begin.

Sample Preparation

Like the alignment, the sample preparation was also done with extreme caution in order to prevent contamination of the sample and to avoid dirt or fingerprints on the sample cell. A new, disposable sample cell was cleaned with deionized water produced by an E-pure deionizer (see Appendix I). The cell was then dried in a vacuum oven and its dry weight was measured using an electronic weighing scale (see Appendix I). The cell was filled with water and the weight was measured again. The weight of the water was calculated from the dry weight, and the weight of the water plus cell. Polystyrene latex microspheres of diameter 0.107 μm (see Appendix I) were used for the non-flowing experiments.

Once the desired volume fraction of the particles was determined (by the experimenter), the mass of the core sample of polystyrene latex particles to be added was calculated from the equation

$$\text{Volume Fraction} = \frac{\text{Mass of particles}}{\text{Mass of water}} \frac{\text{Density of water}}{\text{Density of particles}} (\text{VF of the core sample}) \quad (4\text{-}2)$$

The density of water is 1.0 g/cc and the density of the polystyrene latex particles is 1.05 g/cc. The particles were then added to the water, and the total weight measured and noted. From this, the weight of the particles actually added was calculated, and from the above equation, the volume fraction of the sample was calculated. The sample cell was then sealed with Parafilm and labeled with the information on volume fraction, date of preparation, and the size of particles used. The sample cell was then shaken slowly to encourage mixing of the particles with water, but also preventing bubble formation. A sample typically can be used for two weeks. Beyond that time, aggregation of particles sets in, and this directly affects particle sizing experiments.

4.4 Experimental Procedure

The experimental procedure described in this section concerns the effects of varying the angular spacing between the detectors on the suppression of the multiple scattering effects. To accomplish this, the detector spacing was varied systematically, and the behavior of the cross-correlation function and the particle radius as a function of tilt angle between the fibers was mapped out.

At the start of the experiment, the top and the back fibers were aligned such that the S/N ratio was the highest. This corresponds to the case where the two detectors are viewing the sample volume at an angular separation of 0 mrad. In this case, the effects of multiple scattering will be most pronounced. The field correlation function will exhibit non-exponentiality and the radius of the particle predicted will be lower than the actual radius. It is at this point that the experiment is started. Typically, the curve of the intensity correlation function became smooth after about 90 seconds of data collection. So, the duration of each run was set for 120 seconds. When the run was complete, the software calculated the time-averaged count-rates received by Channel 0 and Channel 1. Other results of the analysis reported include: the intensity correlation (g^2) function, the value of the g^2 function at a delay time of 0 nanoseconds (also known as the Y-intercept), the radius of the particle, and the normalized second cumulant. These values were written down in a lab notebook, and the run saved in the ASCII/Binary format.

For the next run, the angular separation between the fibers was increased in one direction, by adjusting the rear tilt micrometer for the top fiber by two divisions. The multiple run mode was enabled with a duration of 8 seconds per run. At that tilt angle, the micrometer controlling the front-back motion of the top fiber with respect to the sample cell (see Fig. 10) was adjusted, until the count rate on Channel 1 was maximized. This being done, the micrometer readings were written down in the lab notebook, the multiple run mode was disabled, the duration set to 120 seconds, and the run was started.

The process was repeated until the Y-Intercept dropped to below 0.05, whence the data collected was not useful for analysis. Care was taken accordingly to increase the duration of the runs. A low S/N ratio required a longer duration of run, to collect the same amount of useful data. This was reckoned by the smoothness of the g^2 function. The duration of the runs ranged from 2 minutes for a high Y-intercept, to about 10 minutes for low Y-intercepts. The procedure described above constituted one 'shoulder' of the Y-intercept, or one direction of tilt. The same procedure was followed for the other direction of tilt, or the other shoulder. The results of the experiments will be presented in Chapter VI.

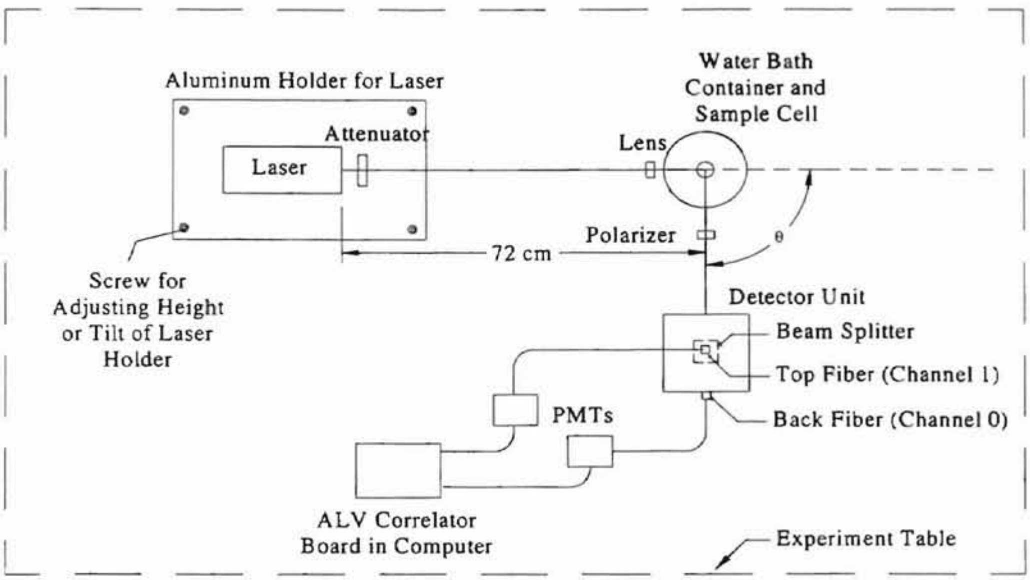

Figure 7: Schematic of the setup used for the non-flowing case experiments.

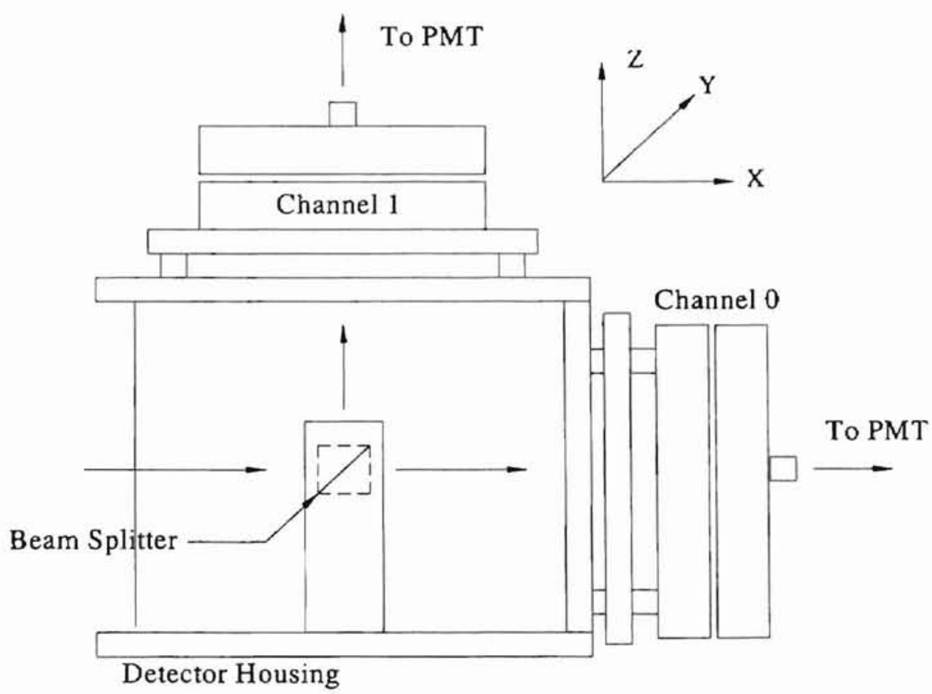

Figure 8: Side view of the detector housing showing where the fiber mounts attach, and the location of the beam-splitter [Cambern (1999)].

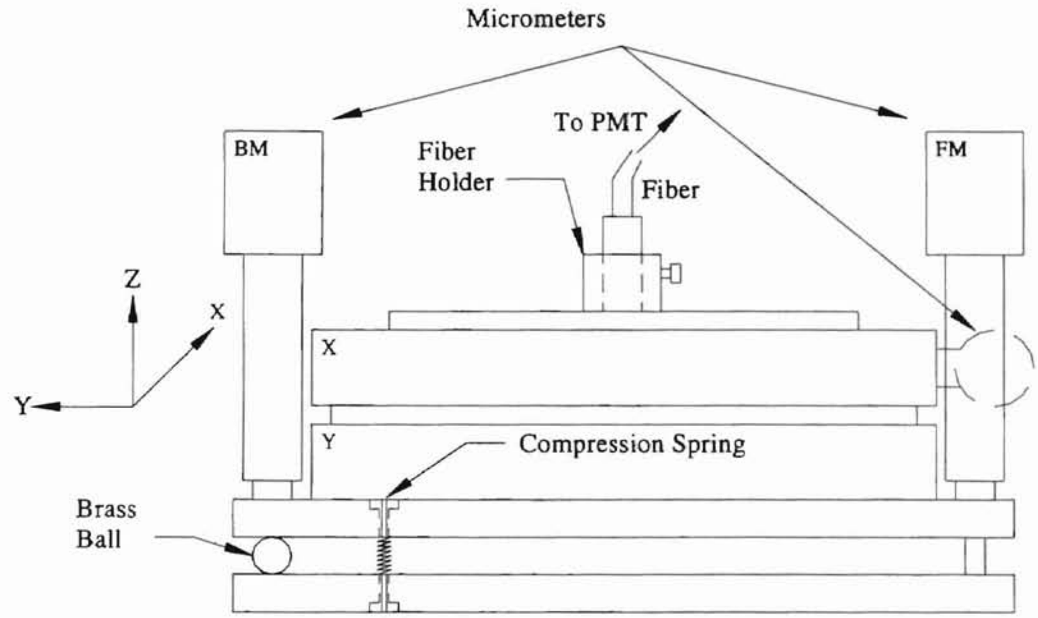

Figure 9: Side view of the top fiber mount. X and Y denote the direction each translation stage moves, while BM and FM denote the back and the front micrometers respectively [Cambern (1999)].

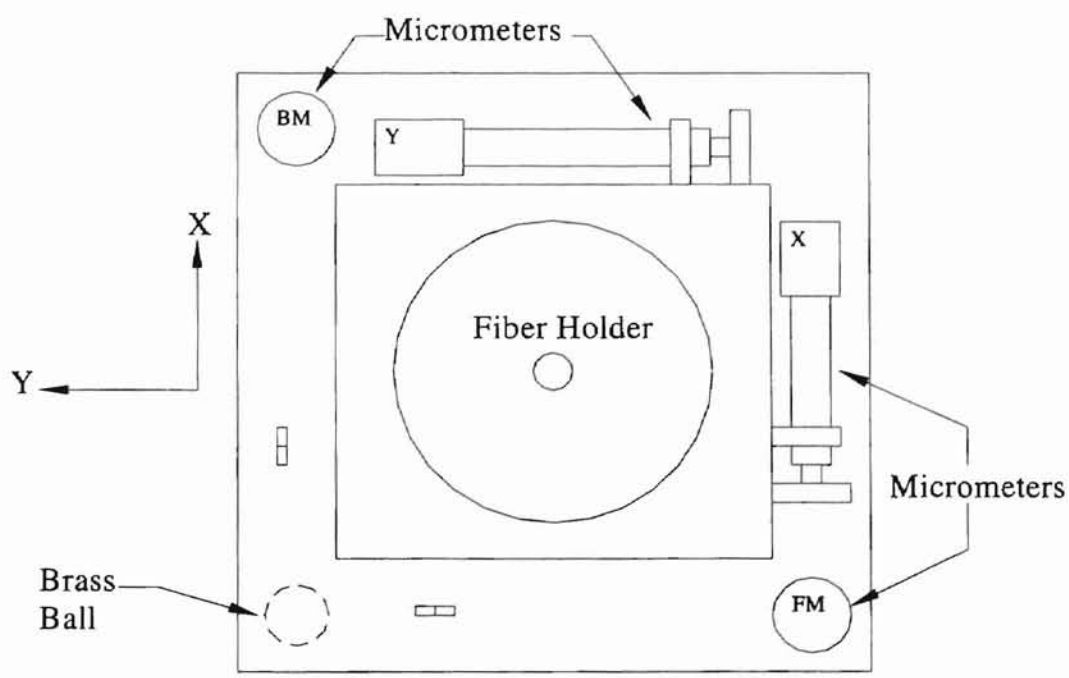

Figure 10: Top view of the top fiber mount. BM, FM, X and Y are repeated from Fig. 9 [Cambern (1999)].

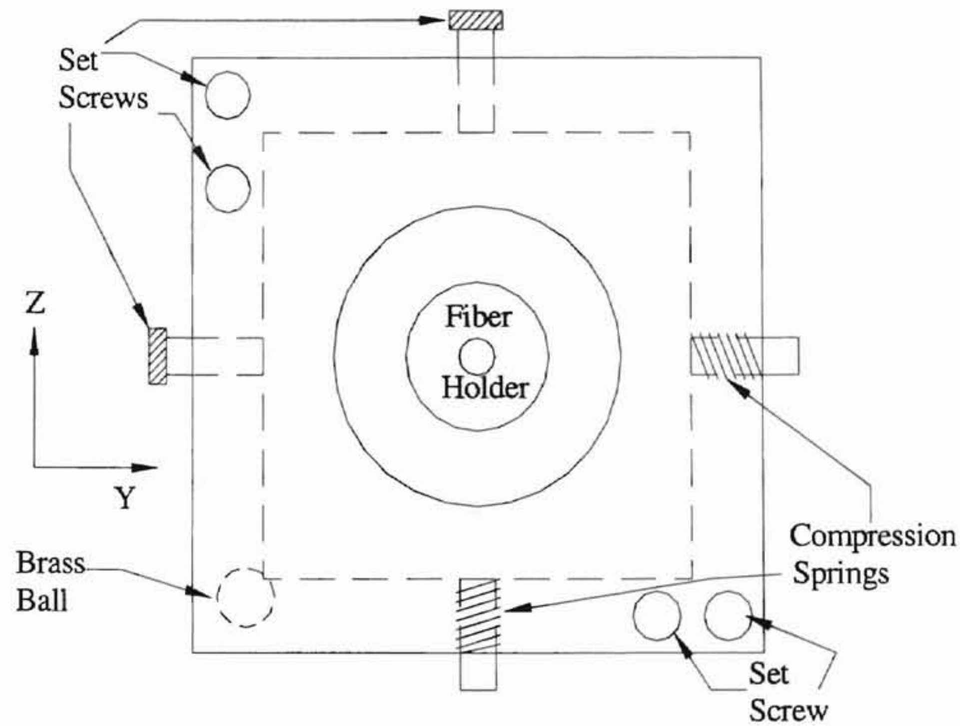

Figure 11: Back view of the rear fiber mount [Cambern (1999)].

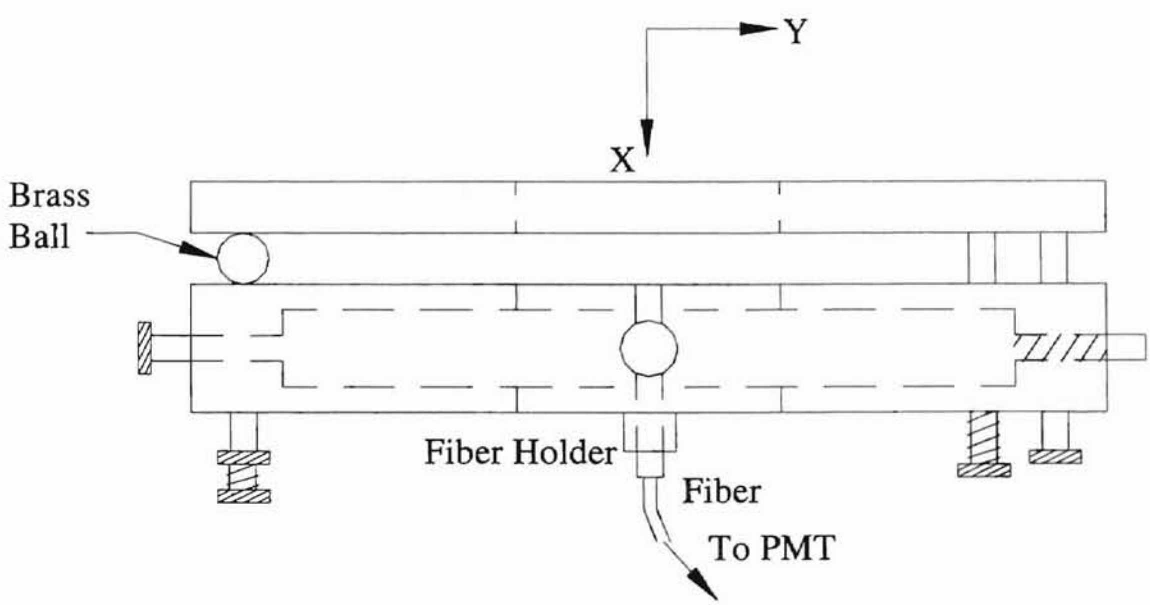

Figure 12: Top view of the rear fiber mount [Cambern (1999)].

CHAPTER V

FLOWING CASE: EXPERIMENTAL SETUP AND PROCEDURE

5.1 Introduction

This chapter will focus on the second objective of this research, viz., flow effects suppression. The second section of this chapter will give a detailed idea of the equipment used for the flow experiments. The third section of the chapter will explain the calculation of the scattering angle for the experiments, based on the angles of the laser and the detector arms with respect to the normal to the direction of flow. The calculations made for some of the flow parameters will also be presented in the third section. The fourth section of the chapter will describe in detail the alignment procedure to be followed. The fifth section of the chapter will be devoted to the experimental procedure adopted for the experiments conducted.

5.2 Experimental Setup

The main components involved in the experimental setup can be classified into five groups, viz., the goniometer, the light source, the detection devices, the sample, and the flow system. Figure 13 shows a schematic of the experimental setup used for the flow experiments. Details of the components will be provided in this section.

Goniometer

The goniometer for the flowing system was designed differently than that for a non-flowing system. This was because, in the case of the flowing system, both the laser and the detector arms had to be mobile, in order to implement the technique of flow effect suppression. The goniometer was designed and built by the Chemistry and Physics Machine Shop at Oklahoma State University.

The goniometer was made of aluminum, and consisted of a body that housed two cylindrical shafts, and two rectangular arms for holding the laser and the detection devices. Figure 14 shows a schematic of the goniometer. The body of the goniometer was a hollow rectangular frame measuring 43.5 cm high, 23.5 cm wide, and 12.7 cm deep. The thickness of the frame was 2 cm. The frame housed two cylindrical shafts made of aluminum. The outer shaft was hollow and its dimensions were 6.35 cm outer diameter, 2.86 cm inner diameter, and 16.5 cm height. The solid inner shaft's dimensions were 2.54 cm diameter, and 17.5 cm height. The inner shaft and the outer shaft were held concentric by the use of ball bearings which separated them.

A rectangular arm of dimensions 61.2 cm long, 3.7 cm wide, and 2 cm thick was attached to the outer shaft, and held the laser and its accessories. A similar arm, measuring 67.2 cm long and attached to the inner shaft, held the detection equipment. Two stepper motors (see Appendix I) were attached to the inner shaft and the outer shaft to rotate them in a controlled manner. The stepper motors were also housed within the rectangular frame, with the laser arm stepper motor attached to the outer shaft from the bottom, while the detector arm stepper motor was attached to the inner shaft from the top. The laser arm and the detector arm were held at heights of 26 cm and 31 cm from the experiment table respectively. The two arms were supported at the free ends by cylindrical shafts of 1.9 cm diameter, and fitted with rollers for easy movement of the arms on the experiment table. The laser and the detector arms could travel over a range of 0° to 48° about the axes of the shafts, henceforth referred to as 'the axis' of the goniometer.

Light Source and Its Accessories

The light source used for the flow experiments was a Neodymium-Yttrium-Silver (Nd: YAG) laser (see Appendix I). The laser operated at a wavelength of 532.5 nm in a vacuum, and the total power of the laser beam was 100 mW. The vertically polarized green beam had an original diameter of 0.70 mm [Melles-Griot catalog (1995/96)]. The laser was held by an aluminum holder and was capable of being moved vertically and horizontally along the length of the laser arm. The eye of the laser was 49 cm above the experiment table, and a distance of 45.5 cm from the axis (see Fig. 13).

The attenuator, lens and lens holder used for the flow experiments were the same as that used for the non-flow experiments. The attenuator was mounted on the laser arm a distance of 37.5 cm from the axis of the goniometer. The lens was mounted on the laser arm at a distance of 4.5 cm from the axis (see Fig. 13).

Detection Devices

The detection devices used for the flow experiments were basically the same as those used for the non-flow experiments. The detector unit used to hold the beam splitter, optical fibers, and motion control devices for the optical fibers, was the same as that used for the non-flow experiments. The base of the detector unit was 44.5 cm above the experiment table. The same two photomultiplier tubes were used for the flow experiments also.

A multi-band, non-polarizing beam splitter specified for 532.5 nm wavelength was used for the flow experiments. The beam splitter divided the beam into two beams of approximately equal intensity ($45 \pm 5\%$). The beam splitter was located at a distance of 32 cm from the axis.

Two single mode optical fibers (see Appendix I) specified for the 532.5 nm wavelength were used to transmit the detected signal to the photomultiplier tubes.

The polarizer was mounted at a distance of 27.5 cm from the axis on the detector arm (see Fig. 13).

Sample Cell Holder

Figure 15 illustrates the sample stand and its components. The sample cell holder used for the flow experiments was designed to hold a long sample cell of rectangular cross-section. The holder was mounted on a teflon rotating stand of dimensions 76 mm diameter and 8 mm thickness. The stand was capable of being rotated through an angle (δ) from -60° to $+60^\circ$. This helped in studying the effects of flow when the flow vector was not perpendicular to the angular bisector between the incident beam and the scattered beam vectors. The rotatable stand was mounted on a dovetail slide, which was fitted with a micrometer so that the slide could be moved in a direction normal to the direction of flow. The dovetail slide moved inside a base of thickness 14 mm, and the base was mounted on top of the goniometer. The micrometer on the dovetail slide helped measure the depth of the overlap area between the incident beam and the detection cylinder inside the test cell. Details of the sample cell and holder are given by Cambern (1999).

The sample cell (Fig. 15) used for the flow experiments had a rectangular cross-section and had dimensions of 6 mm width, 8 mm height, and 30.5 cm length with 0.9 mm wall thickness. The sample cell was made of quartz (see Appendix I).

Flow System

The flow system was an important component in the flow experiments. The flow system was composed of two holding tanks, the sample cell, a shuttle pump, and tygon tubing. Figure 16 shows a diagram of the holding tanks, lid, and gasket as viewed from the side. The two holding tanks had rectangular cross-sections and had dimensions of 215 mm length, 49.5 mm width, and 69.5 mm thickness, with 12 mm side-wall thickness, and 9 mm bottom plate thickness. The tanks had a capacity of 250 ml each. The tanks were made from plexiglass and had large lids with openings for fluid inlet and fluid outlet. The lid was closed on the tanks by means of 21 screws evenly spaced along the sides of the rectangular top.

The fluid was pumped by means of a shuttle pump (see Appendix I). The pump was capable of pumping at a maximum rate of 25 ml/min. This pump was chosen because the pumping mechanism would not damage the small sub-micron particles used in the tests.

The pump, holding tanks and the sample cell were connected using tygon tubing of dimensions 1.59 mm inner diameter and 3.18 mm outer diameter as shown in Fig. 17. More details on the flow system can be found in Cambern's (1999) thesis.

The particles used for the experiments were uniform polystyrene latex microspheres. Latex particles having diameters of 0.107 μm, 0.098 μm, and 0.203 μm (see Appendix I) were used for the flow experiments.

Angular Calibration of Table

The table on which the experimental apparatus was mounted was calibrated in order to determine and repeatedly return to the angular locations of the laser and the detection arms with respect to the normal. The marking was done by first placing the sample rotating stand at an angle of 0°, and a mirror was placed in the sample holder. The laser arm was aligned until the beam was reflected back to the eye of the laser by the mirror. This position corresponded to the normal direction to the flow vector, or the angles $\alpha_L = \alpha_D = 0^{\circ}$. Once this position was marked on the table, the table was marked for various angles by moving the appropriate arm through various angles using the stepper motor. This process was repeated to verify the accuracy of the measurements. As a further check, the linear distances between the normal line and the rollers attached to the bottom of the support shafts of the laser and detector arms were measured, for various equal angles of α. The results agreed well with each other to an accuracy of 1°. The computer code used to run the stepper motor is included in Appendix V. From the calibration, the maximum angles of the laser and the detector arms were found to be 48° and the minimum angles to be 15°.

5.3 Calculation of Flow Parameters

Scattering Angle Calculations

It is very important to know the scattering angle in order to predict the particle radii from the field correlation function. The scattering angle, θ, is the angle made by the detected beam with the transmitted incident beam. For the flow geometry, calculation of the scattering angle is complicated by the refraction effects at the air-glass and the glass-water interfaces. Figure 18 illustrates the scattering angle for the flow geometry. The scattering angle is calculated as follows. The calculation assumes that the cell walls are parallel.

From Snell's Law, for the laser beam

$$n_A \sin(\alpha_L) = n_W \sin(\beta_L) \tag{5-1}$$

where n_A is the refractive index of air, n_W is the refractive index of water, and the suffix L refers to the angular directions to the incident laser beam. Rearrangement of terms yields

$$\beta_L = \sin^{-1}\left(\frac{\sin(\alpha_L)}{n_W} n_A\right) \tag{5-2}$$

By a similar procedure, the angle for the detected beam can be found as:

$$\beta_D = \sin^{-1}\left(\frac{\sin(\alpha_D)}{n_W} n_A\right) \tag{5-3}$$

From the scattering angle geometry shown in Fig. 18,

$$\pi - \theta + \frac{\pi}{2} - \beta_D + \frac{\pi}{2} - \beta_L = \pi \tag{5-4}$$

Rearranging Eq. (5-4) yields

$$\theta = \pi - \beta_L - \beta_D \tag{5-5}$$

From Eqs. (5-2), (5-3), and (5-5), it is possible to calculate the actual scattering angle for any combination of laser and detector angles. But since this research is concerned with the suppression of flow effects, it is important that the laser and detector angles be equal, with the result that $\beta_L = \beta_D$. Table 2 lists the values of the scattering angles (computed from Eq. (5-5)) corresponding to the various equal angles of laser and detector arms.

Table 2: Summary of Scattering Angles Calculated for Selected Equal Angles of Laser and Detector Arms.

$\alpha_L = \alpha_D$		$\beta_L = \beta_D$	θ	$\alpha_L = \alpha_D$		$\beta_L = \beta_D$	θ
(Degrees)	(Radians)	(Degrees)	(Degrees)	(Degrees)	(Radians)	(Degrees)	(Degrees)
10	0.1745	7.5021	164.9958	31	0.5411	22.7833	134.4334
11	0.1920	8.2484	163.5032	32	0.5585	23.4804	133.0392
12	0.2094	8.9936	162.0127	33	0.5760	24.1736	131.6528
13	0.2269	9.7376	160.5248	34	0.5934	24.8627	130.2745
14	0.2443	10.4802	159.0395	35	0.6109	25.5476	128.9048
15	0.2618	11.2214	157.5572	36	0.6283	26.2280	127.5441
16	0.2793	11.9610	156.0780	37	0.6458	26.9037	126.1926
17	0.2967	12.6990	154.6021	38	0.6632	27.5746	124.8508
18	0.3142	13.4351	153.1298	39	0.6807	28.2405	123.5190
19	0.3316	14.1693	151.6614	40	0.6981	28.9011	122.1978
20	0.3491	14.9015	150.1970	41	0.7156	29.5562	120.8875
21	0.3665	15.6315	148.7370	42	0.7330	30.2057	119.5886
22	0.3840	16.3592	147.2815	43	0.7505	30.8492	118.3015
23	0.4014	17.0846	145.8309	44	0.7679	31.4866	117.0267
24	0.4189	17.8073	144.3854	45	0.7854	32.1176	115.7647
25	0.4363	18.5274	142.9452	46	0.8029	32.7420	114.5160
26	0.4538	19.2446	141.5107	47	0.8203	33.3595	113.2811
27	0.4712	19.9589	140.0822	48	0.8378	33.9698	112.0604
28	0.4887	20.6701	138.6599	49	0.8552	34.5727	110.8547
29	0.5061	21.3780	137.2441	50	0.8727	35.1678	109.6644
30	0.5236	22.0824	135.8352				

Flow Parameter Estimation

Some flow parameters were estimated for the experiments. Among the first parameters to be calculated were the flow rate and the average velocity of the flow at different pumping rates. Some other parameters that may be of interest to this research were also calculated. This included the Reynolds number of the flow and the hydrodynamic entry length for this configuration.

The flow rates at different pumping speeds were calculated by performing a flow experiment without the cycle being closed, i.e., using a calibrated beaker at the discharge end instead of the second holding tank. The time taken to fill a known volume was used to calculate the flow rate, and the average flow velocity was calculated using the following equation.

$$v_{avg} = \frac{\dot{Q}}{wh} \quad (5\text{-}7)$$

where $\dot{Q}$ is the calculated flow rate, w is the width of the test cell (6 mm), and h is the height of the test cell (8 mm). Calculations for the maximum velocity at each flow rate are explained in detail in Cambern (1999). Table 3 summarizes the flow rate and average velocity of flow corresponding to the various pump settings, viz., 0%, 50%, 75%, and 100% flow.

Table 3: Summary of Determination of Flow Rates and Flow Velocities for Various Pump Settings [Cambern (1999)].

Pump Setting (% of Maximum Flow)	Measured Flow Rate (mm^3/s)	Average Calculated Velocity (mm/s)
0%	0	0
50%	157.67	3.28
75%	251.11	5.23
100%	373.39	7.78

Based upon the average velocity at full flow, the Reynolds number for the flow configuration was determined from the following equation [White (1991)].

$$Re_{D_h} = \frac{v_{avg} D_h \rho}{\mu} \quad (5\text{-}9)$$

where D_h is the hydraulic diameter of the cross-section, ρ is the density of water (997.3 kg/m^3), and μ is the dynamic viscosity of water (1.002×10^{-3} Pa-s) at a temperature of 23°C.

The hydraulic diameter, D_h, was calculated using the equation

$$D_h = \frac{4\,(\text{Cross-Sectional Area})}{\text{Wetted Perimeter}} \quad (5\text{-}10)$$

$$= \frac{4(\text{width})(\text{height})}{2(\text{width} + \text{height})} = \frac{4(6\text{ mm})(8\text{ mm})}{2(6\text{ mm} + 8\text{ mm})}$$

$$D_h = 6.86\text{ mm}$$

The Reynolds number was then determined for the maximum value of average velocity, which corresponded to a pump setting of 100% flow.

$$Re_{D_h} = \frac{(7.779\text{x}10^{-3}\ \frac{\text{m}}{\text{s}})\,(6.857\text{x}10^{-3}\text{ m})(997.3\,\frac{\text{kg}}{\text{m}^3})}{1.002\text{x}10^{-3}\text{ Pa - s}}$$

$$Re_{D_h} = 53.09$$

This value of Reynolds number corresponded to highly laminar flow. Transition to turbulence occurs at a Reynolds number of about 2300 [White (1991)]. Based upon the Reynolds number, the hydrodynamic entrance length could be calculated. The hydrodynamic entrance length is the distance from the start of the tube, along the direction of flow, to the point (location) where the flow becomes fully developed, and there is no further change in the velocity profile along the direction of flow. It was important for the flow to be fully developed in the detection volume. The hydrodynamic entrance length was determined from the following equation [White (1991)].

$$Le_v = 0.05\,D_h\,Re_{D_h} \tag{5-11}$$

$$= 0.05\ (6.86\text{ mm})\,(53.09)$$

$$Le_v = 18.21\text{ mm}$$

Since the detection volume was located approximately at the lengthwise center of the cell along the direction of flow (~ 150 mm), the flow was fully developed in this region.

5.4 Alignment Procedure

Alignment was critical for the flow experiments to the same extent that it was for non-flow experiments. As mentioned in Section 3.4, the flow velocity vector had to be perpendicular to the angular bisector between the incident beam and the scattered beam vector, in order to suppress the effects of flow. The alignment procedure for the flow experiments was, in some respects, similar to that of the non-flow experiments, which was described in Section 4.3.

As the first step in the alignment procedure, the laser arm was brought to an angle of 0^o, where it was perpendicular to the test cell. A mirror was placed in the test cell holder to help in the alignment process. The laser was aligned such that the beam reflected from the mirror hit the eye of the laser. When this step was completed, the laser was considered to be aligned horizontally and vertically with respect to the test cell holder. Then the laser was moved to the user-chosen angle α_L (following marks on experiment table described in Section 5.2), where the experiment was to be performed. The detector armed was moved to an equal marked angle, α_D, in the opposite direction, so that the perpendicularity condition required for flow suppression was maintained (see Fig. 13). The back and the top optical fibers were then aligned so that the light coming out through them was brightest, first by visual judgement, and then using a power meter, as described in Section 4.3. The mirror was then removed.

The attenuator and the polarizer were then mounted on the laser arm and detector arm, respectively. Next, the test cell was placed in the test cell holder, such that the 8 mm side was facing the laser beam. The optical fibers were connected to the PMTs, the correlator program ALV-5000 was initialized, and the program's count rate display mode was enabled.

Since the test cell had a rectangular cross-section, the specular reflections from the front and back walls of the cell could be intercepted by the detectors when properly aligned. This reflected light was too strong for the PMTs, and also caused unscattered light to mix with scattered light reaching the detectors, known as heterodyning. Heterodyning was an undesirable phenomenon for these experiments, and had to be eliminated. This was accomplished by rotating the normal to the vertical face of the test cell downward by a small angle (~ 5^{o}), about the longest geometric axis of the test cell (in the direction of flow). When this was done, the specular reflections were aimed below the field of view of the detectors. This however, did not completely eliminate the problem. A second measure had to be adopted in order to suppress the reflections further.

But before that, the test cell had to be aligned so that the detection area was inside the test cell, instead of being at either of the cell walls. This was arranged by running an auto-correlation on channel 0 in the correlator program. The test cell was moved toward the laser in a direction perpendicular to the longest axis of the cell, using the test cell depth micrometer (see Fig. 15), until the Y-intercept of the auto-correlation function climbed from a value of ~ 0.0 (no correlation), to a value of ~ 0.95 (very high correlation). This implied that the detectors were "seeing" scattered light from inside the sample, instead of just reflections from the cell wall which do not correlate at all.

As an additional measure to suppress specular reflections, two thin strips of black electric insulation tape (~ 2 mm wide), were attached to the test cell holder, so that reflections from the test cell walls were blocked by the pieces of tape. Figure 19 shows a schematic specifying the position of the electrical tape used to block reflections. To ensure that the tape blocked only the reflections and not much of the scattered light itself, the count rate display mode of the program was used when the strips of tape were attached. When the reflections were blocked, the count rates dropped from several hundred to approximately 100 kHz. Blocking the scattered light caused the count rate to drop to almost 0 kHz.

The pump was turned on, and set to the flow rate desired for the experiment. The lens was the next component to be aligned. The lens was mounted on the laser arm a distance of 40 mm from the test cell wall (see Fig. 13) measured along the direction of the incident beam. The lens was aligned horizontally, vertically, and in a direction along the length of the laser arm using position control setscrews on the lens holder, until the count rate was the highest. This ensured that the narrowest part of the beam was in the detection area.

Finally, the top fiber was aligned such that the Y-Intercept of the cross-correlation function was its highest (~ 0.90), by the same procedure described in Section 4.3. When the top fiber alignment was completed, all of the micrometer readings were recorded in the lab notebook, and the experiment was ready to begin.

5.5 Experimental Procedure

The experimental procedure described in this section concerns the study of flow effects suppression by maintaining the angular bisector between the incident laser beam and the detected beam, perpendicular to the flow velocity vector. Experiments were performed at various angular locations of the laser and the detector arm in order to study their effects on the particle radii predicted.

Scattering Angle Sweep Experiments

Preliminary experiments were conducted on very dilute samples, in order to study the effects of varying the angular locations of the laser and the detector arms. This was checked to see if, at various angles of $\alpha_L = \alpha_D$, the particle radii were predicted accurately, as long as the perpendicularity condition was met.

Once the setup was aligned, the laser and the detector arms were moved to the desired angles $\alpha_L = \alpha_D$. The ALV program was placed in the count rate display mode, and the two strips of black tape were placed on the test cell holder in such a way that the tape blocked the specular reflections. The appropriate scattering angle (Table 2) was input to the ALV program. The pump was off (0% flow rate), and auto-correlation runs were on Channel 0 and on Channel 1. The duration of the runs was chosen to be 60 seconds. When the run was complete, the fit was determined, the data was saved, and the results were recorded as outlined in Section 4-4. Runs were made at pump settings of 50% and 100% flow. The same procedure was repeated for 40°, 30°, and 20° laser/detector angles ($\alpha_L = \alpha_D$).

Particle Sizing Experiments

Experiments were performed in order to study multiple scattering suppression in flowing media, by performing a sweep of the angular separation from 0 to 10 mrads between the fibers viewing the scattering volume. Again, experiments were conducted at laser/detector angles of 40° and 30° ($\alpha_L = \alpha_D$), and at two flow rates (0% and 100%), in order to study the effect of multiple scattering suppression with increased angular separation (tilt) between the fibers.

The procedure was the same as that followed for the non-flowing case, and has been described in Section 4-4. At the α angle desired, the flowing case alignment procedure was followed. When the setup was aligned, the appropriate scattering angle was entered into the ALV program, and the runs made at each tilt angle. Experiments were performed on aqueous suspensions of polystyrene latex particles having diameters 0.098 μm, 0.107 μm, and 0.203 μm. The results of the experiments conducted will be discussed in detail in Chapter VI.

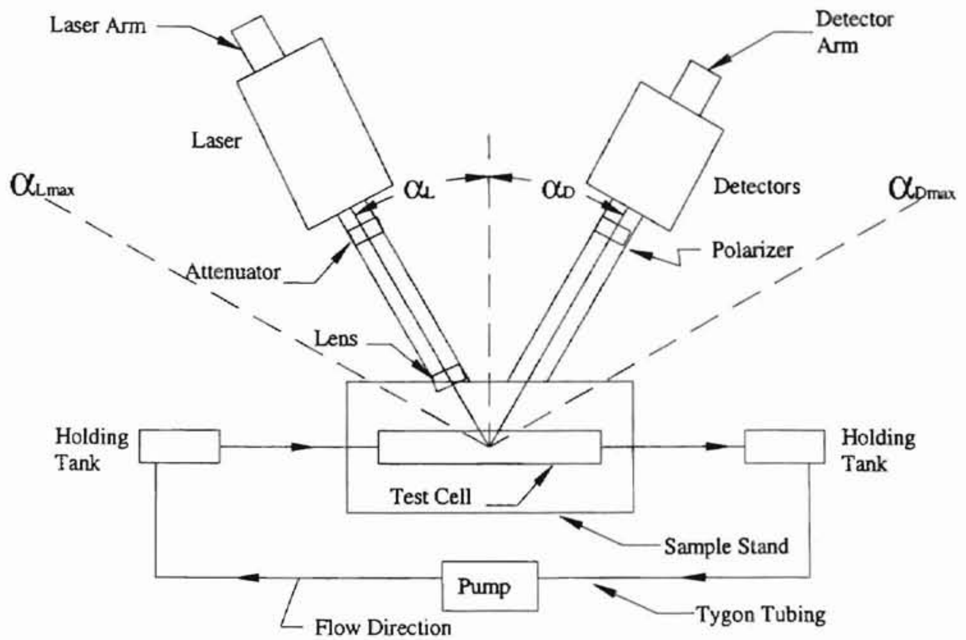

Figure 13: Schematic of the setup used for the flowing case experiments.

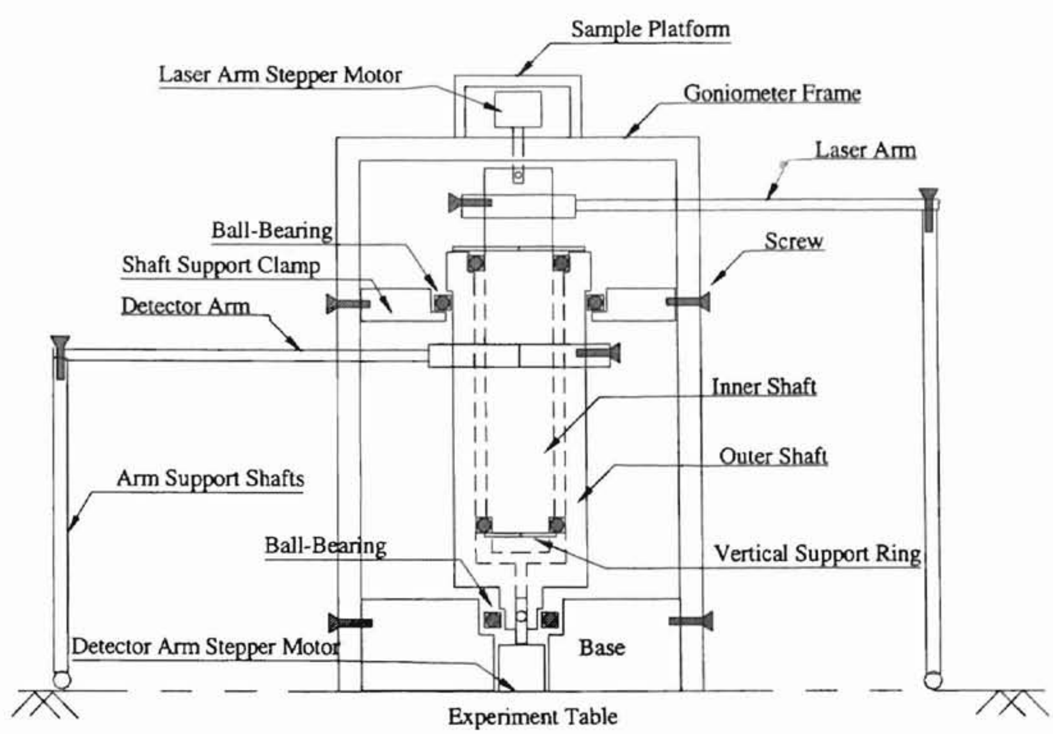

Figure 14: Diagram of the goniometer used in the setup for the flowing case experiments.

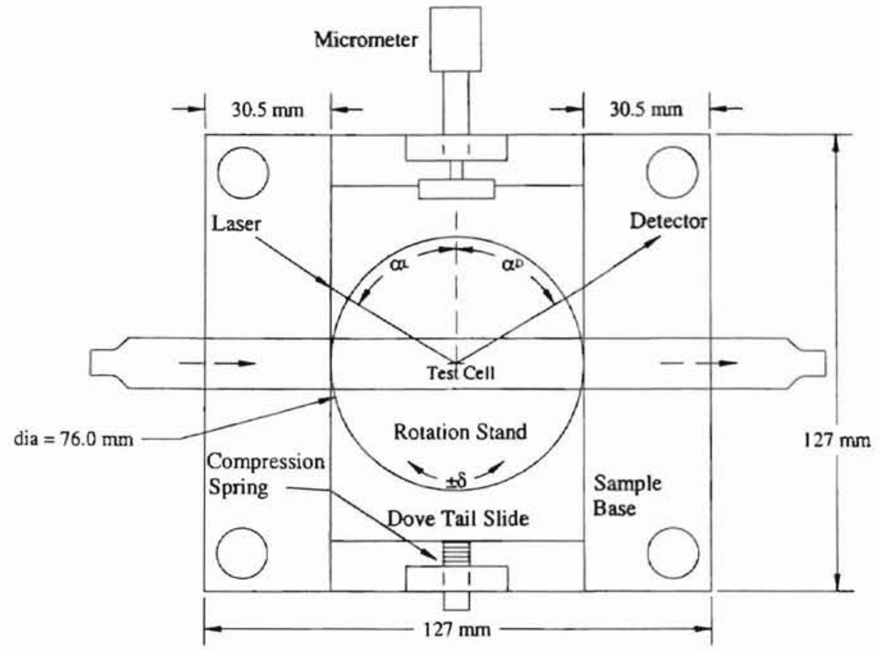

Figure 15: Diagram of the long rectangular test cell mounted on the rotation stand, showing the angle of rotation δ. A negative δ represented a rotation of the test cell toward the laser, while a positive δ represented a rotation toward the detector housing. Also shown is the dovetail used to move the test cell [Cambern (1999)].

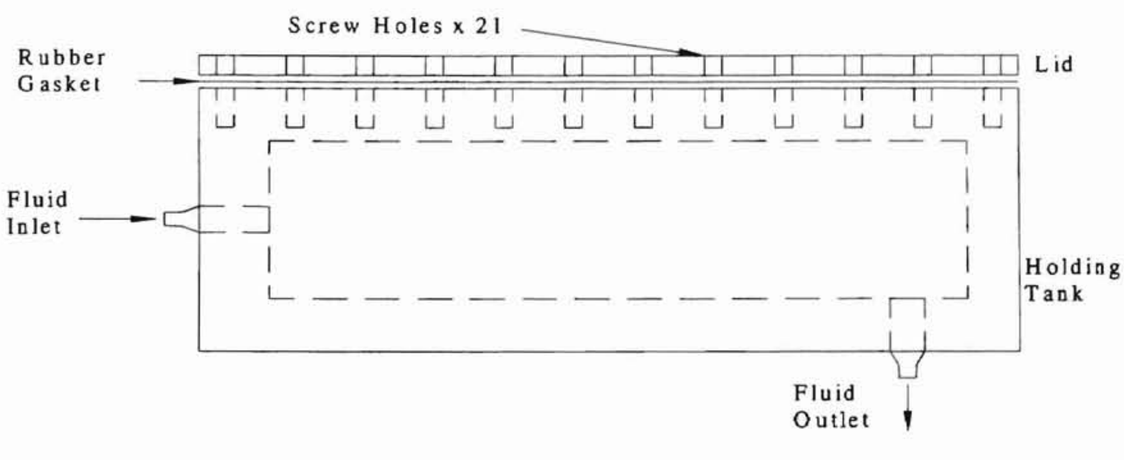

Figure 16: Side view of the holding tank, lid, and gasket used in the flow circuit [Cambern (1999)].

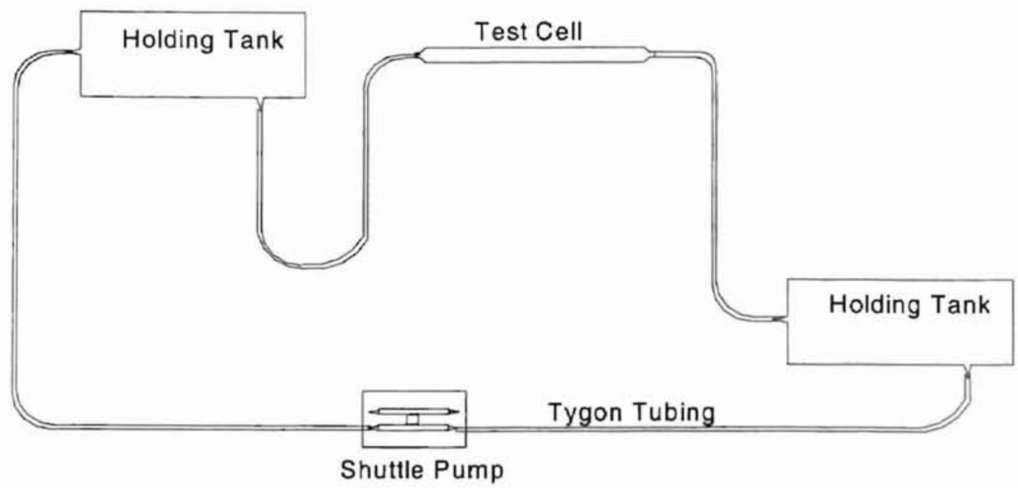

Figure 17: Schematic of the flow system with all components connected.

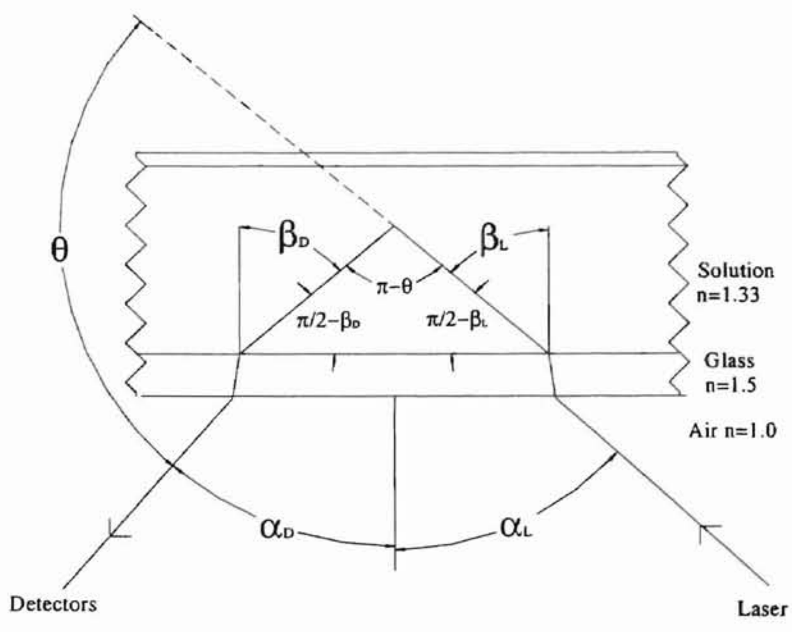

Figure 18: Scattering angle calculation for the flow geometry.

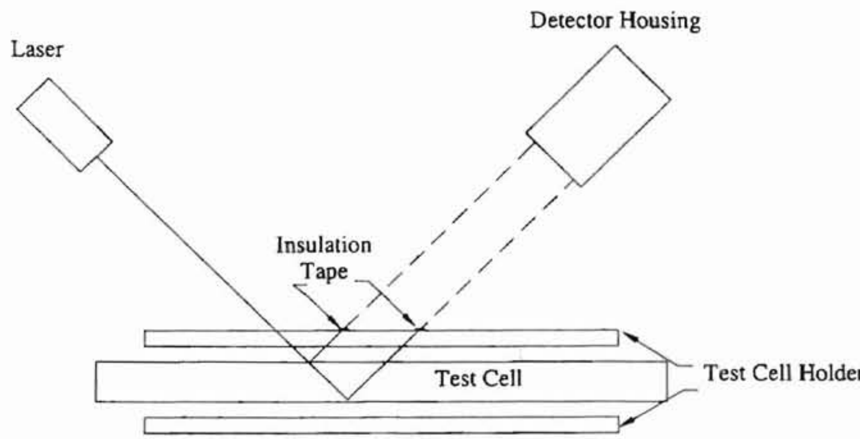

Figure 19: Schematic of the test cell and holder showing the positions of the black electrical tape used to block reflections.

CHAPTER VI

RESULTS AND DISCUSSION

6.1 Introduction

The aim of this research was to show the effectiveness of combining the two techniques of multiple scattering suppression and flow suppression to predict particle diameters accurately in dense, stagnant and flowing media. The one-beam, two-detector cross-correlation setup was used to suppress multiple scattering effects. To suppress flow effects, a flow geometry where the angular bisector between the laser and detector beams was perpendicular to the direction of flow was used. Experiments were performed on stagnant and flowing samples in order to verify the effectiveness of the techniques used. The results and a discussion of the trends seen will be the focus of this chapter. The second section will be devoted to the results obtained from the experiments conducted on non-flowing samples, where the effectiveness of the multiple scattering suppression technique will be discussed. The third section will be devoted to the results obtained from the experiments performed on flowing samples, where the effectiveness of the flow suppression technique used in conjunction with the multiple scattering suppression technique will be discussed. The fourth section will cover the work done in verifying the accuracy of the theoretical prediction of the S/N ratio [Nobbmann *et al.* (1997)] by comparing that theoretical ratio with experimental data.

6.2 Non-Flowing Case

The first objective of this research was to perform experiments on multiple scattering suppression in dense non-flowing (no macroscopic flow velocity) samples, in order to gain experience with the technique, and to further the work done by Nobbmann *et al.* (1997). Experiments were performed to determine the suppression of multiple scattering effects by mapping the signal-to-noise ratio (also known as Y-intercept) as a function of the angular separation between the two detectors viewing the scattering volume.

6.2.1 Preliminary Observations

Preliminary experiments conducted on non-flowing samples did not yield good results, and predicted the radii incorrectly, and inconsistently. The results obtained were analyzed, and the analyses led to the discovery of eight important characteristics of the setup that were very critical for the success of the experiments. A list of the characteristics follows. The first four are discussed in detail herein, while the last four are covered by Cambern (1999).

1. Experiments at scattering angles less than 60° were difficult, because of uncontrollable intensities detected due to direct transmission from the sample.
2. The positioning and alignment of the lens was critical to the success of the experiments.
3. The positioning of the detectors was critical to the success of the experiments.

4. Larger diameter particles were found to be difficult to size, because of hydrodynamic settling, which led to deviation of behavior from pure Brownian motion.
5. Flaws in the beaker used to hold the water bath interfered with the data collection.
6. Both detectors should be aligned properly at the scattering angle at which the experiment was to be performed. This was accomplished by aligning both of the detectors for maximum intensity, at a scattering angle of 0^{o}. Then channel 1 was aligned at the scattering angle at which the experiment was to be performed, by maximizing the Y-intercept.
7. After each tilt in a Y-intercept mapping experiment, the top fiber should be translated to maintain the intensity of channel 1.
8. For the multiple scattering suppression technique to work efficiently, the detection area of both the fibers should overlap the area through which the incident beam passes in the sample. To meet this requirement, all of the components should be in the same horizontal plane.

The first characteristic that was observed in the setup was that at scattering angles lower than 60^{o}, the experiments were very difficult to perform, because of uncontrollable intensities detected due to direct transmission from the sample. This could be observed in the form of higher fluctuations in the count rates detected (approximately 50 kHz as against approximately 20 kHz seen at higher scattering angles). This caused difficulty in maintaining the intensity level of channel 1 after each tilt, and hence contributed to the erratic nature of the results observed. The increase in intensities for channels 0 and 1 at

15° was found to be 4.40 and 4.81 times the values measured at 120° respectively [Cambern (1999)].

The second characteristic that was observed was that the position and the alignment of the lens (see Fig. 13) were critical for the success of the experiments. The lens helped to focus the beam inside the sample. The effective diameter of the speckle pattern increases in a direction transverse to that of the beam propagation, as the diameter of the beam decreases. To obtain the best results, the detection areas must overlap in the 'waist' (24 μm diameter) of the beam. Section 6.3 presents a case, where multiple scattering effects were not effectively suppressed because the detectors were not viewing the focused part of the beam.

The third characteristic that was observed was that the position of the detector was critical to effective suppression of multiple scattering effects. As described in Section 3.3, multiply scattered light will be correlated over a smaller distance transverse to the direction of beam propagation, when compared to that of singly scattered light. To obtain a strong cross-correlation between the two detected signals, the detectors should be placed at an optimum distance from the sample in the direction of the scattered beam. From experiments conducted, a distance of 44.5 cm between the closest vertical surface of the beam splitter and the center of the sample (the axis), was found to be ideal.

The fourth characteristic that was deduced from the experiments was that larger particles (diameter greater than 0.3 μm) tended to settle out of the suspension, because of their weight. Particle sizing experiments are based on an assumption of random Brownian motion of particles in suspension. Larger particles settling out of the suspension could cause deviations from the assumed random Brownian behavior, and could cause incorrect prediction of radii. Smaller sized particles behaved more randomly, and exhibited Brownian motion characteristics. Consequently, best results were obtained with 0.107 μm diameter particles.

The four characteristics described here and the other four detailed by Cambern (1999) helped to establish clear experimental procedures, which were critical for the success of the experiments, and were meticulously followed in all of the experiments.

6.2.2 Y-intercept Mapping Experiments

The underlying theory behind the multiple scattering suppression experiments, as described in Section 3.3, is based on the fact that singly scattered light results from the volume of the laser beam, whereas the overwhelming majority of multiply scattered light stems from the halo surrounding the incident beam. Multiply scattered light will be correlated only over a smaller distance transverse to the direction of beam propagation, when compared to that of the singly scattered light. To suppress multiple scattering effects, two detectors should be placed with sufficiently large angular separation between them, such that one of the detectors is viewing the multiple scattering region, and the other is viewing the single scattering region. It is important to know the extent of angular separation needed between the detectors, before multiple scattering ceases to be correlated.

To determine the effect of suppression of multiple scattering effects, cross-correlation experiments were conducted following the procedure described in Section 4.4, and the Y-intercept and the predicted radii were plotted as a function of tilt angle between the detectors. Experiments were conducted on polystyrene latex particles of 0.107 μm diameter, using a test cell of square cross-section (Appendix I), at a scattering angle of 90°. The volume fractions used were 0.15%, 0.32%, and 0.43% by weight. (Meyer *et al.* (1997b) conducted similar experiments at volume fractions ranging from 0.0017 to 5% by weight (see Section 2.3)). Cambern (1999) provides results of similar experiments to those presented herein, conducted at scattering angles of 30°, 45°, 60°, 90°, and 120°, using a test cell of circular cross-section.

Figure 20 shows the Y-intercept versus tilt angle sweep for the three different volume fractions listed. The Y-intercept for the three volume fractions peaked near 0.90. At a volume fraction of 0.32%, the effects of multiple scattering suppression are clearly seen, with the multiple scattering correlating strongly within a tilt angle separation of ±1.0 mrad, corresponding to the 'peak' of the Y-intercept curve. Beyond an angular separation of ±1.0 mrad, single scattering is correlated strongly, as is evident from the low value of the Y-intercept. These correspond to the 'shoulders' of the curve. A very similar behavior is seen of the 0.43% volume fraction also.

When viewed as a function of volume fraction, the lower volume fraction shows a broader peak and the shoulders start out at a higher Y-intercept than a higher volume fraction. This is because of the lower extent of multiple scattering (and correspondingly, a higher amount of single scattering) associated with a lower volume fraction. Conversely, a higher volume fraction would mean more multiple scattering, and so a narrower peak, and shoulders starting out very low on the Y-intercept. This is clearly the behavior exhibited at the 0.43% volume fraction. The extent of the shoulder is short for the 0.43% volume fraction (about 5 mrad) because the Y-intercept died out very rapidly and so useful data could not be collected beyond the extent noted.

Figure 21 shows the corresponding plots of predicted radii as a function of tilt angle for the three volume fractions. Comparing the three volume fractions, it can be seen that as the volume fraction increases, the amount of multiple scattering increases, leading to increased decay rates of the correlation function, and resulting in lower prediction of radii in the multiple scattering regime. Consequently, 0.43% volume fraction starts off at the lowest radius, 18 nm at a tilt angle of 0 mrad. The intermediate volume fraction (0.32%) starts at a radius of 26 nm, and the lowest volume fraction (0.15%) starts at a radius of 44 nm. Also, the lowest volume fraction required a smaller angular separation between the fibers before the multiple scattering effects were substantially suppressed. Once the required angular separation was reached, the predicted radii were within the range specified by the manufacturer of the particles.

The Y-intercept mapping experiments were repeated at each of the three volume fractions, and the results of the repeated and the original experiments agreed very well. Figure 22 shows the Y-intercept versus tilt angle mapping for the 0.15% volume fraction for the original and the repeated experiments. The results of the two experiments can be seen to agree very well with each other. Results of the repeated experiments for the 0.32% and the 0.43% volume fractions can be found in Appendix III.

6.3 Flowing Case

The second objective of this research was to extend the technique of multiple scattering suppression to flowing media. As the first step, the effectiveness of the flow suppression theory was studied by experimenting on dilute flowing suspensions, to see if flow suppression could be done. The results of these experiments will be discussed in Section 6.3.1. Once this was established, experiments were performed on dense samples of flowing suspensions, in order to verify the effectiveness of the multiple scattering suppression and the flow suppression theories when they are used in conjunction with each other. The results will be discussed in Section 6.3.2. Experiments performed on larger particles (0.3 μm diameter and larger) were not successful. The reason for the failures with the larger particles was studied theoretically. The results of the larger particle study will be discussed in Section 6.3.3.

6.3.1 Flow Suppression Experiments

Auto-correlation experiments were performed on dilute flowing suspensions, in order to study the effectiveness of the theory in suppressing the effects of flow. The experimental setup was aligned as described in Section 5.4. Auto-correlation runs using channel 1, were made at 100% flow rate, for various equal angles of laser and detector arms, viz., 40°, 30°, and 20° (scattering angles of 122°, 136°, and 150° respectively). The condition that the flow vector should be perpendicular to the angular bisector between the laser and the detector arms, was maintained for each of the three angles. The particle sizes used were 0.107 μm and 0.204 μm. The normalized field auto-correlation function (g^1) was plotted for each of the angles. The values of the g^1 function were obtained from the values of the normalized intensity correlation (g^2) function, given by the ALV–5000 software, using the relation given in Eq. (3-5),

$$g^1(\tau) = \sqrt{g^2(\tau) - 1} \quad (6\text{-}1)$$

assuming $\gamma^2 = 1$. The g^1 function is then related to the radius of the particle through the diffusion constant as given by Eq. (3-12).

$$g^1(\tau) = \exp\left(-2D_0 q^2 \tau + i\vec{\mathbf{q}} \cdot \vec{\mathbf{v}}(r)\tau\right) \quad (3\text{-}12)$$

Figure 23 shows a plot of the g^1 function (on a natural logarithmic scale) versus product of q^2 and delay time for auto-correlation experiments done using channel 1 on 0.107 μm particles at 100% flow rate. The correlation functions are found to be linear for all three angles. This exponentiality gives rise to more accurate calculation of the diffusion constant, and hence, more accurate prediction of particle radius. It can be interpreted from Eq. (3-12) that in the absence of the flow term, also known as the Doppler beating term, the g^1 function is exponential. This clearly demonstrates the suppression of flow effects by the experimental setup geometry. Figure 24 shows a plot of the g^1 function versus product of q^2 and delay time for 0.204 μm particles at 100% flow rate. In this case too, the correlation functions are found to be linear for all the three sets of angles. One characteristic to be noted here is that the slope of the g^1 function for 0.204 μm particles is less than that for 0.107 μm particles. This means that the correlation function decays slower for larger particles. The linearity of the functions for both the particle sizes reinforces the fact that the flow geometry used is very successful in suppressing flow effects.

Attempts were made to perform experiments on 0.304 μm diameter particles. But the count rates measured at these scattering angles were too low (about 5 kHz) to record any useful data. The reason for this behavior is explained using the Rayleigh-Gans form factor, in Section 6.3.3.

Experiments were conducted to study the effects of violating the flow geometry by tilting the test cell about the axis, both towards the laser arm and towards the detector arm. From the results of the experiments it was seen that for tilt angles (δ) up to 5°, the g^1 function was exponential. At angles of δ greater than 5°, significant non-exponentiality was observed in the g^1 function, which showed the influence of the flow term on the g^1 function. The results of these experiments are presented in detail by Cambern (1999).

6.3.2 Y-intercept Mapping Experiments

Toward fulfillment of the second objective of this research, the multiple scattering suppression theory was extended to flowing fluids, eliminating flow effects using the flow suppression theory. The need for the Y-intercept mapping experiments has already been justified in Section 6.2.2 for the non-flowing case.

Preliminary experiments conducted for the flowing case yielded an insight into some important characteristics of the flowing setup. One important characteristic that was noted was that the position and the alignment of the lens were critical to the success of the experiments. Figure 25 shows a plot of the Y-intercept versus tilt angle for 0.107 μm particles at a volume fraction of 0.198% and a flow rate of 50%. The angles of the laser and detector arms were 40°, and the scattering angle was 122°. The two curves correspond to the map before and after the lens was aligned in the direction of the laser beam.

When the lens is aligned properly in the direction of the laser beam, the detectors are looking at the most focused part of the beam. The plot shows how the Y-intercept curve had no shoulder when the lens was not aligned, and the curve had a noticeable shoulder when the lens was aligned properly. Figure 26 shows the corresponding plot of the radii versus the tilt angle. The result seen is self-explanatory. When the lens was badly focused, not only was the span of useful data very short, but also, the radius predicted was never accurate. When the lens was properly focused, the span of useful data increased to over 4.5 times. Also the radius was predicted correctly and stayed within the range specified by the manufacturer of the particles, once the shoulder was reached at a tilt angle of about 1.0 mrad. The results of the experiment clearly emphasized the importance of aligning the lens correctly.

Y-intercept mapping experiments were conducted on flowing suspensions to study the effects of four parameters on particle sizing. The parameters are flow velocity, scattering angle, particle size, and particle concentration. The effects of the first two parameters are discussed here, and that of the third and the fourth parameters are discussed in detail by Cambern (1999) but will be briefly discussed here later in this section.

Flow Velocity

Three different particle sizes were studied in order to examine the effect of flow velocity on particle sizing. Figure 27 shows the Y-intercept versus tilt angle mapping for 0.107 μm particles at a volume fraction of 0.198 percent. The angles of the laser and detector arms are 40°, which correspond to a scattering angle of 122°. The incident beam and the detected beams intersect at a distance of about 0.5 mm from the outer wall of the test cell, as measured by the test cell depth micrometer. The curves correspond to three different flow rates, viz., 0%, 50%, and 100% flow rates.

From the plot, no major differences are seen between the three curves. They all start at a peak value of about 0.90, and are identical to the extent that, the span of useful data collected is about 8 mrad for all three flow rates. However, the effect of flow rate is clearly seen in the plot of radius versus tilt angle for the same experiments, which is presented in Fig. 28. It can be seen that, as flow rate increased, the radius predicted in the multiple scattering area of the plot was lower. Consequently, at higher flow rates, it required a larger angular separation between the detectors before multiple scattering ceased to be correlated, and the radius was predicted accurately. Once the curve encountered the shoulder, the radius stayed within the manufacturer's specified range.

The effect of increase in flow rate is, by behavior, analogous to the increase in multiple scattering. The reason for this behavior was deduced to be that, even though the resultant scattering wave vector was perpendicular to the velocity vector, not all the intermediate scattering wave vectors were perpendicular to the velocity vector. As a result, the Doppler beating term in Eq. (3-12) was not fully suppressed. The residual flow effect caused a non-exponentiality in the g^1 function, and hence led to a lower prediction of radius.

A similar effect can be observed in Fig. 29 which shows a plot of the radius versus tilt angle for 0.098 μm particles at a volume fraction of 0.86 %, and laser and detector angles at 30° (scattering angle is 136°). The test cell depth is again 0.5 mm, and two different flow rates, viz., 0% and 100%, are compared. Figure 30 shows a plot of the radius versus tilt angle for 0.203 μm particles at a volume fraction of 0.20 %, scattering angle of 136°, and a test cell depth of 0.5 mm. This plot also exhibits the same effect observed in the other two plots. The radius starts out lower at a higher flow rate, and it takes a greater tilt angle between the detectors before multiple scattering ceases to be correlated, and particle sizing becomes accurate. But these particles seem to have the problem that the radius predicted was always higher than the manufacturer's specification. This can be explained as follows.

The manufacturer's estimate of the particle size was based on a technique known as Transmission Electron Microscopy (TEM) [Duke Scientific Corp. (1997)]. In this technique, the particles are dried, and their sizes are then determined using an electron microscope. However, when the particles are suspended in solution, they tend to absorb water and swell, which makes their sizes appear bigger than specified by the manufacturer. Absorption of water increases with particle size, which explains the fact that size discrepancies were observed in only larger particles. A very similar explanation can also be found in Aberle *et al.* (1998).

Plots of Y-intercept as a function of tilt angle corresponding to Figs. 29 and 30 are presented in Appendix IV.

Scattering Angle

The effect of scattering angle was studied by varying the angle between the laser and detector arms, and the normal to the flow velocity ($\alpha_L = \alpha_D$). The flow geometry required to suppress the effects of flow was maintained. Figure 31 shows a plot of the Y-intercept versus tilt angle for 0.107 μm particles at a volume fraction of 0.198 percent. The test cell depth was about 0.5 mm, and the flow rate is 0 %. The three sets of laser and detector angles ($\alpha_L = \alpha_D$) studied were 48°, 40°, and 30°. From the plot, it can be seen that for all three angles, the peak starts out around 0.90. But with reducing angle, the curve tends to become steeper. Also, the span of useful data reduces with reducing angle. This seems to suggest that as α decreases, the amount of multiple scattering effect seen increases, but the converse is what is actually true as can be seen from the plots of the radius.

Figure 32 shows a plot of the radius versus tilt angle for the same experiments. Here it can be seen that as α decreases, the radius starts out higher, and with increasing α, the amount of tilt angle between fibers increases before particle size is predicted correctly. This is analogous to a decrease in multiple scattering. This can be explained as follows. When α is decreased, it corresponds to the laser and the detector arms moving closer to each other. Since the lens is aligned at each of the angles, the alignment causes the overlap area between the laser and the detector beams to be closer to the cell wall. Since the overlap area is closer to the cell wall at low angles of α, most of the scattered light that is detected will come from single scattering, as the incident light beam has not traveled far enough inside the sample to suffer multiple scattering. This explains the higher prediction of radius at lower values of α. Here too, it can be noted that, once the curve encounters the shoulder, the size remains within the expected range. It can be seen that at an α angle of 30^o, the predicted radius is within the specified range throughout. This is due to the absence of any flow (which is analogous to decreased multiple scattering as explained earlier), combined with the lower multiple scattering seen at that angle, because of the overlap area being close to the cell wall.

The reason for the Y-intercept curve becoming steeper with decreasing angles can be attributed to the fact that since the detection area is closer to the cell wall at lower angles, there is a higher possibility of detecting noise along with the useful signal, which reduces the signal-to-noise ratio.

Figure 33 shows the plot of radius versus tilt angle for 0.107μm particles at a volume fraction of 0.198%. The flow rate is 100%, and the test cell depth is 0.5 mm. This plot also shows a trend similar to that shown in Fig. 32. The radius starts out lower than in Fig. 32. But here too, with lower values of α, the radius is higher. The latter statement agrees with the explanation already offered. The lower value of radius when compared to Fig. 32 is due to what has been already explained in the study of flow effects in this section.

A very similar behavior can be seen in Fig. 34, which shows a plot of the radius versus tilt angle for 0.098 μm particle at a volume fraction of 0.86 percent. The flow rate is 100%, and the test cell depth is 0.5 mm. Results for two values of α are compared here, viz., 48°, and 30°. The trend is very similar, but between Figs. 34 and 33, the radius starts at a lower value for the higher volume fraction. This is clearly due to the increased multiple scattering effect.

Figure 35 shows the radius versus tilt angle for 0.203 μm particles at a volume fraction of 0.20 percent. The flow rate is 100%, and the test cell depth is 0.5 mm. Here again, two angles of α are compared, viz., 48° and 30°. The trend exhibited is very similar to that seen in Fig. 33, but the radii predicted are higher than the manufacturer's specification, as explained earlier in this section. Plots of the Y-intercept as a function of tilt angle corresponding to Figs. 33, 34, and 35 are presented in Appendix IV.

The experiments conducted gave a clear insight into the feasibility of multiple scattering suppression extended to flowing fluids by the implementation of the flow suppression theory. The effects of parameters like particle size and particle concentration on particle sizing were also studied. With an increase in concentration, there is an increase in multiple scattering, which results in lower prediction of particle radius [Cambern (1999)]. With increasing particle size, the radius predicted is higher than the manufacturer's specified range, and the value of the radius predicted becomes unstable because of hydrodynamic settling. Details of the study are discussed by Cambern (1999).

6.3.3 Rayleigh-Gans Form Factor

Experiments on larger particles (0.304 μm diameter and larger) could not be performed, because of the extremely low intensity levels obtained from scattering. This resulted in the lack of a noticeable correlation between the signals. The reason for the low scattered intensities was studied using the Rayleigh-Gans form factor.

According to the Rayleigh-Gans-Debye theory, the scattered intensity of a spherical particle of radius r_p, assuming low probability of multiple scattering is given as

$$I \propto r_p{}^6 P(qr_p) \tag{6-2}$$

where q is the magnitude of the scattered wave vector given by Eq. (3-9). $P(qr_p)$ is the particle form factor [Ackerson (1986)]. The particle form factor is given by the relation

$$P(qr_p) = \frac{3}{(qr_p)^3}\{\sin(qr_p) - [(qr_p)\cos(qr_p)]\} \tag{6-3}$$

Figure 36 shows a plot of the particle form factor $P(qr_p)$ on a logarithmic scale as a function of qr_p. The curve shows distinct maxima and minima. From the graph, it can be seen that, for larger particles, most of the light is scattered in the forward direction (in the general direction of the incident beam, see Fig. 3), corresponding to decreasing scattering angles. The minima of the graph are at values of $qr_p = 4.5, 7.7, 10.9, 14.1$, etc.

Figure 37 shows the particle form factor for 0.107 μm particles and a 532 nm laser wavelength, as a function of scattering angle, computed from Eq. (6-3). The curve is almost flat, with not much noticeable variation over a wide range of scattering angles. Figure 38 shows the particle form factor for 0.204 μm particles. This curve shows some significant drop in the form factor, from 0.0 to –1.0 on the logarithmic scale, at higher scattering angles. Figure 39 shows the particle form factor for 0.304 μm particles. The form factor suffers a considerable drop from 0.0 to –6.0 over the range of scattering angles. A minima is encountered at a scattering angle of 140°. For the flow setup used, the range of scattering angles was 112° to 150°. It is in the range from 122° to 150° that the form factor suffers a huge drop, which implies very low scattering intensities at these angles. One way to alleviate this problem is to design the setup to allow lower scattering angles than what is currently available. This becomes particularly important when working with larger particles which are more forward scattering, while at the same time using a setup that is designed for back scattering. A recommendation to this effect has been included in Section 7.2.

6.4 Theoretical Prediction of the Signal-to-Noise Ratio

One of the objectives of this research was to verify the accuracy of the prediction of the S/N ratio by the equation derived by Nobbmann *et al.* (1997), for a one-beam, two-detector, cross-correlation setup.

As described in Section 3.5, the equation for the S/N ratio, obtained after approximating and solving for the intensity correlation function, is the square of the second order complex degree of coherence γ, where

$$\gamma(\phi)=\frac{\dfrac{A}{B}\dfrac{\exp\left(\dfrac{-q^2\phi^2}{8\alpha_t}\right)}{\left(\alpha_t^{\,2}\left[\dfrac{\alpha_t\phi^2}{4}+\delta_t\right]\right)^{1/2}}+2\dfrac{\exp\left(\dfrac{-q^2\phi^2}{4\beta_t}\right)}{\beta_t\sin(\theta)\sqrt{\alpha_t}}}{\dfrac{A}{B\alpha_t\sqrt{\delta_t}}+\dfrac{2}{\beta_t\sin(\theta)\sqrt{\alpha_t}}} \tag{3-16}$$

β_t is the square of the inverse of the beam waist radius in the sample. α_t is the square of the inverse of the detection cylinder radius. δ_t is the square of the radius of the multiple scattering volume in the sample. θ is the scattering angle, and ϕ is the tilt angle of separation between the detectors. A:B is the ratio of multiple to single scattering in the sample. q is the scattering wave vector given by Eq. (3-9).

For the non-flowing experimental setup used in this research, the parameters are calculated. The parameter β_t is calculated as follows. The focused spot radius is given by the expression [Melles-Griot catalog (1995/96)]

$$w_f = \frac{\lambda f}{\pi w_0} \tag{6-4}$$

where f is the focal length of the lens used (f = 4.0 cm), and w_0 is the radius of the $1/e^2$ irradiance contour at the plane where the wavefront was flat. The incident beam radius, w_0 is 0.34 mm. The wavelength of the laser beam, λ is 632.8 nm. The focused spot radius w_f, also known as the 'waist' of the beam can be calculated to be 0.0237 mm. Since β_t is the square of the inverse of the beam waist radius, the value of β_t is calculated to be $18 \times 10^8/m^2$.

The parameter α_t is calculated as follows [Nobbmann *et al.* (1997)]. The detector field-of-view is approximated as a cylinder and has a diameter given by the product of the fiber divergence angle (1.5 mrad), and the fiber distance (73 cm) from the sample center. The radius of the detection cylinder is calculated to be 0.5625 mm. α_t is then the square of the inverse of the detection cylinder radius and is calculated to be 3.3 x $10^6/m^2$.

The parameter δ_t is calculated as follows [Nobbmann *et al.* (1997)]. The multiple scattering volume in the sample can be approximated to be a sphere of diameter 1.0 cm (the diameter of the cylindrical test cell is 1.0 cm). Since δ_t is the square of the inverse of the radius associated with the multiple scattering volume, δ_t is found to be equal to 4 x $10^4/m^2$. This quantity is actually not a well-defined one. So, a value of δ_t (4 x $10^4/m^2$) corresponding to the maximum multiple scattering volume possible (all scattering is restricted to the test cell) is chosen for investigation purposes.

There are four parameters that influence the value of γ in Eq. (3-16), viz., α_t, β_t, δ_t, and A/B. In the following theoretical study, three of the four parameters were kept constant, and the fourth parameter was varied in order to study the effect of that parameter on the S/N ratio curve. The experimental data used for the verification was that for 0.107 μm particles at a volume fraction of 0.32 percent, square cell, non-flowing case, and a scattering angle of 90^o. (Refer to data compiled under Exp. 33 in Appendix – II.)

First, the effect of the parameter δ_t was studied. Figure 40 shows the plot of the S/N ratio (both experimental data and the theoretical curve) versus tilt angle. The value of β_t used was 4 x $10^8/m^2$, the value of α_t used was 6.1 x $10^6/m^2$, and A:B was 1:770. δ_t was varied from 1 x 10^4 to 18 x $10^4/m^2$. Since δ_t is a measure of the volume of multiple scattering in the sample, as expected, with increasing values of δ_t, the shoulders rise. This implies that as δ_t increases, the radius corresponding to the multiple scattering volume decreases. Consequentially the amount of single scattering increases, and causes the shoulders to rise. This effect is the same as that observed in Fig. 20. The reason for the absence of a long shoulder is because of the low value of β_t used, instead of the calculated value (18 x $10^8/m^2$) for the experiment. Since β_t is the square of the inverse of the beam waist radius, a low value of β_t corresponds to a poorly focused beam. This reduces the size of the single scattering speckle, and causes a short shoulder.

Figure 41 shows a plot of the S/N ratio (experimental and theoretical) versus tilt angle for the same experiment, with the β_t variation. The value of α_t was 6.1 x $10^6/m^2$, δ_t was 4 x $10^4/m^2$, and A:B was 1:770. The range of β_t values tried was 8 x 10^8 to 16 x $10^8/m^2$. It can be seen that, with increasing values of β_t, the shoulder seems to rise up. This can be attributed to the decreasing radius of the beam in the sample (because of the focus of the lens), causing a larger size of the single scattering speckle. This causes a better correlation of the single scattering signals, once the tilt angle separation required to suppress multiple scattering effects is reached.

Figure 42 shows a plot of the S/N ratio (experimental and theoretical) versus tilt angle for the same experiment, with the A:B variation. The value of α_t was 6.1 x $10^6/m^2$, β_t was 18 x $10^8/m^2$, and δ_t was 4 x $10^4/m^2$, and A was kept as 1.0. The range of B values tried was 1000 to 2400. With increasing values of B, the shoulder rises up, and the peak widens very slightly. This is because of the increased single scattering brought about by increasing the value of B. In a way, the increase in the value of B is analogous to the increase in value of δ_t. Both of the parameters cause a similar effect on the S/N ratio. This can be clearly observed when Eq. (3-16) is rearranged to yield

$$\gamma(\phi)=\frac{A\dfrac{\exp\left(\dfrac{-q^2\phi^2}{8\alpha_t}\right)}{\left(\alpha_t^2\left[\dfrac{\alpha_t B^2\phi^2}{4}+B^2\delta_t\right]\right)^{1/2}}+2\dfrac{\exp\left(\dfrac{-q^2\phi^2}{4\beta_t}\right)}{\beta_t\sin(\theta)\sqrt{\alpha_t}}}{\dfrac{A}{\alpha_t B\sqrt{\delta_t}}+\dfrac{2}{\beta_t\sin(\theta)\sqrt{\alpha_t}}} \qquad (6\text{-}5)$$

The similarity in the influence of the parameters δ_t and B can be seen in Eq. (6-5), where the quantity $B\sqrt{\delta_t}$ influences $\gamma(\phi)$ instead of either B or δ_t individually. The presence of the $\alpha_t B^2\phi^2/4$ term in Eq. (6-5) does not influence the value of the S/N ratio as much as the $B\sqrt{\delta_t}$ term in the light of the fact mentioned earlier. For a volume fraction of 0.32 % and a value of B = 2000, $\alpha_t B^2\phi^2/4$ is computed to be 64 x 10^6, while $B^2\delta_t$ is computed to be 16 x 10^{10}. This leads to the conclusion that when α_t, β_t, and ϕ are fixed, varying B or δ_t will yield almost the same value of $\gamma(\phi)$ as long as $B\sqrt{\delta_t}$ is a constant.

Since δ_t was not a well-defined quantity, a value of δ_t was arbitrarily chosen to be 4 x $10^4/m^2$, and the value of B that gave the best fit to the experimental data was determined, after all of the other parameters were fixed by calculation.

Figure 43 shows the S/N ratio for the non-flowing case involving 0.107 μm particles at a volume fraction of 0.32 %, square cell geometry, and a scattering angle of 90°. The values of the parameters used are as follows: β_t = 18 x $10^8/m^2$, α_t = 6.1 x $10^6/m^2$, δ_t = 4 x $10^4/m^2$. From the curve, a value of A:B = 1:2000 is a good fit to the experimental data (see Fig. 42 for comparison between different values of B).

Figure 44 shows a similar plot for a volume fraction of 0.15 %. The closest fit to the experimental data was obtained using a value of A:B = 1:3100. The theory does not predict the value of the S/N ratio very well for this low volume fraction case. Figure 45 shows the plot for a volume fraction of 0.43 %. The closest fit to the experimental data, was obtained using a value of A:B = 1:850. The theoretical prediction agrees with the trend of the curve, but the experimental peak is wider than that predicted by the theory. One of the shoulders is fit well by the theoretical curve. It should be stated here that the theoretical curve was shifted by 0.1 mrad to the right, to take care of the asymmetry of the experimental data.

Asymmetry in data could exist if the detectors were not aligned accurately to view the center of the incident beam. The laser beam is brightest at the center, and the intensity decreases radially from the center of the beam. When Y-intercept mapping is done, the top detector is tilted first, and then translated to maintain the count rate on channel 1. If the detectors were not aligned accurately to view the center of the incident beam at the start of the experiment, the translation required to maintain intensity at each tilt angle would not be the same on both shoulders which would account for the asymmetry of the data.

Figure 46 shows the plot for a volume fraction of 0.32 % for a circular test cell geometry, at a scattering angle of 90° [data obtained from Cambern (1999)]. For this case too (like the 0.43% volume fraction), the experimental curve is wider at the peak. The value of A:B used to fit the data was 1:1900. For a very similar volume fraction (see Fig. 43) of 0.32 % using the square test cell, the ratio of A:B of 1:2000 gave the best fit. This suggests that the test cell geometry does not greatly influence the ratio of multiple to single scattering obtained.

From the results of the investigation, it is evident that the theory predicts the trend of the S/N ratio reasonably well. Slight discrepancies exist between the exact nature of the theoretical and the experimental curves. This can be justified as due to the approximation used (a small focused laser beam, an intermediate detection width, and a large sample volume, i.e., $\beta_t >> \alpha_t >> \delta_t$) to evaluate the integral given in Eq. (3-15) to arrive at the equation for the S/N ratio. The results show that, as the volume fraction increases, the ratio of A:B corresponding to the ratio of the multiple to single scattering decreases; and for identical volume fractions, the test cell geometry does not influence the ratio of the multiple to single scattering. The study also shows that when α_t, β_t, and ϕ are fixed, varying B or δ_t will yield almost the same value of $\gamma(\phi)$ as long as $B\sqrt{\delta_t}$ is a constant. It would be interesting to verify the accuracy of the prediction of the theory, for the flowing case, to see if the flow affects the proportion of scattering seen, by fitting the experimental Y-intercept data presented by Cambern (1999) and in this thesis with Eq. (3-16).

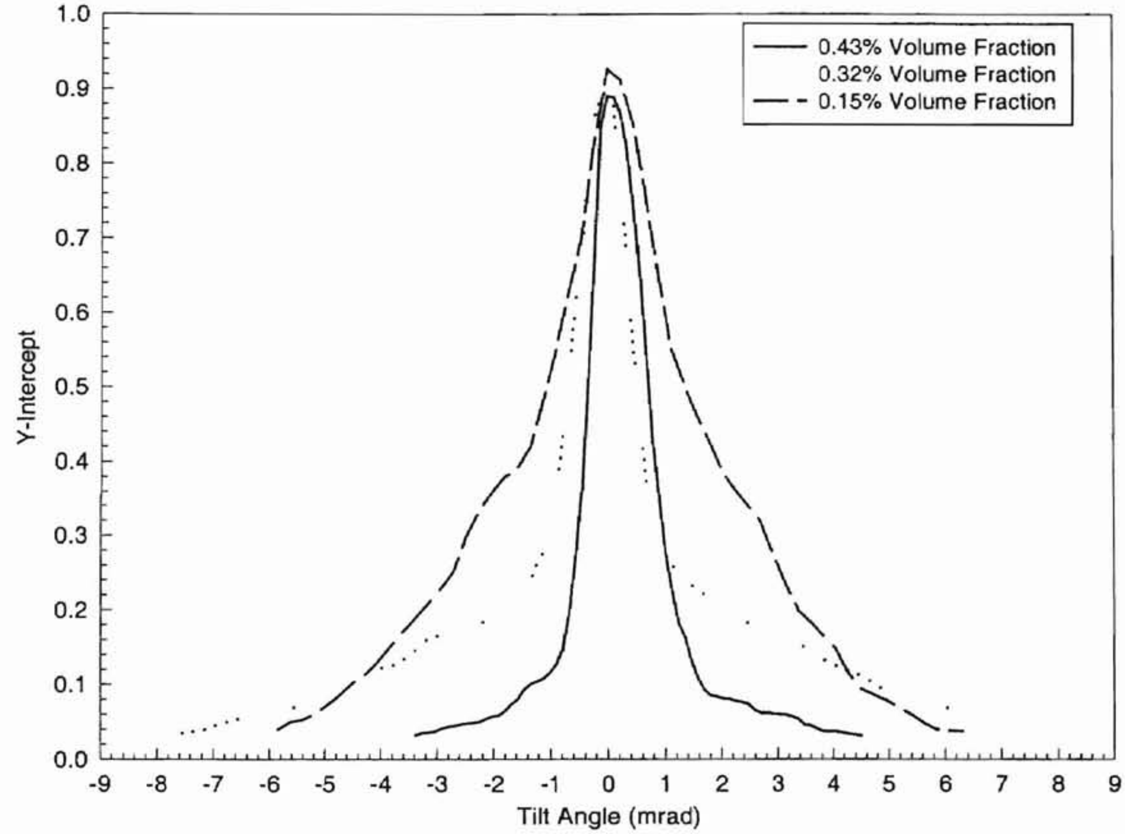

Figure 20: Y-intercept versus tilt angle mapping for 0.107 μm particles for the non-flowing case. A square test cell is used. Three volume fractions are compared here, viz., 0.15%, 0.32%, and 0.43%. The scattering angle is 90°. Data corresponds to experiments 33, 35, and 37.

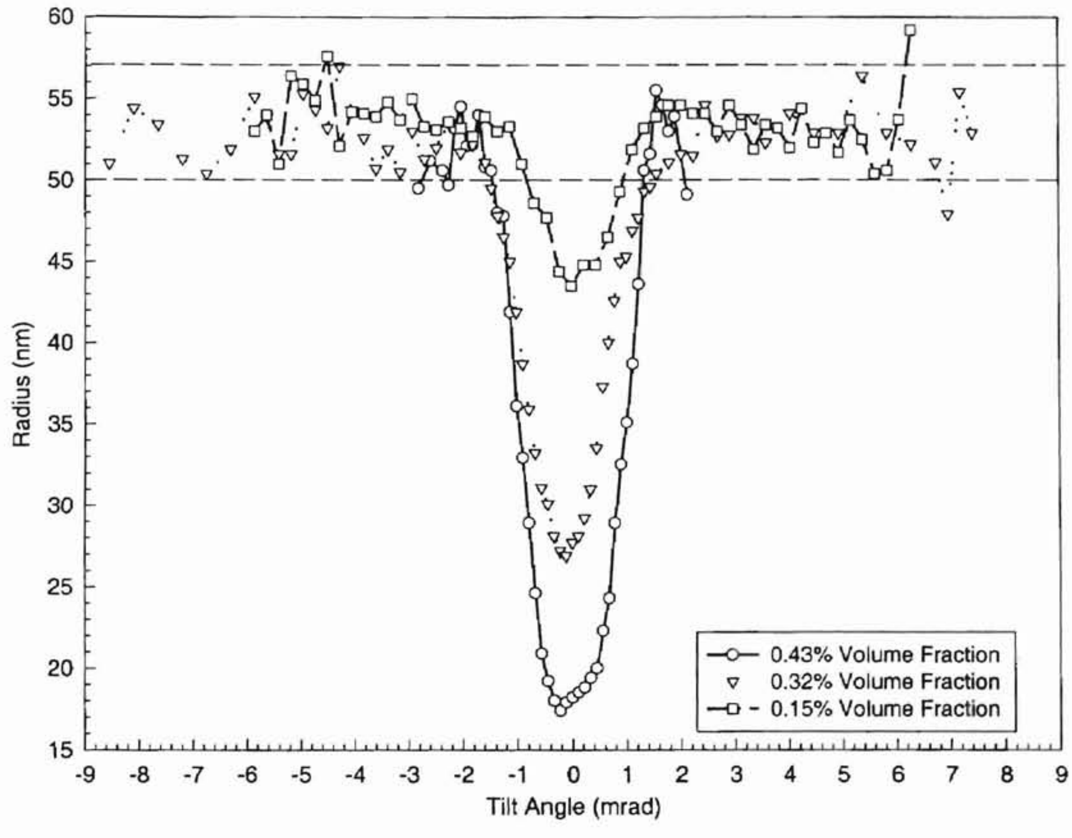

Figure 21: Radius versus tilt angle mapping plot corresponding to Fig. 20. The dashed lines indicate the range of expected particle size as specified by the manufacturer of the particles.

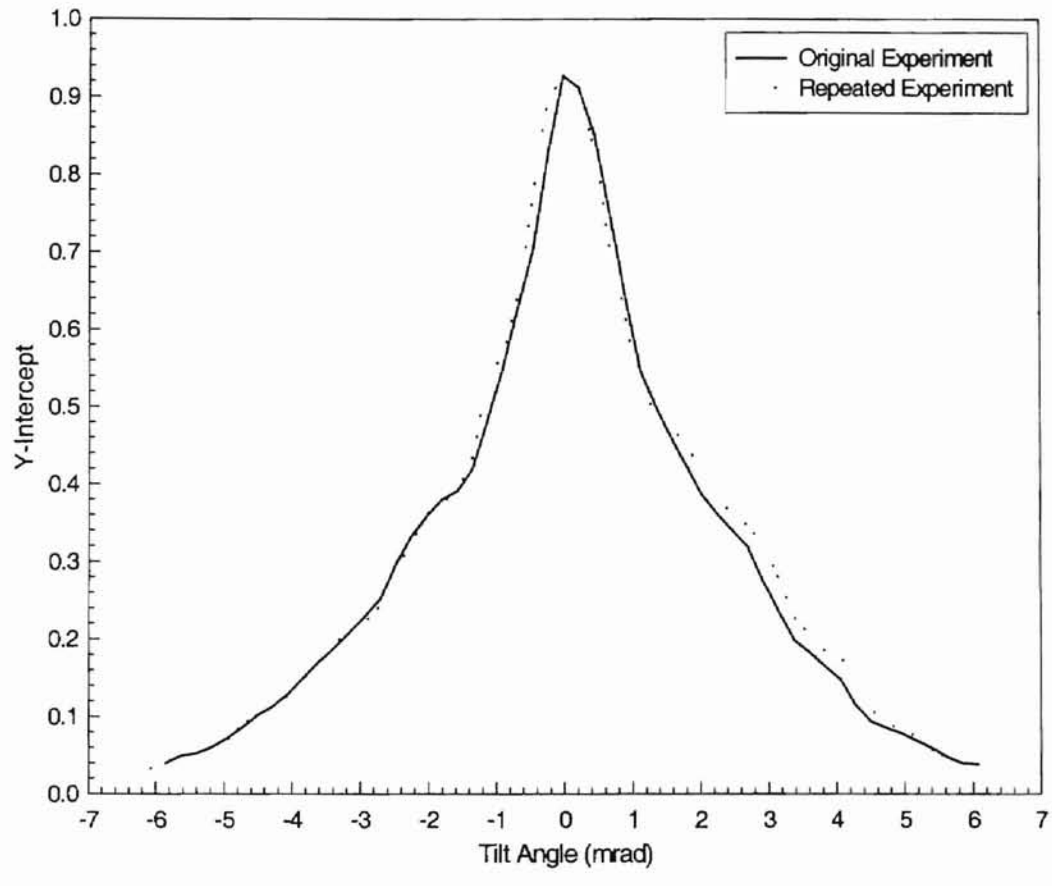

Figure 22: Y-intercept versus tilt angle mapping for 0.107 μm particles for the non-flowing case. A square test cell is used, and the volume fraction is 0.15 percent. The two curves correspond to the original experiment and the repeated experiment, conducted to verify the repeatability of the data. The scattering angle is 90°. Data corresponds to experiments 34 and 35.

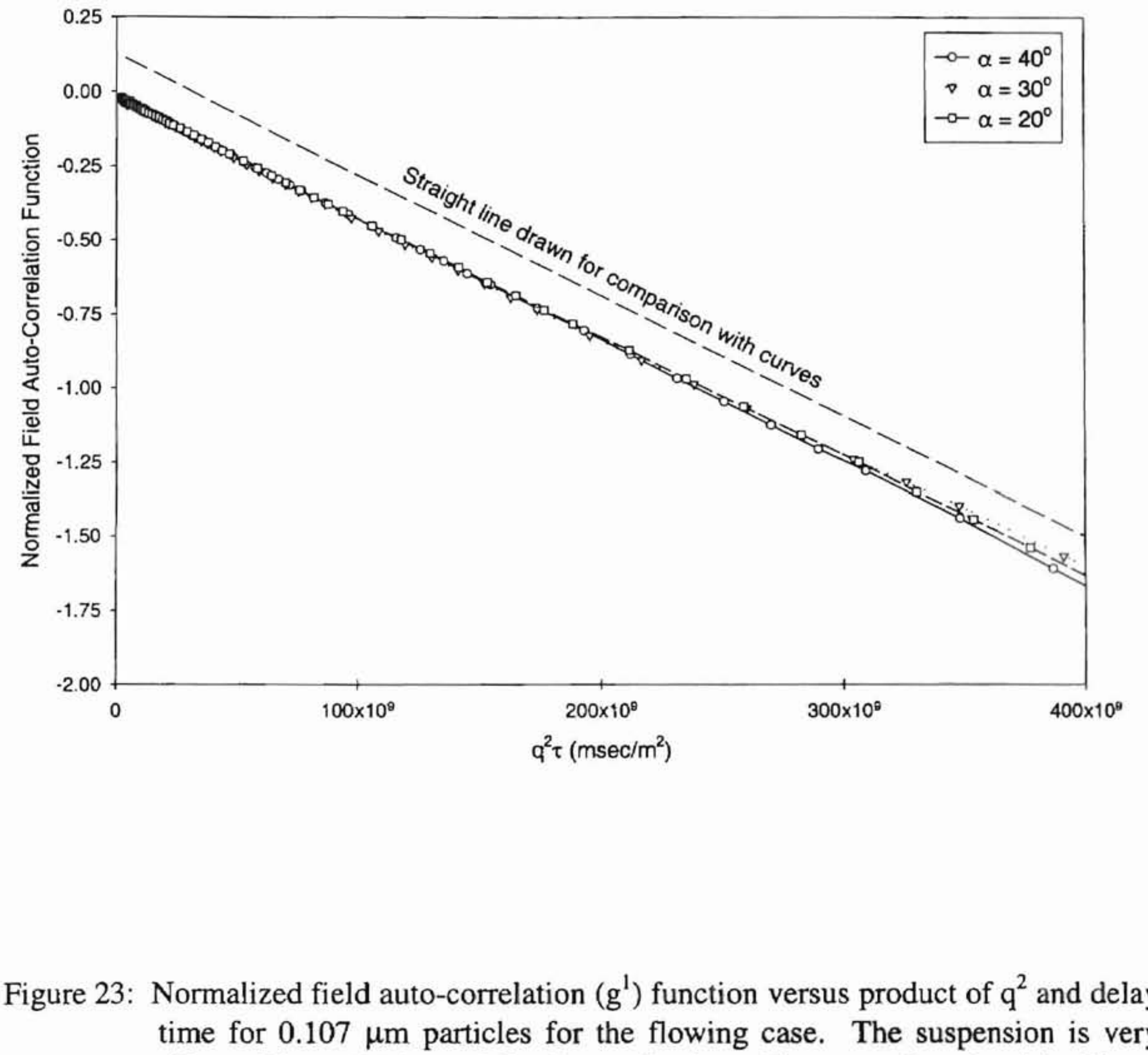

Figure 23: Normalized field auto-correlation (g^1) function versus product of q^2 and delay time for 0.107 μm particles for the flowing case. The suspension is very dilute. Channel 1 is used for data collection. Three equal angles (α) of laser and detector arms are compared, viz., 40°, 30°, and 20°. Corresponding scattering angles are 122°, 136°, and 150°, respectively. Data corresponds to experiment 59.

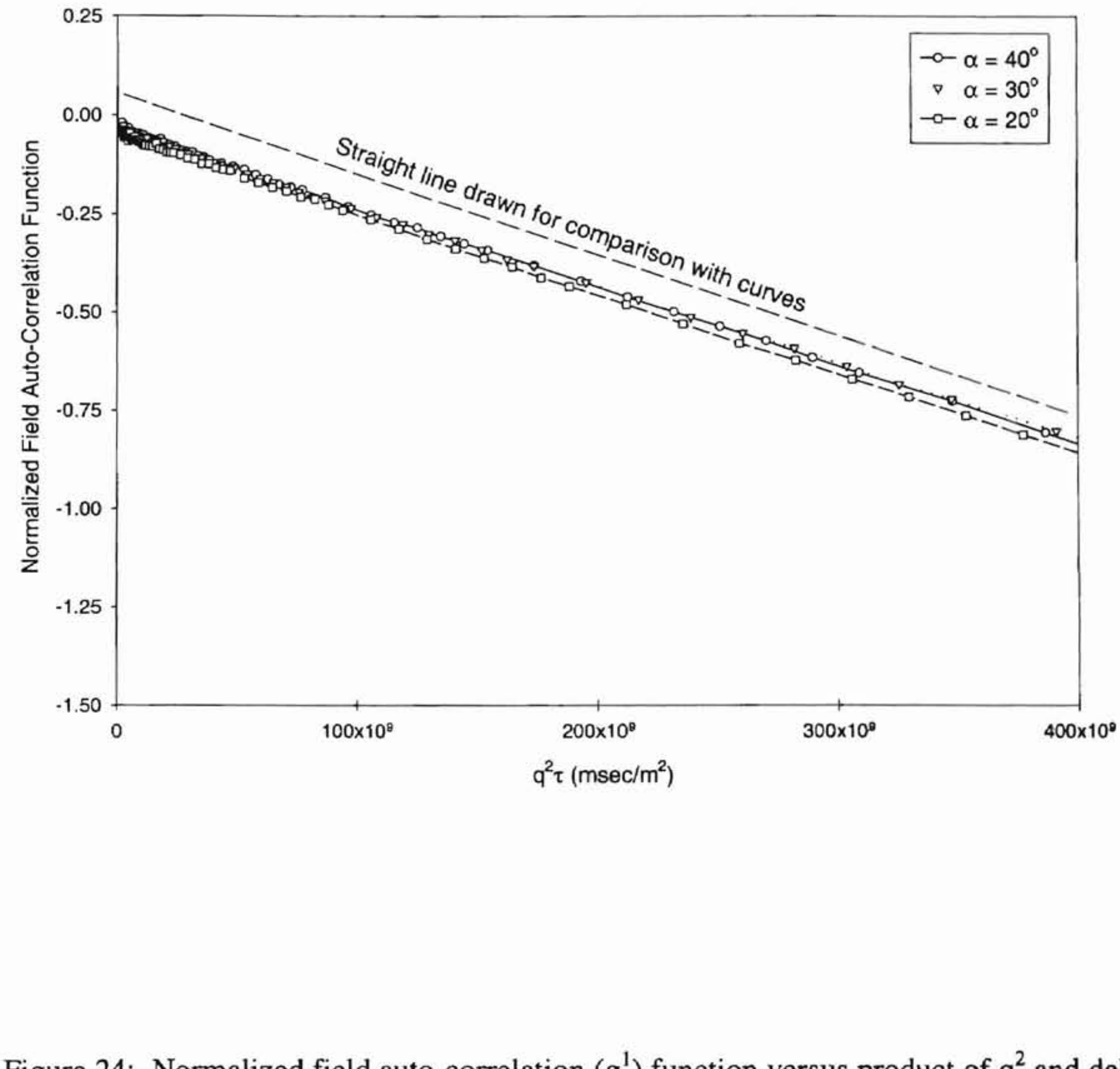

Figure 24: Normalized field auto-correlation (g^1) function versus product of q^2 and delay time for 0.204 μm particles for the flowing case. The suspension is very dilute. Channel 1 is used for data collection. Three equal angles (α) of laser and detector arms are compared, viz., 40°, 30°, and 20°. Corresponding scattering angles are 122°, 136°, and 150°, respectively. Data corresponds to experiment 61.

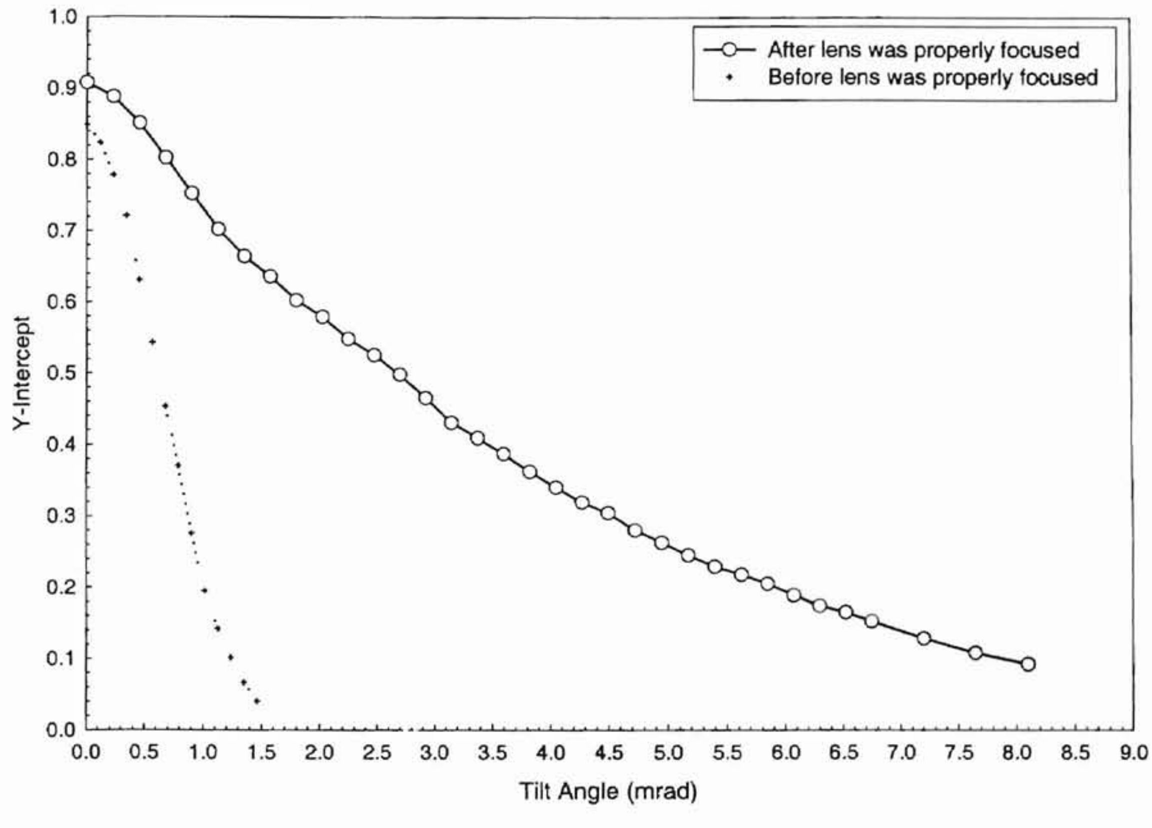

Figure 25: Y-intercept versus tilt angle mapping for 0.107 μm particles for the flowing case. The two curves correspond to the results obtained when the lens was not, and later, was focused properly along the direction of the laser beam. The volume fraction is 0.198 percent. The flow rate is 50 percent. The angle α is 40° (corresponding scattering angle is 122°). Data corresponds to experiments 91 and 97.

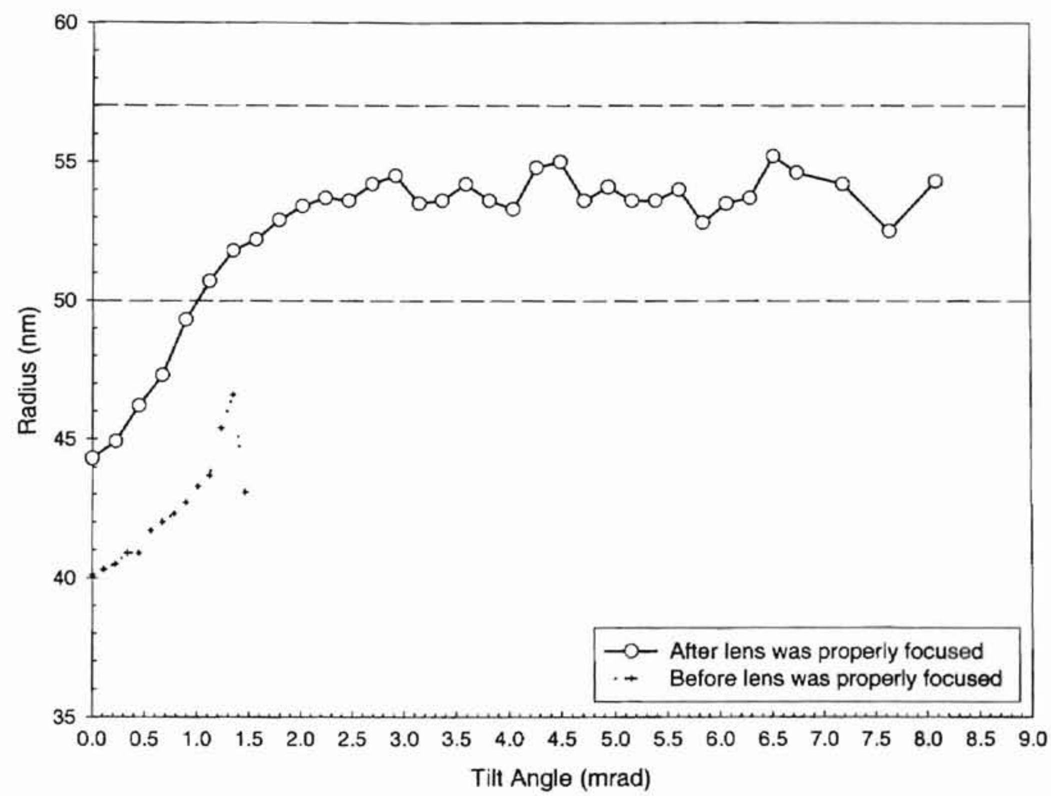

Figure 26: Radius versus tilt angle mapping corresponding to the data in Fig. 25. The dashed lines indicate the range of expected particle size as specified by the manufacturer of the particles.

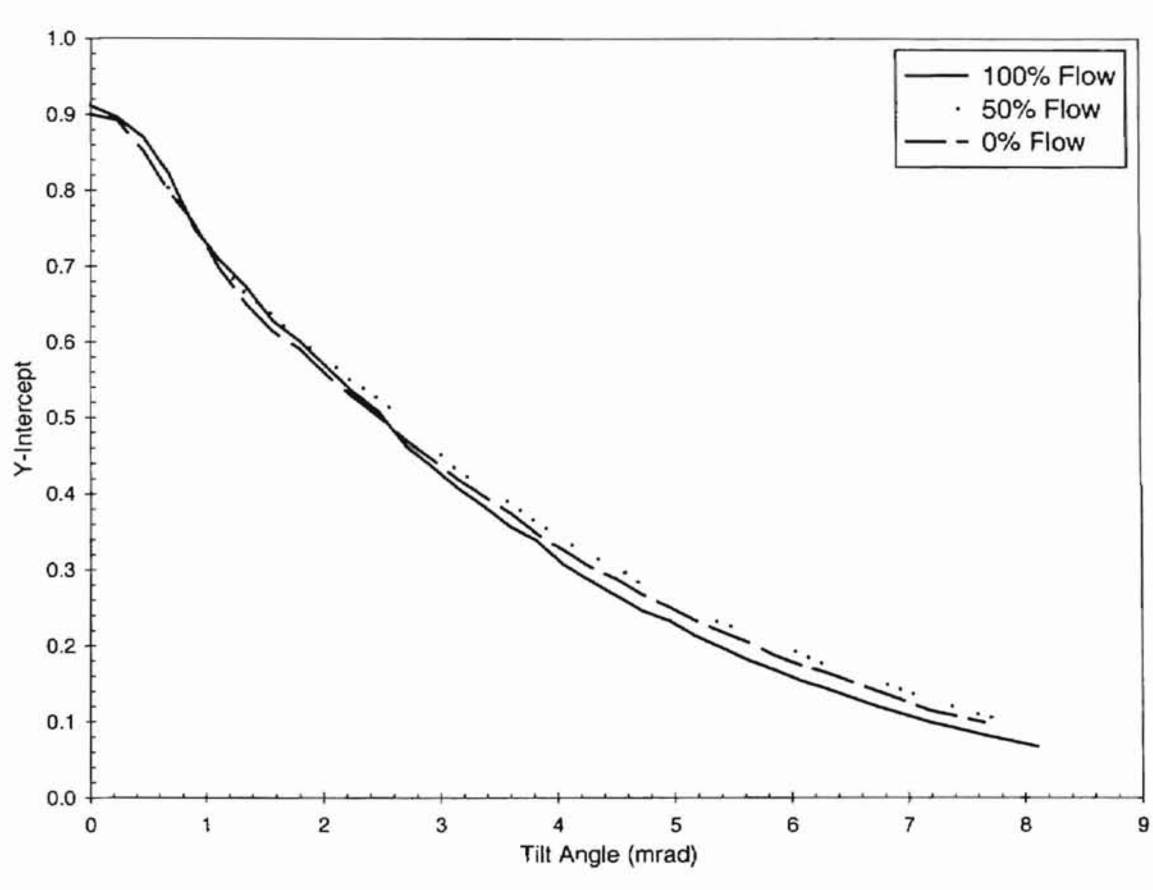

Figure 27: Y-intercept versus tilt angle mapping for 0.107 μm particles for the flowing case. The volume fraction is 0.198 percent. The angle α is 40° (corresponding scattering angle is 122°). Three different flow rates are compared here, viz., 0%, 50%, and 100% flow. Data corresponds to experiments 96, 97, and 98.

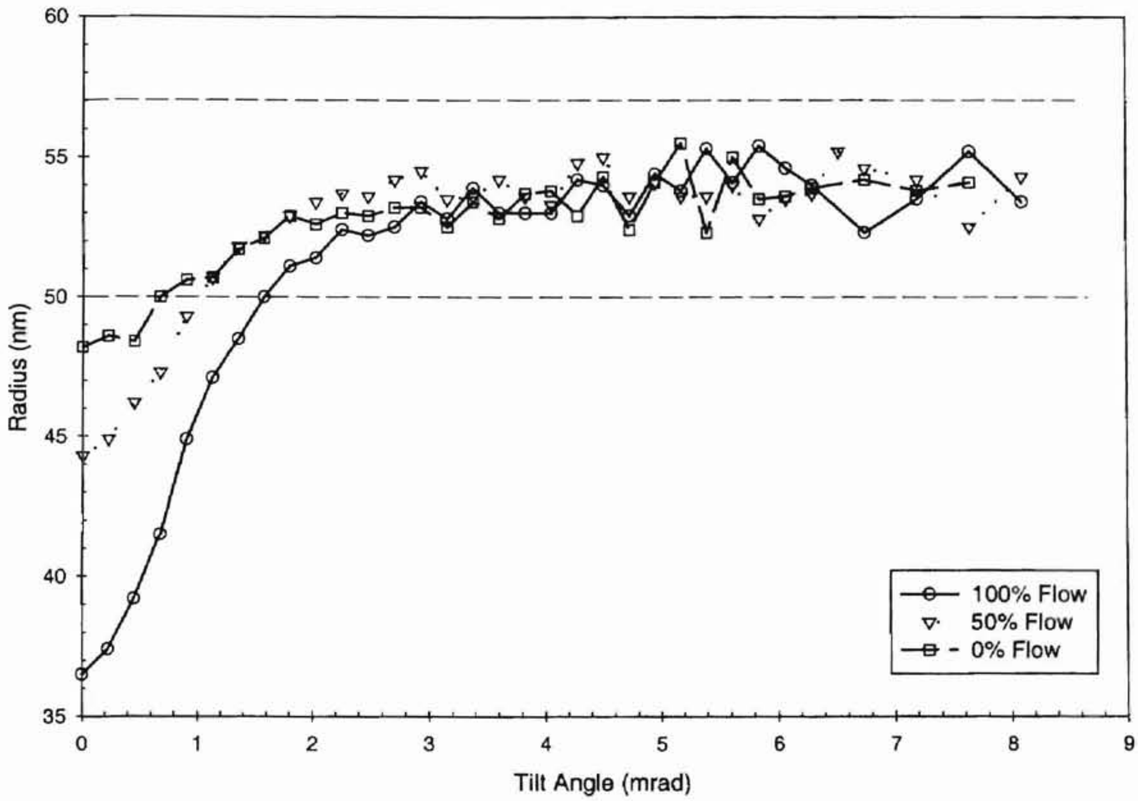

Figure 28: Radius versus tilt angle mapping for the data shown in Fig. 27. The dashed lines indicate the range of expected particle size as specified by the manufacturer of the particles.

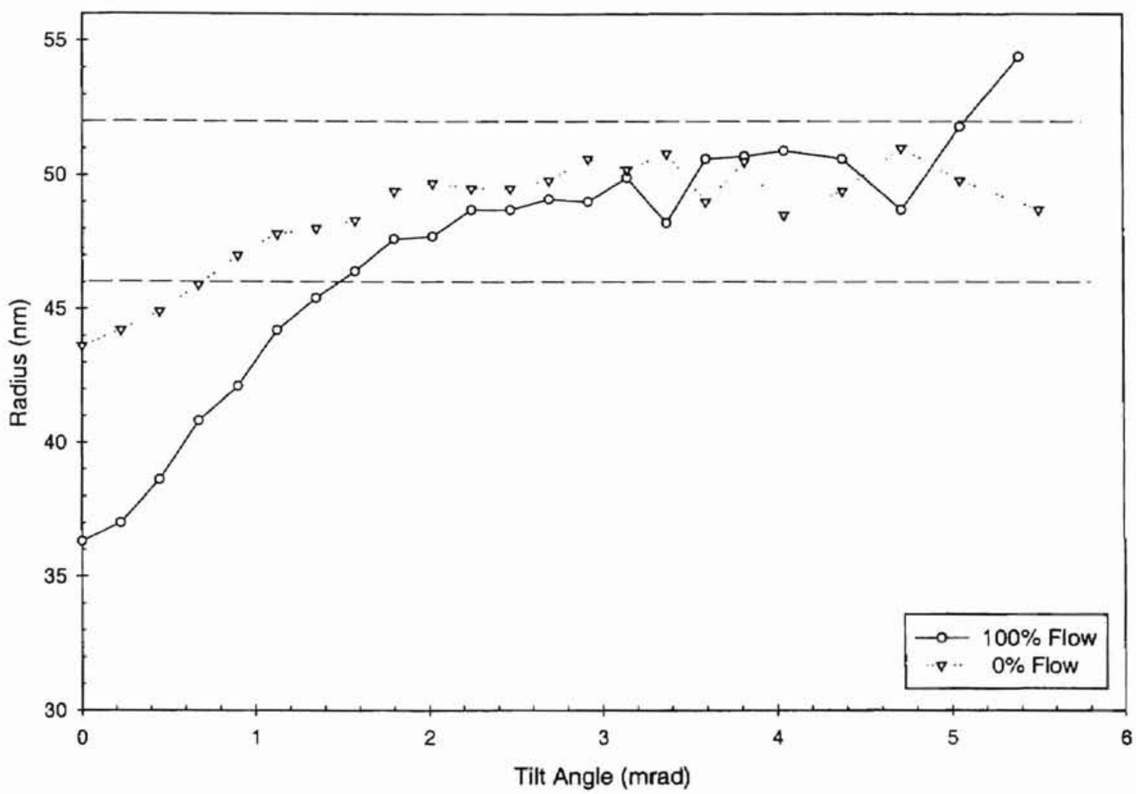

Figure 29: Radius versus tilt angle mapping for 0.098 μm particles for the flowing case. The volume fraction is 0.86 percent. The angle α is 30^o (corresponding scattering angle is 136^o). Two different flow rates are compared here, viz., 0% and 100% flow. The dashed lines indicate the range of expected particle size as specified by the manufacturer of the particles. Data corresponds to experiments 108 and 109.

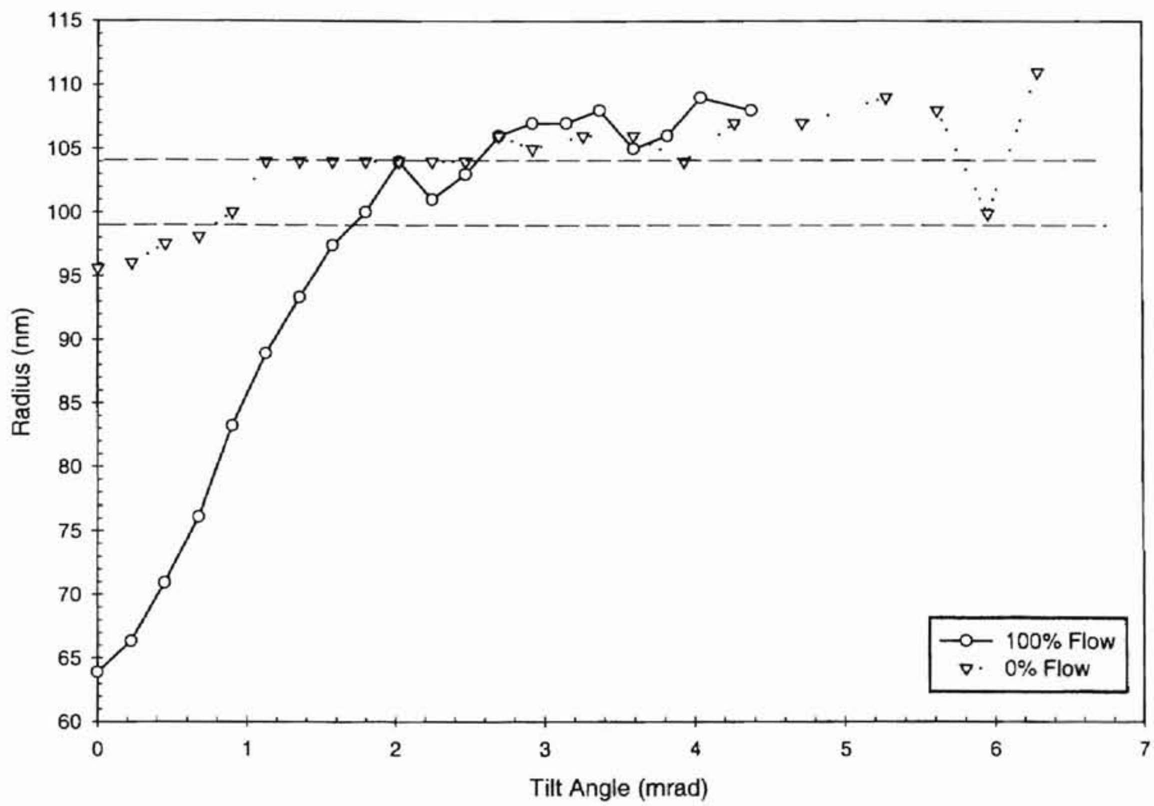

Figure 30: Radius versus tilt angle mapping for 0.203 μm particles for the flowing case. The volume fraction is 0.20 percent. The angle α is 30° (corresponding scattering angle is 136°). Two different flow rates are compared here, viz., 0% and 100% flow. The dashed lines indicate the range of expected particle size as specified by the manufacturer of the particles. Data corresponds to experiments 113 and 114.

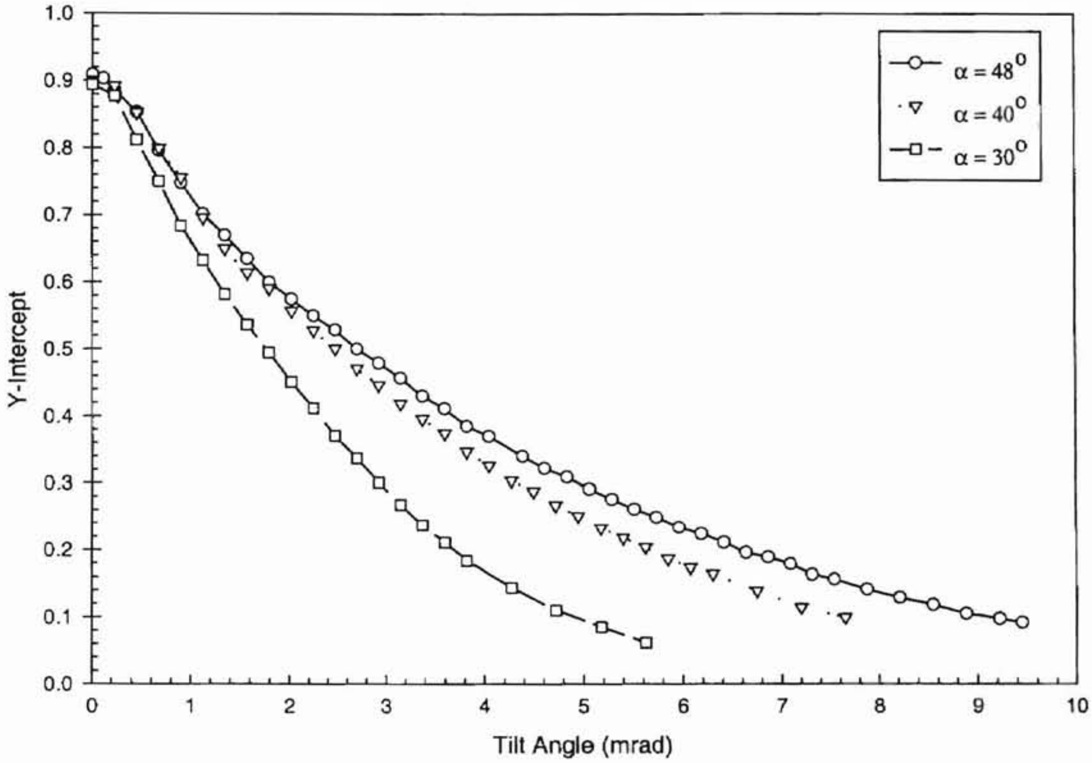

Figure 31: Y-intercept versus tilt angle mapping for 0.107 μm particles for the non-flowing case. The volume fraction is 0.198 percent. Three different α angles are compared here, viz., 48°, 40°, and 30° (corresponding scattering angles are 112°, 122°, and 135°). Data corresponds to experiments 93, 96, and 99.

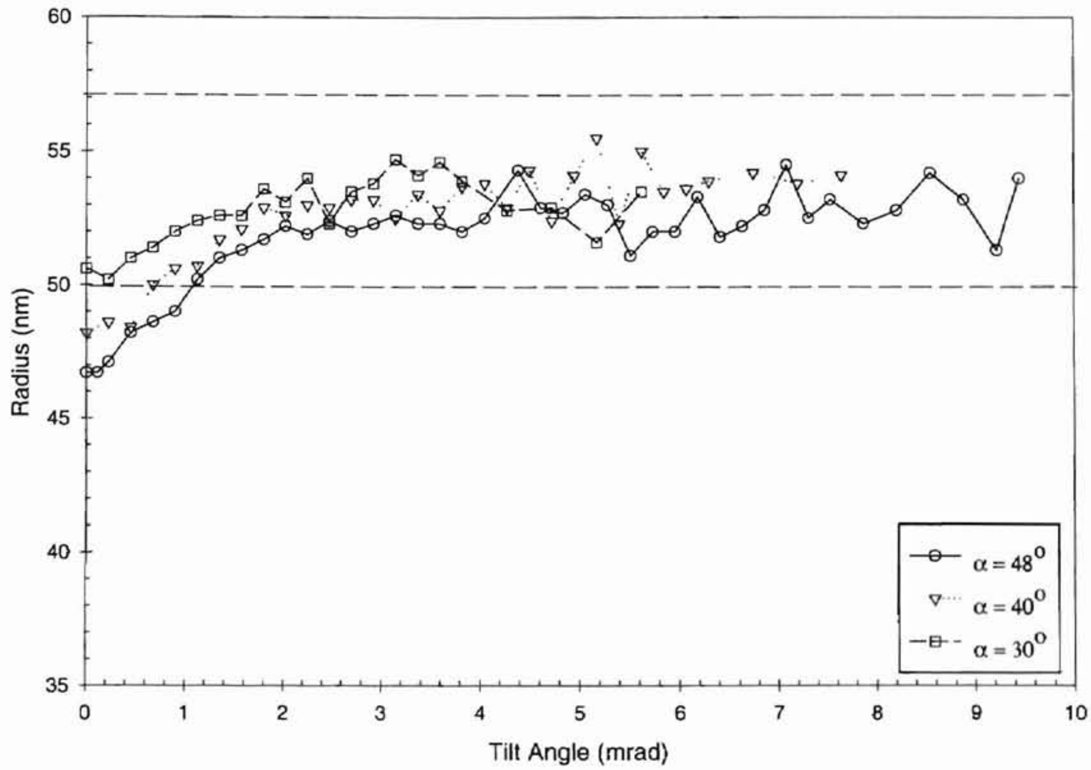

Figure 32: Radius versus tilt angle mapping for the data shown in Fig. 31. The dashed lines indicate the range of expected particle size as specified by the manufacturer of the particles.

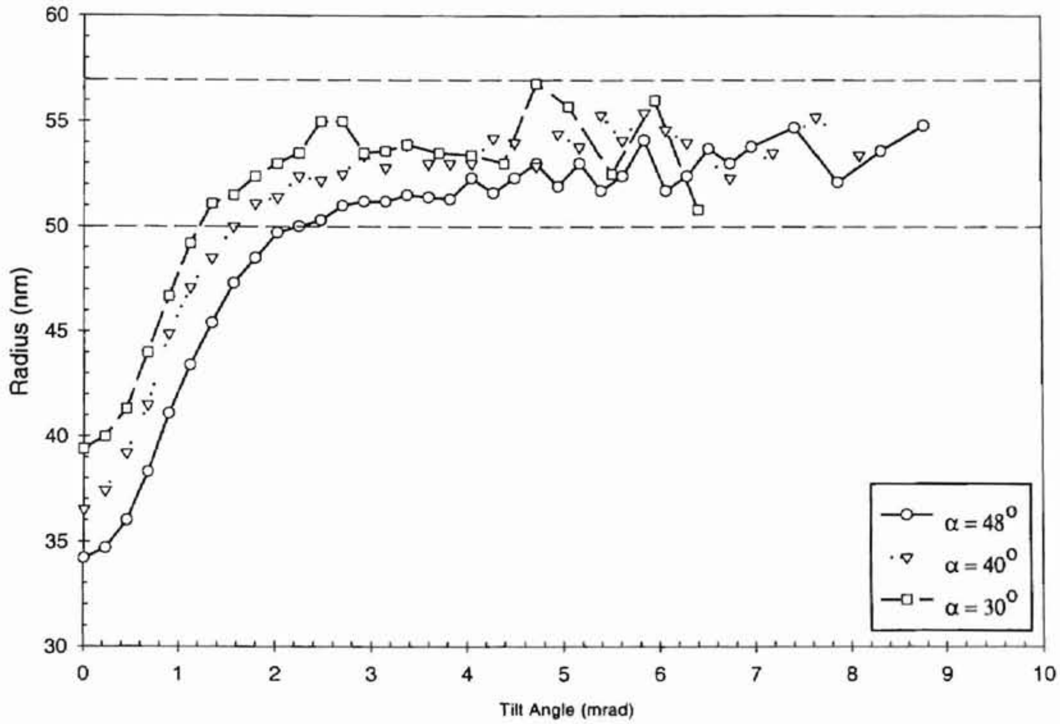

Figure 33: Radius versus tilt angle mapping for 0.107 μm particles for the flowing case. The volume fraction is 0.198 percent. The flow rate is 100 percent. Three different α angles are compared here, viz., 48°, 40°, and 30° (corresponding scattering angles are 112°, 122°, and 135°). The dashed lines indicate the range of expected particle size as specified by the manufacturer of the particles. Data corresponds to experiments 95, 98, and 101.

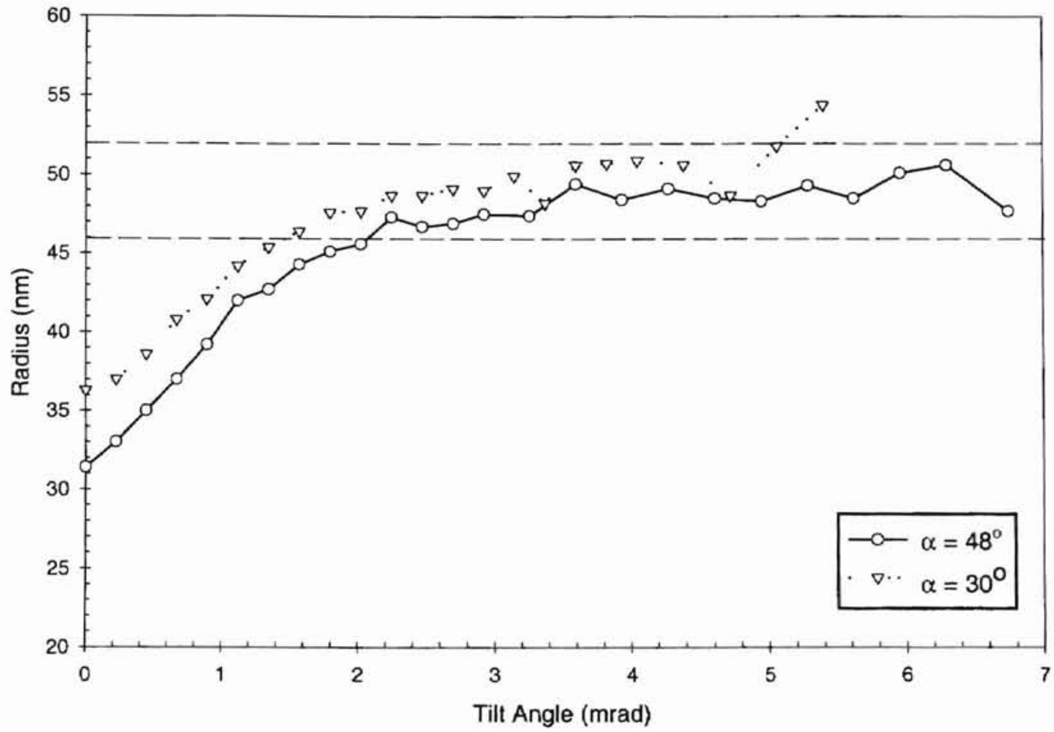

Figure 34: Radius versus tilt angle mapping for 0.098 μm particles for the flowing case. The volume fraction is 0.86 percent. The flow rate is 100 percent. Two different α angles are compared here, viz., 48° and 30° (corresponding scattering angles are 112° and 135°). The dashed lines indicate the range of expected particle size as specified by the manufacturer of the particles. Data corresponds to experiments 106 and 109.

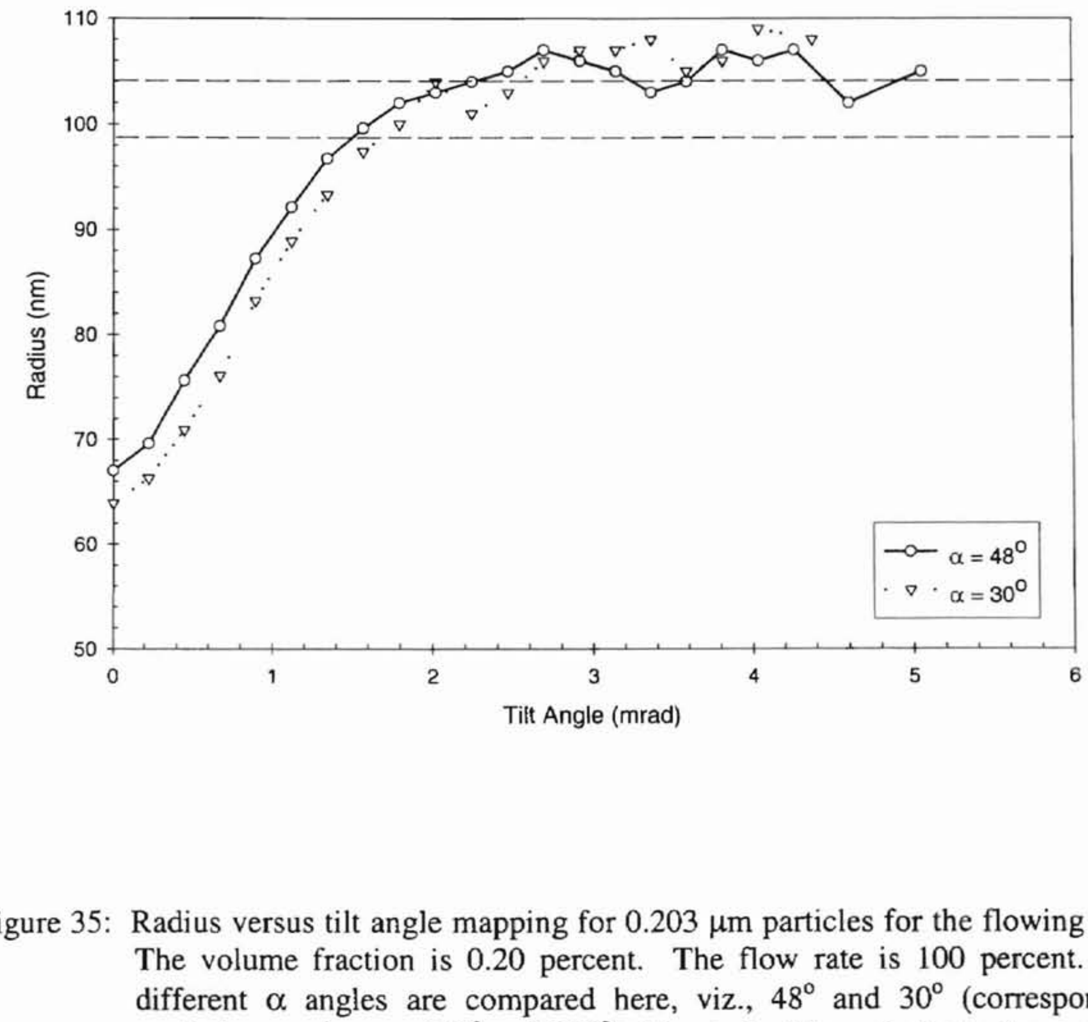

Figure 35: Radius versus tilt angle mapping for 0.203 μm particles for the flowing case. The volume fraction is 0.20 percent. The flow rate is 100 percent. Two different α angles are compared here, viz., 48° and 30° (corresponding scattering angles are 112° and 135°). The dashed lines indicate the range of expected particle size as specified by the manufacturer of the particles. Data corresponds to experiments 112 and 114.

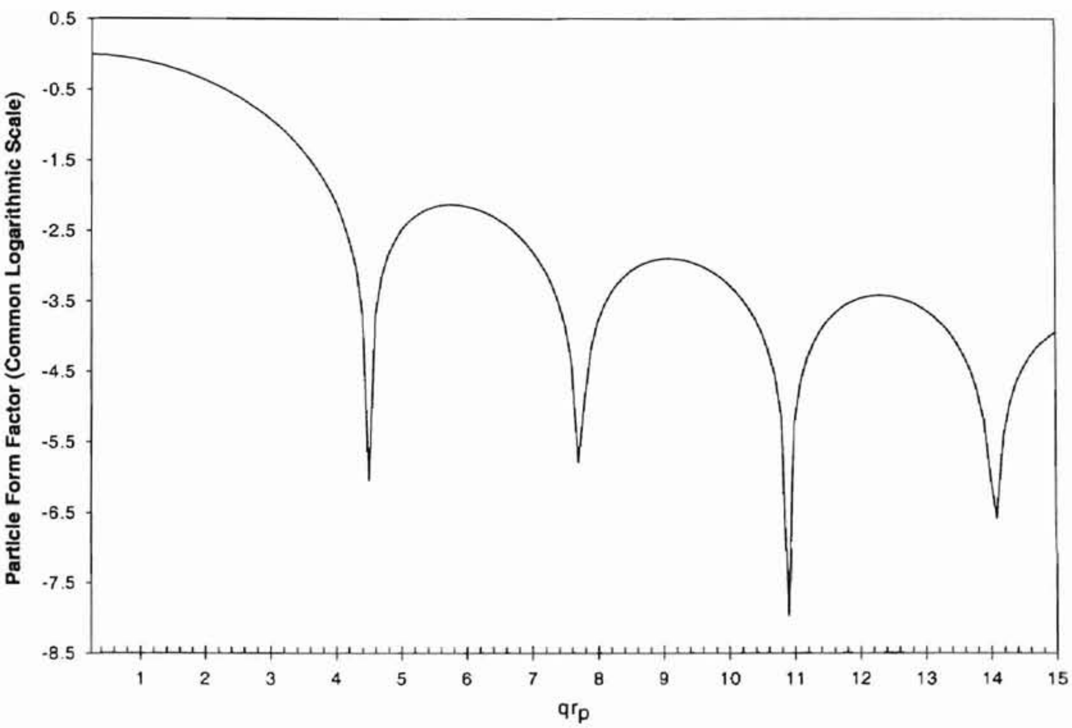

Figure 36: Plot of the Rayleigh-Gans particle form factor $P(qr_p)$ (on a common logarithmic scale) as a function of qr_p, where q is the magnitude of the scattering wave vector, and r_p is the radius of the particle.

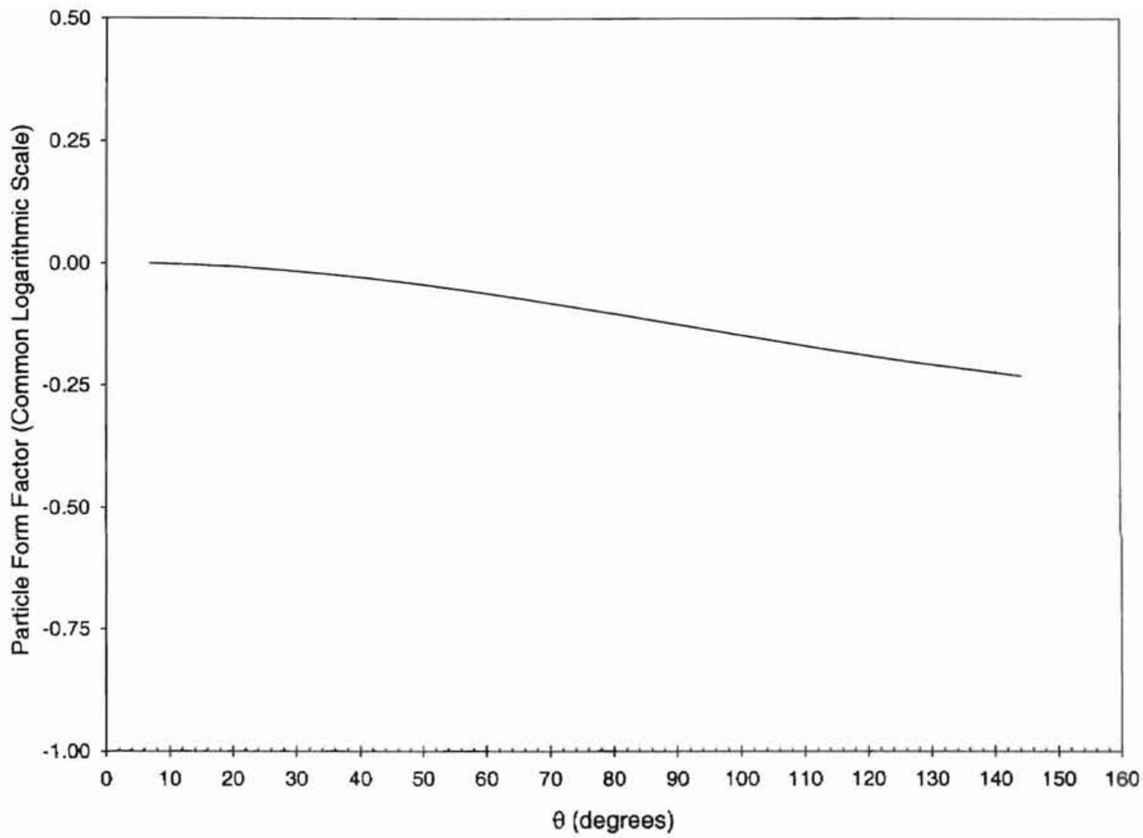

Figure 37: Plot of the Rayleigh-Gans particle form factor $P(qr_p)$ (on a common logarithmic scale) as a function of scattering angle θ, for 0.107 μm particles.

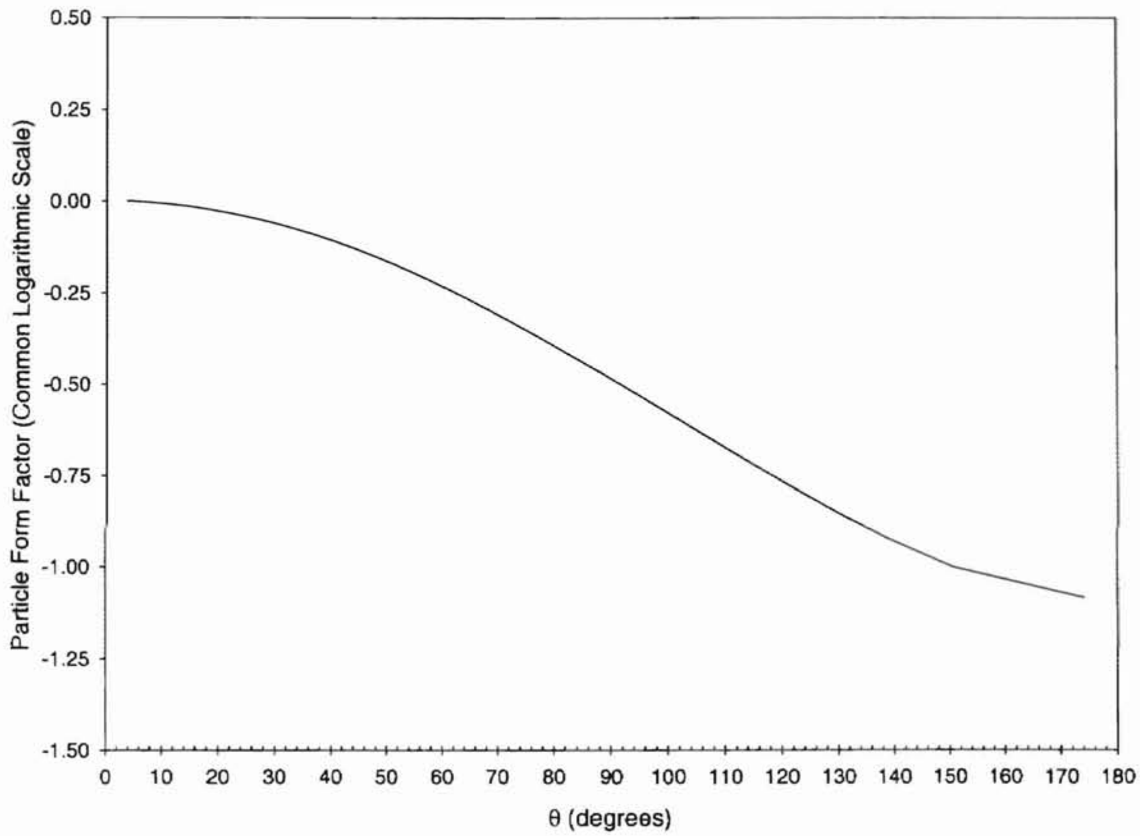

Figure 38: Plot of the Rayleigh-Gans particle form factor $P(qr_p)$ (on a common logarithmic scale) as a function of scattering angle θ, for 0.204 μm particles.

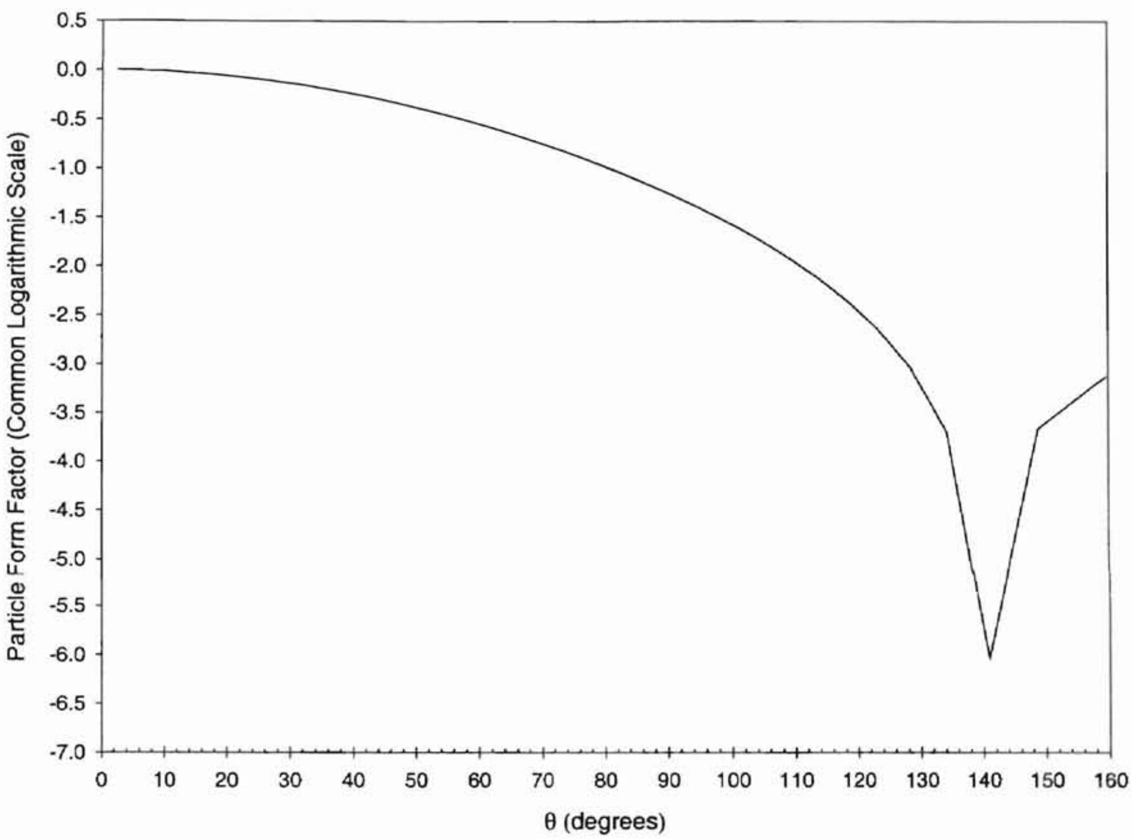

Figure 39: Plot of the Rayleigh-Gans particle form factor $P(qr_p)$ (on a common logarithmic scale) as a function of scattering angle θ, for 0.304 μm particles.

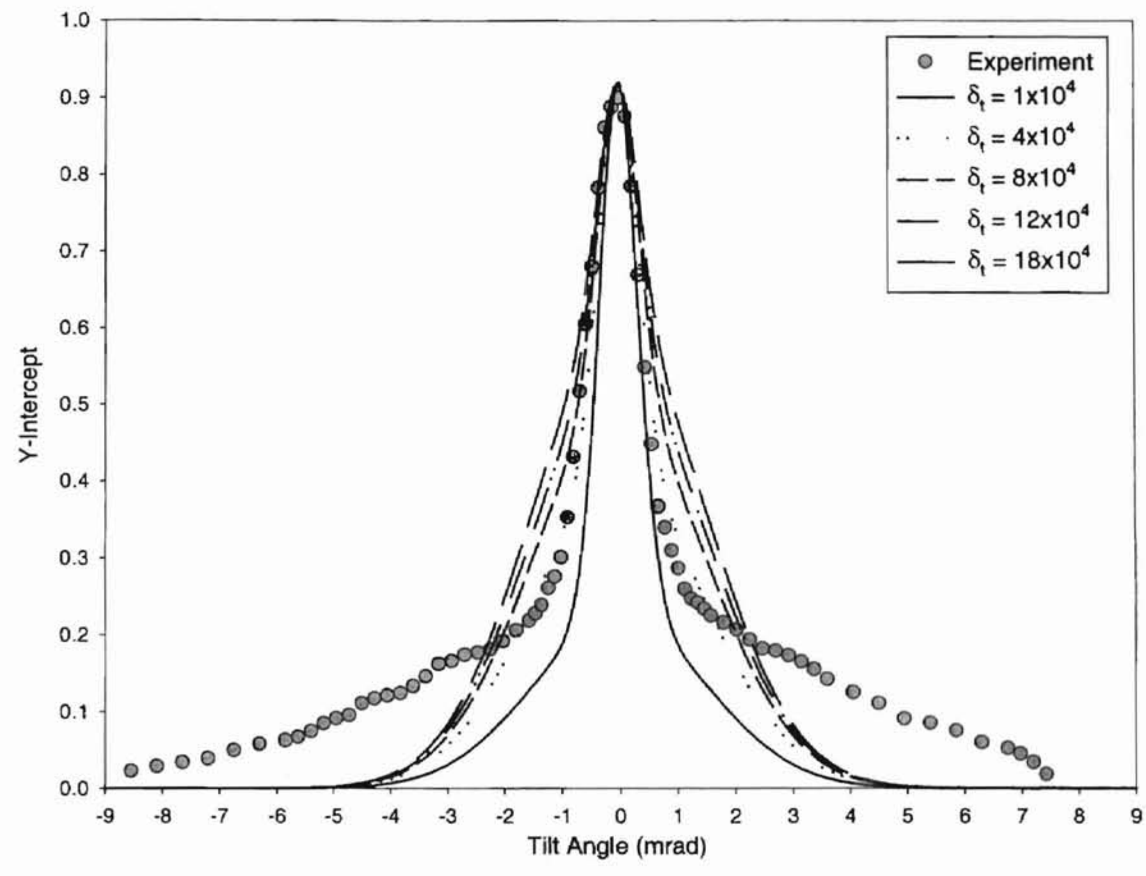

Figure 40: Plot of the Y-intercept obtained from experimental data and the theoretically predicted value of S/N ratio [Nobbmann *et al.* (1997)] versus tilt angle. Plot shows the effect of variation of the parameter δ_t. The experimental data corresponds to the non-flowing case, square cell geometry, volume fraction of 0.32 percent, and a scattering angle of 90°. The values of the theoretical parameters are: $\alpha_t = 6.1\text{x}10^6/\text{m}^2$, $\beta_t = 4\text{x}10^8/\text{m}^2$, and A:B = 1:770.

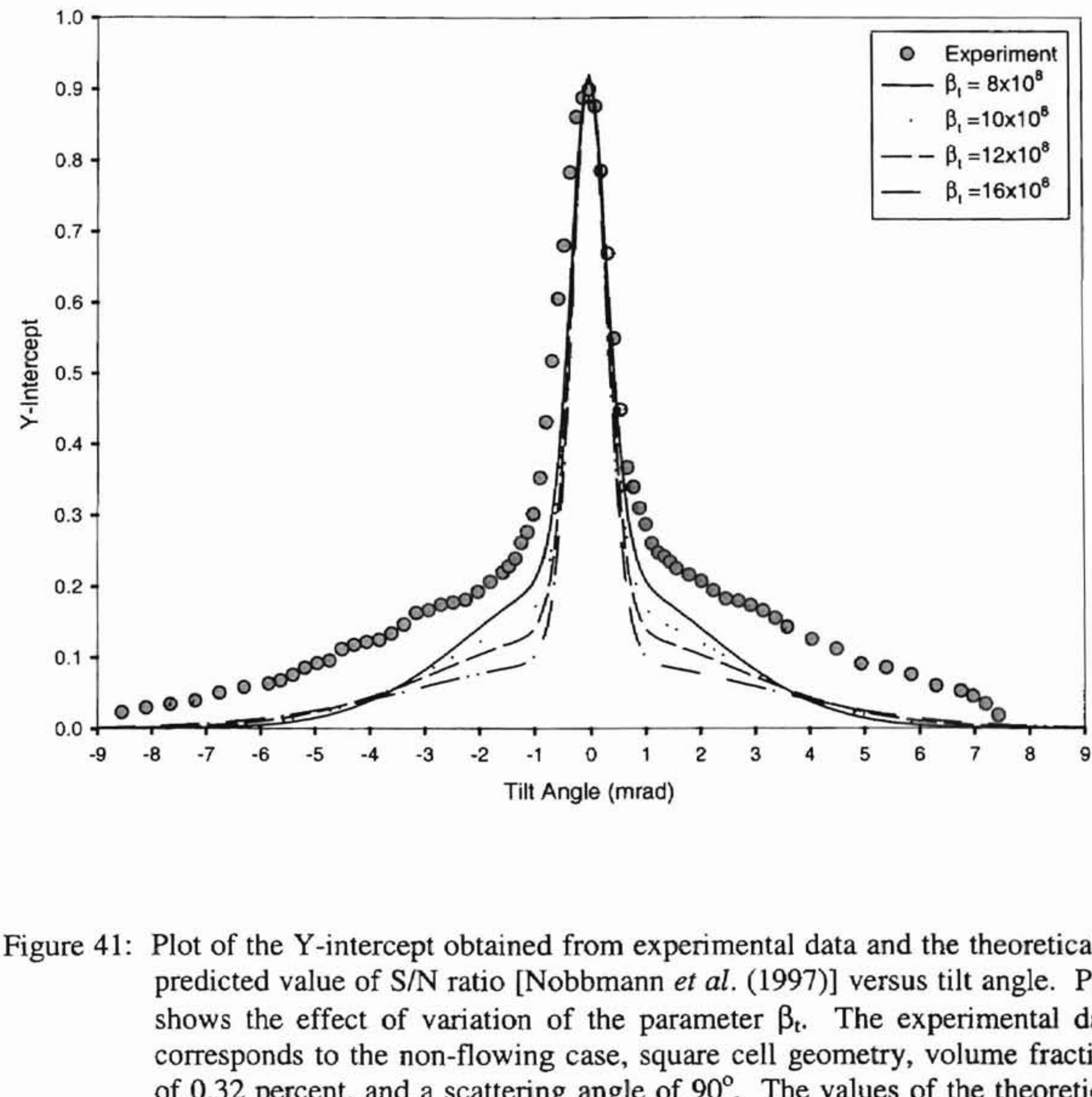

Figure 41: Plot of the Y-intercept obtained from experimental data and the theoretically predicted value of S/N ratio [Nobbmann *et al.* (1997)] versus tilt angle. Plot shows the effect of variation of the parameter β_t. The experimental data corresponds to the non-flowing case, square cell geometry, volume fraction of 0.32 percent, and a scattering angle of 90°. The values of the theoretical parameters are: $\alpha_t = 6.1x10^6 /m^2$, $\delta_t = 4x10^4 /m^2$, and A:B = 1:770.

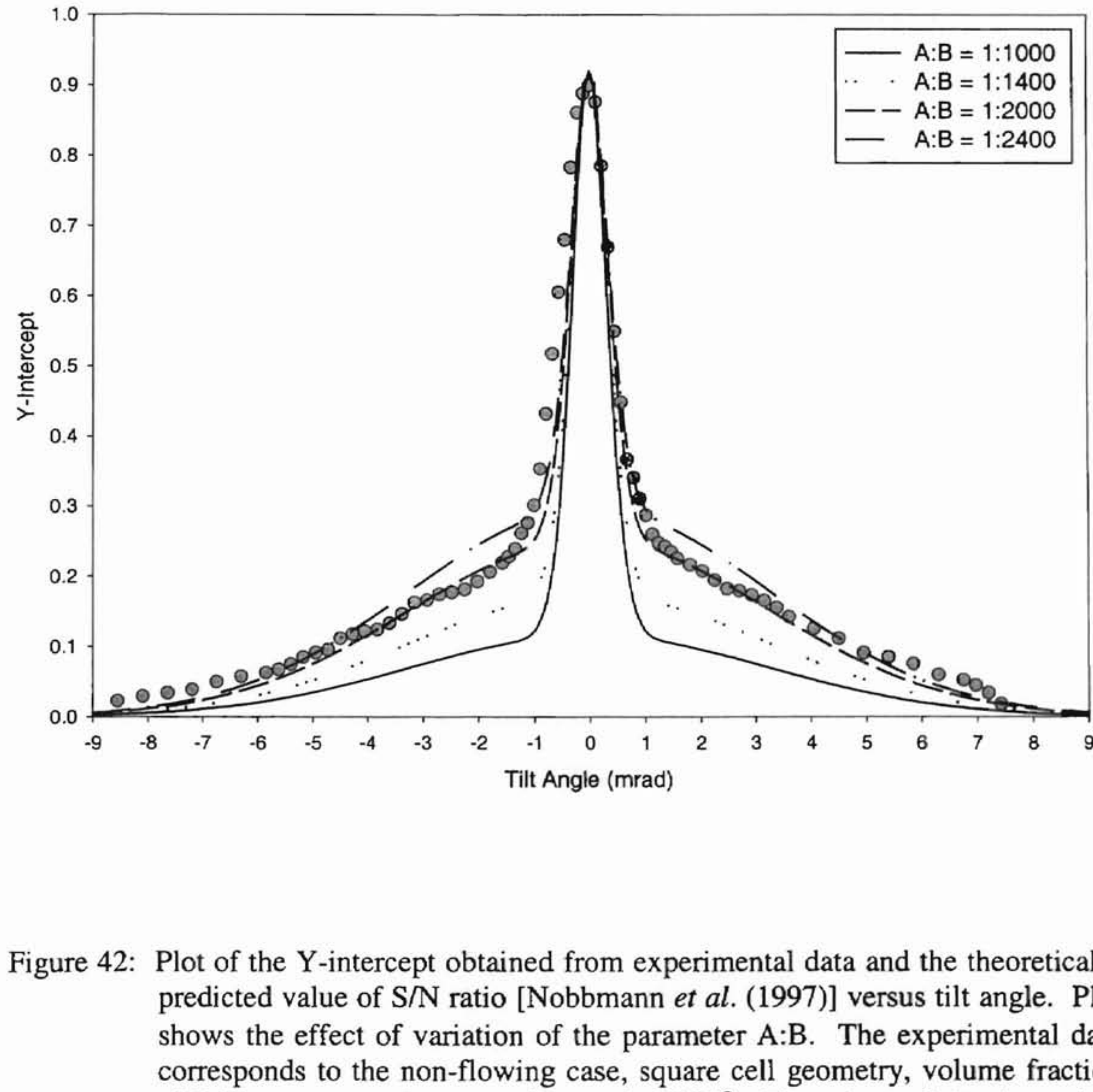

Figure 42: Plot of the Y-intercept obtained from experimental data and the theoretically predicted value of S/N ratio [Nobbmann *et al.* (1997)] versus tilt angle. Plot shows the effect of variation of the parameter A:B. The experimental data corresponds to the non-flowing case, square cell geometry, volume fraction of 0.32 percent, and a scattering angle of 90°. The values of the theoretical parameters are: $\alpha_t = 6.1x10^6\,/m^2$, $\beta_t = 18x10^8\,/m^2$, and $\delta_t = 4x10^4\,/m^2$.

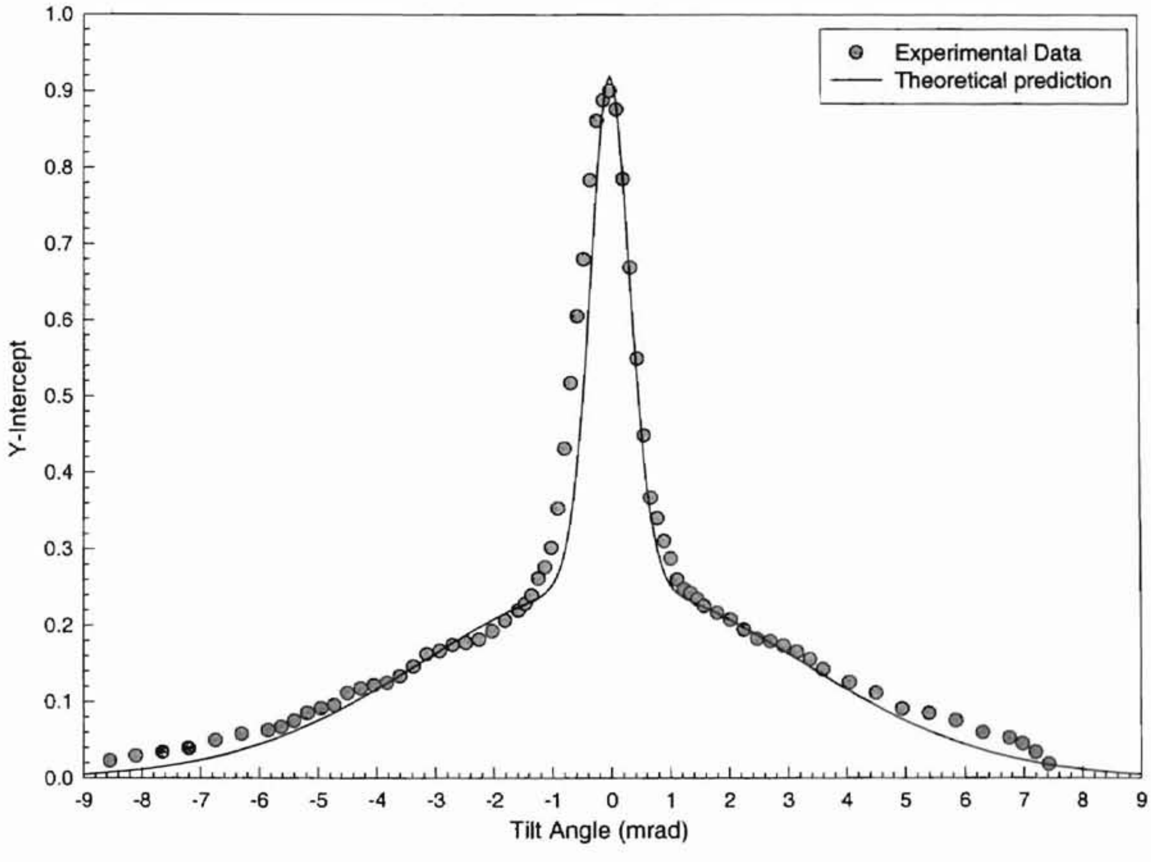

Figure 43: Plot of the Y-intercept obtained from experimental data and the theoretically predicted value of S/N ratio [Nobbmann *et al.* (1997)] versus tilt angle. The experimental data corresponds to the non-flowing case, square cell geometry, volume fraction of 0.32 percent, and a scattering angle of 90^o. The values of the parameters used for the fit are: $\alpha_t = 6.1x10^6 /m^2$, $\beta_t = 18x10^8 /m^2$, $\delta_t = 4x10^4 /m^2$, and A:B = 1:2000.

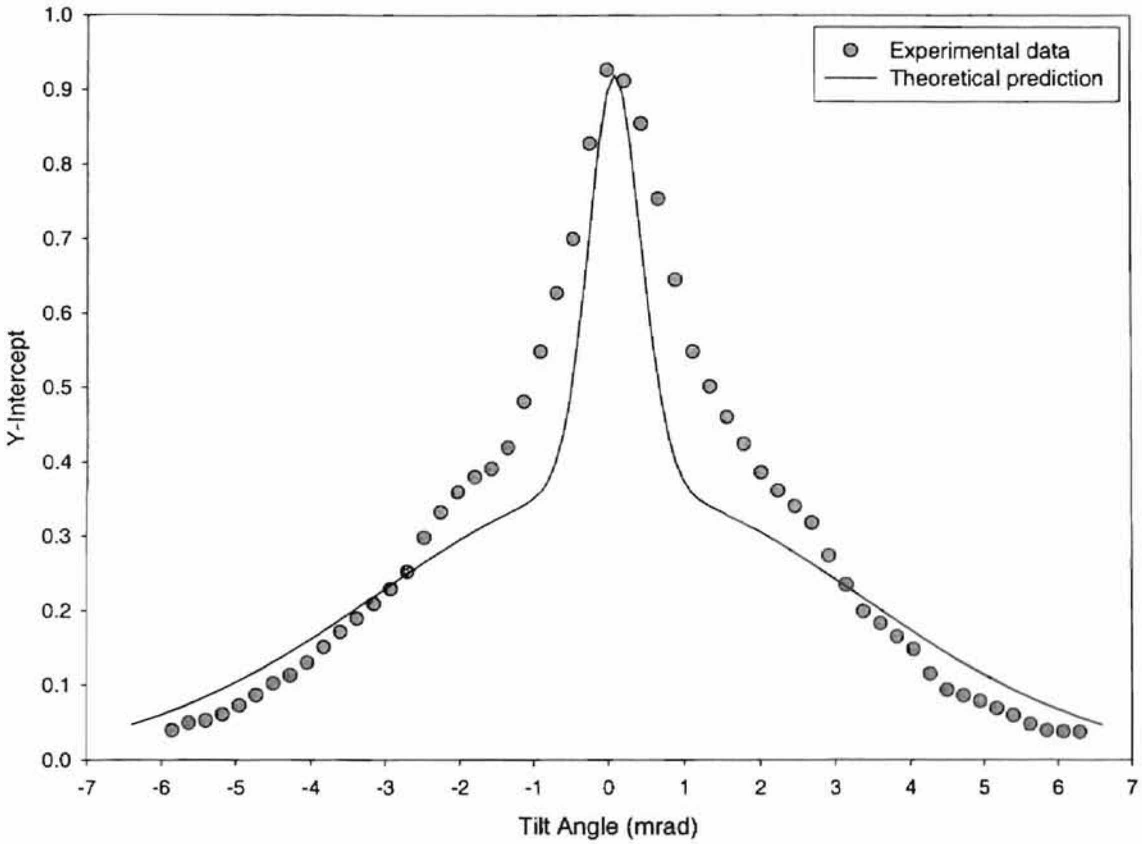

Figure 44: Plot of the Y-intercept obtained from experimental data and the theoretically predicted value of S/N ratio [Nobbmann *et al.* (1997)] versus tilt angle. The experimental data corresponds to the non-flowing case, square cell geometry, volume fraction of 0.15 percent, and a scattering angle of 90°. The values of the parameters used for the fit are: $\alpha_t = 6.1 \times 10^6$ /m^2, $\beta_t = 18 \times 10^8$ /m^2, $\delta_t = 4 \times 10^4$ /m^2, and A:B = 1:3100.

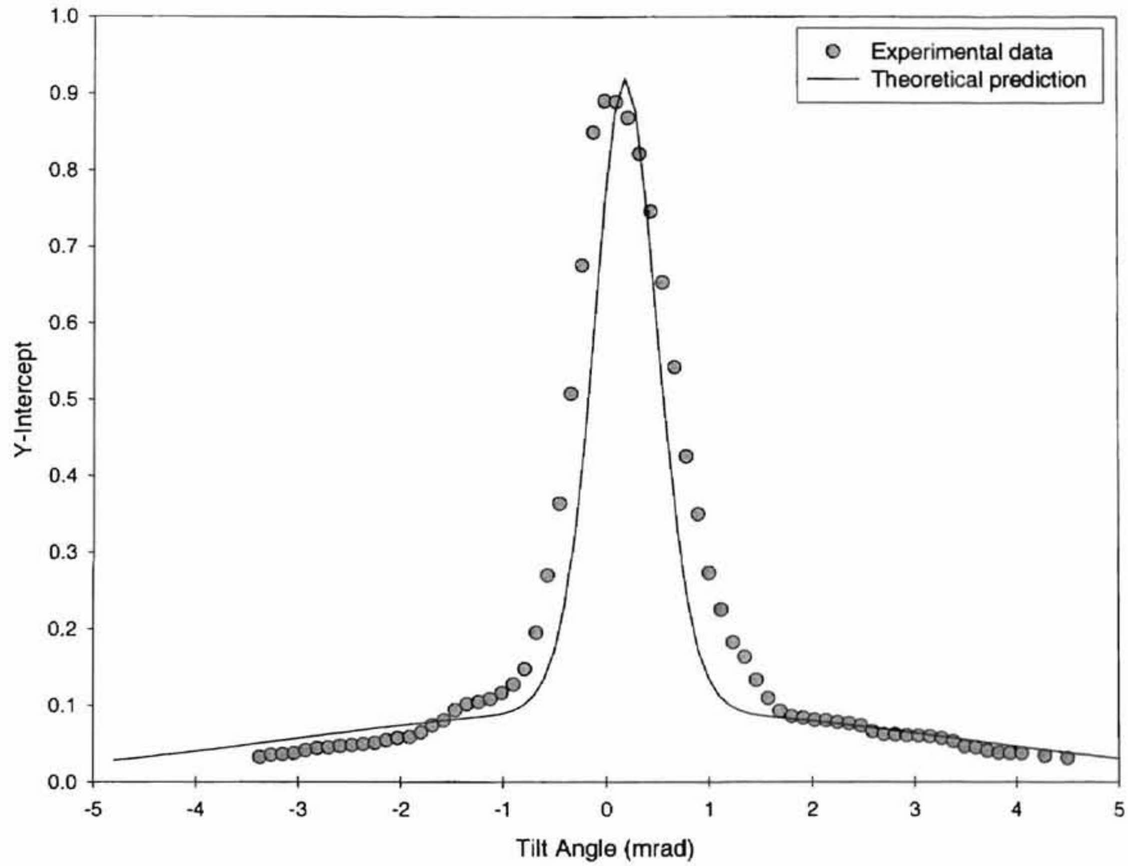

Figure 45: Plot of the Y-intercept obtained from experimental data and the theoretically predicted value of S/N ratio [Nobbmann *et al.* (1997)] versus tilt angle. The experimental data corresponds to the non-flowing case, square cell geometry, volume fraction of 0.43 percent, and a scattering angle of 90°. The values of the parameters used for the fit are: $\alpha_t = 6.1 \times 10^6\ /m^2$, $\beta_t = 18 \times 10^8\ /m^2$, $\delta_t = 4 \times 10^4\ /m^2$, and A:B = 1:850.

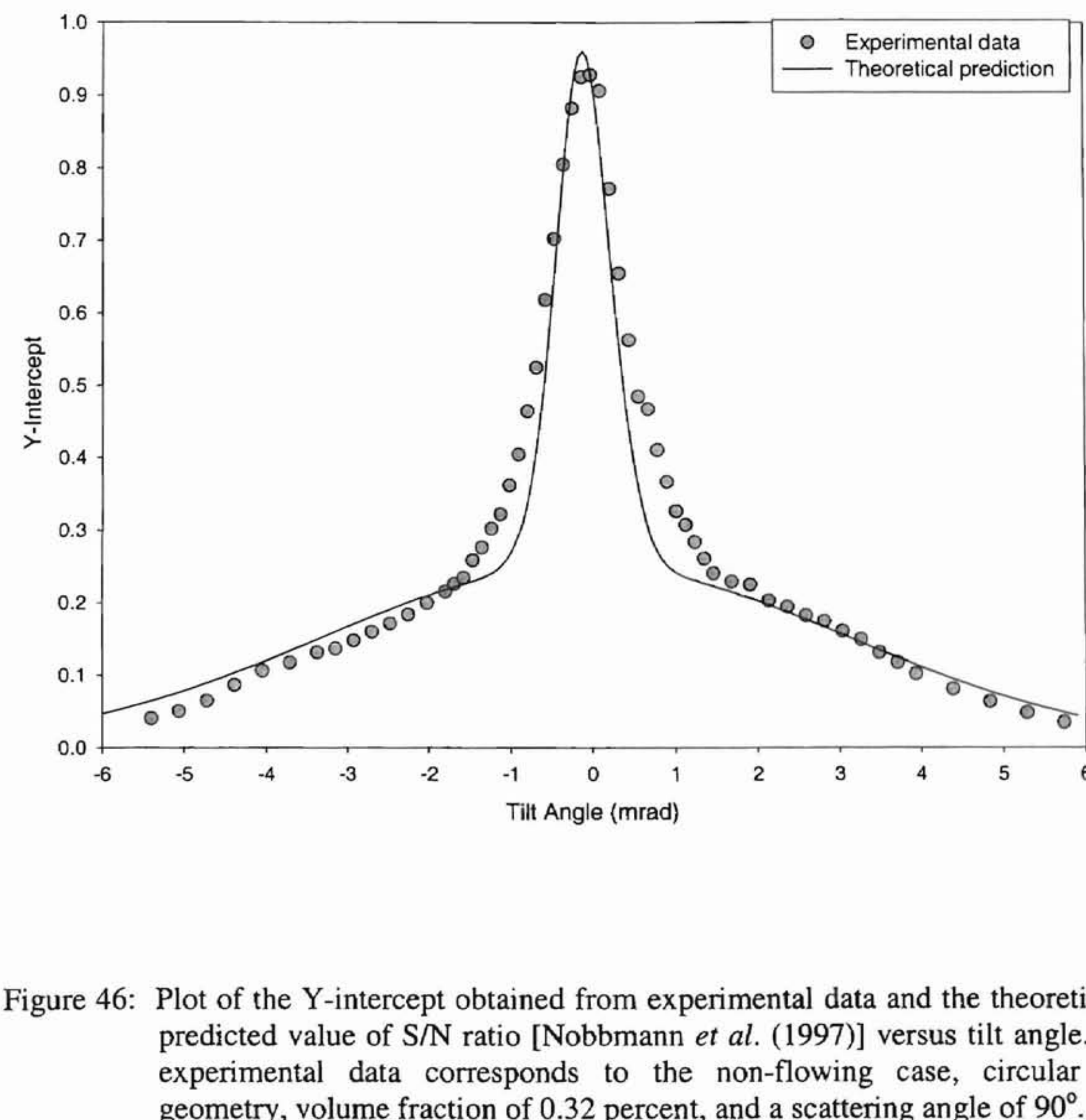

Figure 46: Plot of the Y-intercept obtained from experimental data and the theoretically predicted value of S/N ratio [Nobbmann *et al.* (1997)] versus tilt angle. The experimental data corresponds to the non-flowing case, circular cell geometry, volume fraction of 0.32 percent, and a scattering angle of 90°. The values of the parameters used for the fit are: $\alpha_t = 6.1\times10^6$ /m^2, $\beta_t = 18\times10^8$ /m^2, $\delta_t = 4\times10^4$ /m^2, and A:B = 1:1900.

CHAPTER VII

CONCLUSIONS AND RECOMMENDATIONS

7.1 Conclusions

It is important to be able to determine the diameter of micron size particles in a wide variety of industrial applications. Industries producing, for example, pharmaceutical drugs, paints, and air/fuel filtering systems need to be able to determine and control the diameters of micron size particles. It is particularly desirable to make use of in-situ, non-destructive, non-intrusive testing techniques to size particles, so that particle sizing takes place without disturbing the manufacturing process. Non-in-situ testing techniques have procedural limitations that include a necessity to remove the sample from the process to investigate it in the laboratory, or to allow a sample taken from a flowing system to stagnate prior to analysis, or to dilute the sample.

In-situ, non-intrusive techniques ensure that there are no great differences between the analysis and the manufacturing environments, which bring into question the validity of non-in-situ testing techniques. Dynamic Light Scattering (DLS) is one form of in-situ, non-destructive, non-intrusive technique that makes use of light scattered by particles to determine particle characteristics. Some limitations involving particle characterization in dense systems, because of multiple scattering effects were outlined in Chapter III. A technique of multiple scattering suppression using a one-beam, two-detector, cross-correlation setup was proposed by Meyer *et al.* (1997). This technique was verified by Nobbmann *et al.* (1997). This research furthered the work done by Nobbmann *et al.* on multiple scattering suppression.

The objectives of this research were two-fold. The first objective of this research was to further the work done by Nobbmann *et al.* (1997) on multiple scattering suppression in non-flowing suspensions by studying the effects of particle sizes, volume fractions, scattering angles, and sample cell cross-sections. This was done to gain experience in the technique of multiple scattering suppression. The second objective of this research was to extend the technique of multiple scattering suspension to flowing fluids. Part of the first objective of this research was to verify the accuracy of the theoretical prediction of the signal-to-noise ratio by Nobbmann *et al.* (1997).

Toward fulfillment of the first objective, experiments were conducted on non-flowing suspensions of polystyrene latex particles at different concentrations. From the preliminary experiments, some important characteristics of the experimental setup like the criticality of proper lens alignment and detector position were observed. These characteristics were very critical to the success of the experiments and are described in detail in Chapter VI. These characteristics were incorporated into formulation of the alignment and experimental procedures for the non-flowing, and later, for the flowing experiments. From the experiments conducted at different volume fractions (0.15 %, 0.32 %, and 0.43 %), it was observed that, with increasing concentration, the peak of the Y-intercept curve narrowed and the shoulders dropped. The radius predicted was also lower. This was due to the increase in multiple scattering at higher concentrations. A greater tilt of separation angle (2 mrad for 0.43 % compared to 1 mrad for 0.15 % volume fraction) between the detectors was required before multiple scattering ceased to be correlated, and the radius was predicted correctly. Thus the one-beam, two-detector, cross-correlation technique was found to be effective in suppressing multiple scattering effects over a range of volume fractions (0.15 %-0.45 %).

Toward fulfillment of the second objective, an experimental setup for the flowing case was designed, making use of the characteristics of the non-flowing setup already observed. Care was also taken that the setup maintained the flow geometry (the angular bisector between the incident and the detected beams should be normal to the flow vector) required for the suppression of flow effects. The first set of experiments was performed to verify the effectiveness of the technique in suppressing flow effects, by experimenting with dilute, flowing suspensions. The effects of flow were suppressed at different flow velocities (0 - 7.78 mm/s), as was ascertained through the g^1 function. Experiments were later conducted to extend multiple scattering suppression in flowing fluids.

Experiments were conducted to study the effects of two parameters, viz., velocity and scattering angle. It was observed that as velocity increased (0 to 7.78 mm/s), the radius predicted was lower (about 10 nm for 0.107 μm particles), and it required a greater tilt angle of separation (about 1 mrad) between the detectors, before the radius was predicted correctly. This effect is similar to the effect of increase in multiple scattering, and so it could be concluded that the effect of the increase in velocity was analogous to the effect of increase in multiple scattering. With a decrease in the angle (α) of laser and detector arms from 48° to 30 ° (an increase in the scattering angle θ from 112° to 136°), the radius predicted was higher (about 5 nm at 100 % flow) in the peak region of the Y-intercept curve. Less tilt angle separation (1 mrad instead of 2 mrad) was required, before the radius was predicted correctly. This is a characteristic of decreasing multiple scattering, and was because of the area of intersection between the laser and detector beams being closer to the test cell wall at lower angles ($\alpha = 30^o$), where less multiple scattering is likely. The effects of other parameters such as volume fraction, particle size are discussed in detail by Cambern (1999). With increasing volume fraction (0.32 % to 0.86 %), the radius predicted when the two detectors are not spatially separated decreases by about 5 nm.

The theoretical prediction of the S/N ratio with the equation (Eq. 3-16) proposed by Nobbmann *et al.* (1997) was verified by comparing the theoretical Y-intercept with the experimental value. The general trend was predicted well by the theory over a range of volume fractions (0.15 % to 0.43 %). The effect of some parameters (α_t, β_t, δ_t, and A:B) in the equation was studied, and the actual behavior agreed well with the expected behavior of the S/N ratio when each parameter was independently varied. An interesting observation made was that when α_t, β_t, and ϕ were fixed, varying the terms B and δ_t yielded the same value of S/N ratio as long as $B\sqrt{\delta_t}$ was a constant.

The theory of multiple scattering suppression works very well, when used in conjunction with flow suppression, to predict particle sizes in dense, flowing suspensions. It was not possible to study suspensions of larger particles (0.3 μm diameter and larger) because of hydrodynamic settling. It was also not possible to study the effects of flow at scattering angles higher than 136° or lower than 112°, because of the limitations in travel of the laser and detector arms. However, considering the sensitive nature of the experiments, some improvements in the designs can be made, which should make particle-sizing experiments easier and more controllable. Some recommendations on how to further the work done in this thesis will be presented in the following section.

7.2 Recommendations

There is a lot of opportunity for improving the design of the current setup in order to enable more accurate control of the components involved. One design improvement will be to have micrometers for controlling the motion/alignment of the back fiber in the detector housing (see Fig. 11). The current arrangement of set-screws did not allow recording the current position of the back fiber, and therefore did not enable easy restoration in case the alignment was disturbed.

An arrangement to control all motion of the test cell for the flowing setup would greatly benefit any future experiments. Precision micrometers could be used to control the rotation of the test cell ($\pm \delta$) (see Fig. 15). Micrometers to tip the test cell about an axis in the direction of the length of the cell (parallel to the direction of flow) would be very useful. This is especially important, as when the test cell is tipped to prevent reflections from the cell wall being detected, a bearing on the actual depth of the beam inside the test cell is lost. The presence of the micrometer would enable determination of the exact amount of tip of the test cell, from which the depth of the beam inside the cell can be calculated.

Experiments conducted on larger particles failed because of low intensities received by scattering. This reason for this failure was explained in Section 6.3.3 using the Rayleigh-Gans form factor. It was also shown how smaller (80°–100°) scattering angles (larger α angles) could increase the amount of scattering intensities seen to workable levels. The present design allows a maximum arm movement of 48° (α). This limitation can be overcome by milling out the side walls (by about 1 inch) of the goniometer on both sides, which would increase the range of α angles by 10°, without compromising the stability of the goniometer. This would help in experimenting with particles of larger diameter.

Another area which could be improved is the use of narrow slits to block reflections from the test cell wall to the detectors. The present use of black electrical tape worked, but a more sophisticated arrangement is desirable.

The implementation of the suggestions made would make experimenting with this sensitive setup easier and more efficient.

Although quite a few parameters were investigated in this thesis, there are other parameters that were left to be explored. One interesting extension of this research is to size particles in suspensions that contain a mix of particles, and determine the size distribution of the particles. Another interesting aspect would be to experiment with particles that also absorb, instead of just scatter light, and see if absorption affects particle sizing.

If the goniometer design is improved to allow greater angles of the laser and the detector arms, larger particles can be studied. The effects of hydrodynamic settling of larger particles need to be investigated by sizing stagnant suspensions of larger particles to see if a correlation exists between the velocity of settling and particle radius predicted.

The equation that predicts the S/N ratio [Nobbmann *et al.* (1997)] can be improved in one respect. The original equation has two parameters 'A' and 'B', which represent the amount of multiple and single scattering present in the sample respectively. These two parameters influence the shape of the Y-intercept curve together, because of the presence of the third term that involves both 'A' and 'B', when $\gamma(\phi)$ is squared to obtain the Y-intercept. The equation can be controlled to fit the experimental data at the peak and shoulders independently, if 'A' and 'B' are independently controllable, without affecting the other. If this can be done, the theoretical curve can be made to fit the experimental data better, giving a more accurate idea of the ratio of the multiple to the single scattering actually present, as is measured by the experimental data. A study of the correlation between the quantity $B\sqrt{\delta_t}$ that gives the best fit to the experimental S/N curve, and the volume fraction of the sample would be very helpful in controlling the values of the terms, in the process of predicting the S/N ratio more accurately.

This research has been a success in terms of verifying and proving the feasibility of using two independent suppression techniques in conjunction, to accomplish a major goal of particle sizing in dense flowing media. The study of the theoretical prediction of the S/N ratio was reasonably successful.

Implementing the recommendations will make particle sizing experiments more controllable and repeatable. It will be possible to extend the range of usefulness of this technique of multiple scattering and flow suppression to larger velocities, concentrations and particle sizes. A better understanding of the theoretical prediction of the S/N ratio will enable prediction of the amount of angular separation required to suppress multiple scattering effects, without having to experimentally determine it for each volume fraction. Any advancement to the research done in this thesis will be beneficial not only to industries that work with microscopic particles, but eventually to all mankind.

REFERENCES

Aberle, L.B., Hülstede, P., Wiegand, S., Schröer, W., and Staude, W. (1998), "Effective Suppression of Multiply Scattered Light in Static and Dynamic Light Scattering," **Applied Optics**, Vol. 37, No. 27, pp. 6511-6524.

Ackerson, B.J. (1986), *Selected Topics in Static and Dynamic Light Scattering*, a series of lectures presented during the fall of 1986, Van't Hoff Laboratory, University of Utrecht, The Netherlands.

Ackerson, B.J. and Clark, N.A. (1981), "Dynamic Light Scattering at Low Rates of Shear," **Journal of Physique**, Vol. 42, pp. 929-936.

Ackerson, B.J., Dougherty, R.L., Reguigui, N.M., and Nobbmann, U. (1992), "Correlation Transfer: Application of Radiative Transfer Solution Methods to Photon Correlation Problems," **Journal of Thermophysics and Heat Transfer**, Vol. 6, No. 4, pp. 577-588.

ALV-Laser Vertiebsgesellschaft m.b.H., *ALV-5000/E Multiple Tau Digital Correlator Reference Manual for Software Version 5.0*, June 1993.

Berne, B.J. and Pecora, R. (1976), *Dynamic Light Scattering*, John Wiley and Sons, Inc., New York, NY.

Brown, R.G.W. (1987), "Dynamic Light Scattering Using Monomode Optical Fibers," **Applied Optics**, Vol. 26, No. 22, pp. 4846-4851.

Cambern, R.M. (1999), "Multiple Scattering Suppression for Cross-Correlation of a Flowing Fluid to Determine Particle Size," Masters Thesis, School of Mechanical and Aerospace Engineering, Oklahoma State University, Stillwater, Oklahoma.

Dhont, J.K.G. and de Kruif, C.G. (1983), "Scattered Light Intensity Cross-Correlation. I. Theory," **Journal of Chemical Physics**, Vol. 79, pp.1658-1663.

Dorri-Nowkoorani, F., Nobbmann, U., Reguigui, N.M., Ackerson, B.J., and Dougherty, R.L. (1993), "Correlation Measurements of a Multiply Scattered Laser Beam by Fluid/Particle Suspensions," AIAA 93-2745, AIAA 28th Thermophysics Conference, Orlando, FL, July 6-9.

Dorri-Nowkoorani, F. (1995), "Multiple Scattering Correlation Measurements in

Fluid/Particle Suspensions: Application to Particle Characterization," Ph.D. Dissertation, School of Mechanical and Aerospace Engineering, Oklahoma State University, Stillwater, Oklahoma.

Dougherty, R.L., Ackerson, B.J., Reguigui, N.M., and Nobbmann, U. (1991), "Correlation Transfer: Application of Radiative Transfer Solution Methods to Photon Correlation in Optically Dense Media," AIAA 91-1433, AIAA 26th Thermophysics Conference, Honolulu, Hawaii, June 24-26.

Dougherty, R.L., Ackerson, B.J., Reguigui, N.M., Dorri-Nowkoorani, F., and Nobbmann, U. (1994), "Correlation Transfer: Development and Application," **Journal of Quantitative Spectroscopy and Radiative Transfer**, Vol. 52, No. 6, pp. 713-727.

Duke Scientific Corporation, *Particle Specifications,* Bulletin 92K, September 1997.

Hoppenbrouwers, M. and van de Water, W. (1998), "Dynamic Light Scattering in Shear Flow," **Physics of Fluids**, Vol. 10, No. 9, pp. 2128-2136.

Lock, J.A. (1997a), "Theory of Multiple Scattering Suppression in Cross-Correlated Light Scattering Employing a Single Laser Beam," in *Light Scattering and Photon Correlation Spectroscopy*, Pike, E. R. and Abbiss, J. B., eds., NATO Series, Kluwer, Dordrcht, The Netherlands, pp. 51-64.

Lock, J.A. (1997b), "Role of Multiple Scattering in Cross-Correlated Light Scattering with a Single Laser Beam," **Applied Optics**, Vol. 36, No. 30, pp. 7559-7570.

Melles-Griot Company, *Optical Instruments Catalog,* 1995/96.

Meyer, W.V., Cannell, D.S., Smart, A.E., Taylor, T.W., and Tin, P. (1997a), "Suppression of Multiple Scattering Using a Single Beam Cross-Correlation Method," in *Light Scattering and Photon Correlation Spectroscopy*, Pike, E.R. and Abbiss, J.B., eds., NATO Series, Kluwer, Dordrcht, The Netherlands, pp. 39-50.

Meyer, W.V., Cannell, D.S., Smart, A.E., Taylor, T.W., and Tin, P. (1997b), "Multiple-Scattering Suppression by Cross-Correlation," **Applied Optics**, Vol. 36, No. 30, pp. 7551-7558.

Mos, H.J., Pathmamonoharan, C., Dhont, J.K.G., and de Kruif, C.G. (1986), "Scattered Light Intensity Cross-Correlation. II. Experimental," **Journal of Chemical Physics**, Vol. 84, pp. 45-49.

Nobbmann, U., Jones, S.W., and Ackerson, B.J. (1997), "Multiple-Scattering Suppression: Cross-Correlation with Tilted Singled-Mode Fibers," **Applied Optics**, Vol. 36, No. 30, pp. 7571-7576.

Phillies, G.D.J. (1981), "Suppression of Multiple Scattering Effects in Quasielastic Light Scattering by Homodyne Cross-Correlation Techniques," **Journal of Chemical Physics**, Vol. 74, pp. 260-262.

Pine, D.J., Weitz, D.A., Chaikin, P.M., and Herbolzheimer, E. (1988), "Diffusing-Wave Spectroscopy," **Physical Review Letters**, Vol. 60, No. 12, pp. 1134-1137.

Schätzel, K., Drewel, M., and Ahrens, J. (1990), "Suppression of Multiple Scattering in Photon Correlation Spectroscopy," **Journal of Physics: Condensed Matter** Vol. 2, pp. SA393-SA398.

White, F.M. (1991), *Viscous Fluid Flow*, 2nd edition, McGraw-Hill, Inc., New York, NY.

Wiese, H. and Horn, D. (1991), "Single-Mode Fibers in Fiber-Optic Quasielastic Light Scattering: A Study of the Dynamics of Concentrated Latex Dispersions," **Journal of Chemical Physics**, Vol. 94, pp. 6429-6443.

Weiner, B.W. (1984), "Particle Sizing Using Photon Correlation Spectroscopy," in *Modern Methods of Particle Size Analysis*, edited by Barth, H.B., John Wiley and Sons, Inc., New York, NY.

APPENDICES

APPENDIX I

Equipment List

1. **Laser (Non flowing experiments)**: 20 mW Helium Neon laser manufactured by Uniphase with a wavelength of 632.5 nm, Model No. 1135P.

2. **Laser (Flowing experiments)**: 100 mW Neodymium-Yttrium-Silver laser manufactured by Adlas with a wavelength of 532.5 nm, Model No. DPY315II.

3. **Correlator software**: ALV-5000/E Multiple Tau Digital Correlator by ALV-Laser Vertriebsgesellschaft m.b.H Germany.

4. **Goniometer (Non-flowing experiments)**: Designed and built by the OSU Chemistry/ Physics Machine shop.

5. **Goniometer (Flowing experiments)**: Designed and built by the OSU Chemistry/ Physics Machine shop, and was made of Aluminum.

6. **Stepper motors (Flow Goniometer)**: Manufactured by Eastern Air Devices. Model Number PN LA34AGK-2, 2.9 V D/C, 3.1 amps, 1.8 degrees/step, 110 Oz-in running torque.

7. **Translation stages**: Model No. 426a, manufactured by Newport and equipped with SM-25 micrometers were used for the top fiber mount. Dimensions of the stages were 89 mm x 89 mm x 25.4 mm with a 50.8 mm diameter hole in the center. The aluminum tilt plates were produced by the OSU Chemistry/Physics Machine Shop and had dimensions of 127 mm x 134 mm x 10 mm.

8. **Back fiber mount**: Manufactured by the OSU Chemistry/Physics Machine Shop, had two main pieces, the mount plate and the piece that carried the set screws. The dimensions of the mount plate were 101.6 mm x 101.6 mm x 12.7 mm with a 34.5 mm diameter hole in the center. The dimensions of the second piece were 101.6 mm x 101.6 mm x 22.9 mm with a 34.5 mm diameter hole in the center.

9. **Beam-splitter (Non-flowing experiments)**: 632.5 nm wavelength specific beamsplitter from Newport, Model No. 05BC16-NP.4.

10. **Beam-splitter (Flowing experiments)**: Multi-band, nonpolarizing beamsplitter, Model No. 05FC16-PB.3 by Newport.

11. **Fiber Optic Cables**: Manufactured by Oz Optics LTD. Part No. LPC-02-532-4/125-P-0.7-3.2GR-30-1-3-3.

12. **Photomultiplier tubes**: Manufactured by Thorn EMI Electron Tubes Inc., Model No. EBA-805.

13. **Power supplies**: Two power supplies produced by Global Specialties, Model Nos. 1310 and 1302.

14. **Attenuator holder**: Manufactured by Newport, Model No. FH-1.

15. **Polystyrene Latex particles**: Core samples of particles from Duke Scientific:

    A. 0.107 μm diameter; 10 percent solids by weight; 5.6% Coefficient of Variation, Catalog No. 5010A-Lot No. 16456
    B. 0.098 μm diameter; 10 percent solids by weight; 6.2% C.V., Catalog No. 5010A-Lot No. 20259
    C. 0.203 μm diameter; 10 percent solids by weight; 2.1% C.V., Catalog No. 5020A-Lot No. 20500
    D. 0.204 μm ± 6 nm diameter; 1 percent solids by weight; Catalog No. 3200A-Lot No. 20613
    E. 0.300 μm ± 5 nm diameter; 1 percent solids by weight; Catalog No. 3300A-Lot No. 20286.

16. **Index matching vat**: Water bath container formed from 64-stock glass tubing in Oklahoma State Glass Shop with dimensions of 6.35 cm outside diameter having a wall thickness of 2.4 mm and a height of 8.89 cm.

17. **Test cell (Non-flowing experiments)**: Test tube manufactured by Fisher Scientific from borosilicate glass with dimensions of 10 mm x 75 mm, Catalog No. 14-961-25.

18. **Test cell (Flowing experiments)**: 6 mm x 8 mm 30.5 cm rectangular test cell with a 0.9 mm wall thickness, manufactured by Wilmad Glass from clear fused quartz, Catalog No. WQR-0608.

19. **Tubes**: 1/8" x 1/16" tubing manufactured by Tygon, S-50-HL, Class VI.

20. **Holding tanks**: Dimensions of 215 mm x 69.5 mm x 49.5 mm were manufactured from Plexiglas by the Oklahoma State University Physics Machine Shop. The side walls were 12 mm thick, while the lid and base were 9 mm thick. The lid was sealed to the base by 21 screws and a rubber gasket.

21. **Shuttle pump**: Manufactured by Instech Labs, Model No. S20P.

22. **Optical Power Meter**: Manufactured by Newport Inc., Model No. 840 with wand Model No. 818-ST.

23. **Deionizer**: E-pure deionizer, Model No. D4641, manufactured by Barnstead and Thermolyne.

24. **Electronic lab scale**: Model No. 31205, by Sartorious.

25. **Parafilm**: Lab film manufactured by American National Can was used to seal test tubes.

APPENDIX II

Non Flowing Case: Experimental Data

Table 4: Summary of the Non-Flowing Fluid Experiments Discussed by Cambern (1999) and in this Thesis.

Experiment Number	Scattering Angle (deg)	Test Cell Type	Volume Fraction (% by weight)	Particle Diameter (μm)
32	90	Square	0.3239	0.107
33	90	Square	0.3239	0.107
34	90	Square	0.1536	0.107
35	90	Square	0.1536	0.107
36	90	Square	0.4285	0.107
37	90	Square	0.4285	0.107
38	90	Circular	0.1330	0.107
39	90	Circular	0.3201	0.107
40	30	Circular	0.3201	0.107
41	30	Circular	0.3201	0.107
42	Sweep	Circular	Single	0.107
43	60	Circular	0.3271	0.107
44	60	Circular	0.1545	0.107
45	Sweep	Circular	Single	0.107
46	120	Circular	0.5025	0.107
47	120	Circular	0.3795	0.107
48	45	Circular	0.3795	0.107

Note: Detailed data for Experiments 32-37 appear in Table 5, and detailed data for Experiments 38-48 are given by Cambern (1999).

Table 5: Detailed Description of Experiments 32-37 Described in Summary Table 4.

Exp 32 0.107 µm PSL; Square Cell; V.F.=0.3239%; θ=90°
Front Tilt = 16.86 divs Side Translation = 11.37 divs

S.No.	Top Fiber Mic. Rdgs.		Count Rate		Cumulant - 2 Fit Data				Duration
	Rear Tilt	Front Translation	Ch 0	Ch 1	Y-Int	Decay Rate	Radius	Norm 2nd Cumulant	
	(divs)		(KHz)		(-)	(/ ms)	(nm)	(-)	(s)
1	17.3	15.12	169.532	129.888	0.902	3.19	25.3.	0.23	120
2	17.35	15.2	168.217	128.56	0.858	3.14	25.7	0.23	
3	17.37	15.32	169.119	128.18	0.666	2.84	28.5	0.21	
4	17.39	15.48	168.325	125.949	0.388	2.29	35.3	0.19	
5	17.41	15.5	173.462	132.644	0.347	2.07	38.92	0.17	
6	17.43	15.64	169.506	130.062	0.244	1.73	46.5	0.094	
7	17.45	15.76	169.914	128.178	0.202	1.61	50	0.062	
8	17.47	15.79	170.149	131.257	0.195	1.55	52.1	0.019	
9	17.49	15.86	168.971	131.756	0.181	1.56	51.8	0.031	
10	17.51	15.92	169.812	133.226	0.177	1.58	51.1	0.067	
11	17.53	16.09	169.222	135.584	0.163	1.52	53	0.0011	
12	17.55	16.15	165.452	132.937	0.158	1.5	53.9	0.022	
13	17.57	16.28	165.871	130.75	0.141	1.53	52.6	0.012	
14	17.59	16.35	165.102	128.875	0.138	1.41	57.1	-0.008	
15	17.61	16.49	165.612	129.151	0.128	1.47	55.1	-0.038	
16	17.63	16.59	165.087	129.399	0.123	1.46	55.4	0.0037	
17	17.65	16.67	167.29	128.105	0.116	1.51	53.4	-0.004	
18	17.67	16.77	165.782	125.111	0.109	1.46	55.3	0.038	
19	17.69	16.85	166.356	121.715	0.0983	1.44	56.1	-0.0038	
20	17.71	16.94	167.071	121.286	0.0884	1.49	54.1	0.027	
21	17.73	17.06	164.881	120.701	0.0816	1.59	50.9	0.11	
22	17.75	17.22	165.34	122.37	0.0756	1.51	53.5	0.0059	
23	17.77	17.32	165.318	121.056	0.065	1.49	54.3	0.0054	
24	17.79	17.45	171.17	124.493	0.0567	1.48	54.6	0.032	
25	17.81	17.58	171.004	124.863	0.0547	1.61	50.1	0.13	
26	17.83	17.65	170.859	127.996	0.0526	1.68	48.1	0.17	
27	17.85	17.72	163.502	129.056	0.0511	1.55	51.9	0.03	
28	17.87	17.76	165.989	129.91	0.0463	1.23	65.4	-0.11	
29	17.31	15.04	170.586	122.759	0.65	2.87	27.4	0.23	
30	17.29	14.93	172.19	124.062	0.44	2.39	33	0.19	
31	1727	14.82	172.199	123.154	0.305	2.04	38.5	0.16	
32	17.25	14.68	173.497	126.465	0.242	1.76	44.8	0.098	
33	17.23	14.6	173.361	125.025	0.212	1.68	46.9	0.084	
34	17.21	14.5	173.769	124.98	0.191	1.59	49.5	0.055	
35	17.19	14.38	173.545	124.49	0.166	1.49	52.8	0.031	
36	17.17	14.25	173.943	125.254	154	1.46	53.9	0.07	
37	17.15	14.15	173.969	125.647	0.144	1.49	52.7	-0.0054	
38	17.13	14.06	173.325	125.03	0.139	1.52	52	0.03	
39	17.11	13.98	169.288	124.01	0.134	1.49	52.9	0.014	
40	17.09	13.88	170.35	126.784	0.13	1.53	51.5	0.094	
41	17.07	13.7	167.557	123.015	0.113	1.47	53.5	-0.03	
42	17.05	13.58	169.43	123.747	0.104	1.49	53	-0.0011	
43	17.03	13.48	169.799	120.447	0.0967	1.5	52.5	0.055	
44	17.01	13.41	168.638	123.41	0.0938	1.48	53.2	0.0078	
45	16.99	13.32	170.883	123.41	0.0872	1.58	50.5	0.024	
46	16.97	13.24	173.624	125.132	0.0828	1.55	50.8	0.01	
47	16.95	13.13	171.103	123.996	0.0743	1.43	55	0.093	
48	16.93	13.04	173.169	123.864	0.0679	1.43	55	-0.045	
49	16.91	12.92	173.106	124.16	0.0647	1.47	53.7	0.059	
50	16.89	12.81	171.221	122.718	0.0566	1.38	57.2	-0.12	
51	16.87	12.67	171.511	124.053	0.0482	1.46	53.8	-0.072	
52	16.85	12.55	171.389	124.337	0.0417	1.66	47.5	0.23	
53	16.83	12.46	171.613	123.805	0.0385	1.49	53	-0.088	
54	16.81	12.37	169.958	124.469	0.0353	1.46	54.1	-0.012	
55	16.79	12.27	168.646	124.178	0.0329	1.62	48.5	0.036	
56	16.77	12.18	167.891	122.33	0.0294	1.48	53.1	0.043	
57	16.75	12.04	167.908	125.699	0.0268	1.28	61.4	-0.07	

Exp 33 0.107 µm PSL, Square Cell; V.F.=0.3239%; θ=90°

Front Tilt = 16.85 divs Side Translation = 11.38 divs

S.No.	Top Fiber Mic. Rdgs.		Count Rate		Cumulant - 2 Fit Data				Duration
	Rear Tilt	Front Translation	Ch 0	Ch 1	Y-Int	Decay Rate	Radius	Norm 2nd Cumulant	
	(divs)		(KHz)		(-)	(/ ms)	(nm)	(-)	(s)
1	17.38	15.09	239.697	186.509	0.9	2.84	27.7	0.226	120
2	17.39	15.145	239.221	186.409	0.876	2.8	28.1	0.21	
3	17.4	15.21	238.227	183.027	0.785	2.7	29.2	0.21	
4	17.41	15.28	236.347	181.358	0.669	2.54	31	0.2	
5	17.42	15.34	235.093	180.421	0.549	2.35	33.5	0.19	
6	17.43	15.42	235.544	182.765	0.448	2.11	37.3	0.16	
7	17.44	15.49	238.175	180.502	0.367	1.97	40	0.15	
8	17.45	15.53	235.299	182.427	0.34	1.85	42.6	0.12	
9	17.46	15.57	236.737	182.644	0.31	1.75	45	0.089	
10	17.47	15.62	235.635	181.655	0.287	1.74	45.3	0.094	
11	17.48	15.67	235.876	181.26	0.26	1.68	46.9	0.1	
12	17.49	15.71	235.542	180.293	0.247	1.65	47.7	0.061	
13	17.5	15.76	234.898	180.221	0.242	1.6	49.3	0.053	
14	17.51	15.78	239.489	189.4	0.234	1.59	49.6	0.0259	
15	17.52	15.82	235.299	180.764	0.225	1.56	50.4	0.048	
16	17.54	15.93	235.674	183.528	0.216	1.54	51.1	0.08	
17	17.56	16	238.365	183.081	0.207	1.53	51.6	0.043	
18	17.58	16.15	239.13	182.419	0.194	1.43	51.5	-0.014	
19	17.6	16.27	240.192	180.028	0.182	1.44	54.6	0.015	
20	17.62	16.38	241.536	179.264	0.179	1.5	52.7	0.0013	
21	17.64	16.47	241.569	179.431	0.173	1.49	52.8	0.0069	
22	17.66	16.6	236.135	178.685	0.165	1.47	53.8	0.03	
23	17.68	16.69	240.787	179.51	0.155	1.46	53.8	-0.022	
24	17.7	16.8	240.694	177.571	0.142	1.51	52.3	0.068	
25	17.74	17.01	242.653	179.458	0.125	1.46	54.1	-0.057	
26	17.78	17.2	239.92	176.356	0.111	1.49	52.9	0.021	
27	17.82	17.41	237.315	181.603	0.0905	1.49	52.9	0.015	
28	17.86	17.61	236.027	183.868	0.0848	1.4	56.4	-0.005	
29	17.9	17.81	238.815	183.837	0.075	1.49	52.9	0.039	
30	17.94	18.03	238.359	190.507	0.0594	1.51	52.2	-0.014	
31	17.98	18.3	236.285	200.247	0.0521	1.53	51.1	0.011	
32	18.02	18.4	235.989	137.737	0.0339	1.41	55.4	-0.019	
33	18	18.36	237.475	172.147	0.0448	1.63	47.9	0.12	
34	18.04	18.45	221.55	100.008	0.0182	1.47	52.9	0.073	
35	17.37	15.08	223.67	171.726	0.888	2.9	26.9	0.21	
36	17.36	15.05	222.321	173.717	0.861	2.87	27.2	0.21	
37	17.35	15	222.532	174.135	0.783	2.77	28.1	0.22	
38	17.34	14.95	222.494	173.272	0.68	2.59	30.1	0.2	
39	17.33	14.92	221.381	172.708	0.605	2.51	31.1	0.2	
40	17.32	14.88	221.317	171.622	0.517	2.35	33.2	0.19	
41	17.31	14.83	221.949	170.289	0.431	2.17	35.9	0.17	
42	17.3	14.76	221.591	168.884	0.353	2.02	38.7	0.15	
43	17.29	14.69	221.473	167.12	0.301	1.86	41.9	0.14	
44	17.28	14.64	223.652	166.004	0.276	1.73	45	0.088	
45	17.27	14.6	223.054	167.577	0.261	1.68	46.5	0.098	
46	17.26	14.53	222.539	167.382	0.239	1.63	47.8	0.088	
47	17.25	14.46	222.324	168.62	0.228	1.58	49.5	0.064	
48	17.24	14.41	222.608	171.361	0.219	1.53	51.1	0.055	
49	17.22	14.32	227.055	170.057	0.206	1.5	52.2	-0.0059	
50	17.2	14.25	228.209	167.424	0.192	1.52	51.7	0.088	
51	17.18	14.15	230.886	165.239	0.181	1.47	53.5	-0.028	
52	17.16	14.04	229.911	166.827	0.177	1.51	52	0.046	
53	17.14	13.95	210.329	168.324	0.174	1.53	51.3	0.062	
54	17.12	13.82	210.823	169.305	0.166	1.48	53	-0.015	
55	17.1	13.76	223.683	169.939	0.162	1.55	50.5	0.053	
56	17.08	13.64	223.008	168.476	0.146	1.51	51.9	0.032	
57	17.06	13.52	222.685	166.105	0.133	1.55	50.7	0.04	
58	17.04	13.39	221.967	167.232	0.124	1.49	52.6	0.041	
59	17.02	13.28	221.523	169.286	0.121	1.44	54.3	0.0068	
60	17	13.15	221.672	170.247	0.111	1.38	57	-0.0079	
61	16.98	13.03	221.857	170.425	0.0951	1.47	53.2	-0.036	
62	16.96	12.96	221.593	169.103	0.091	1.44	54.3	-0.079	
63	16.94	12.87	221.049	169.342	0.0847	1.42	55.3	0.0041	
64	16.92	12.75	222.083	170.394	0.0746	1.52	51.6	0.098	
65	16.9	12.65	222.168	172.873	0.0669	1.52	51.6	0.079	
66	16.88	12.54	221.795	174.32	0.0624	1.45	53.9	-0.011	

Exp 34 0.107 μm PSL; Square Cell; V.F.=0.1536%; θ=90°

Front Tilt = 16.825 divs Side Translation = 11.38 divs

S.No.	Top Fiber Mic. Rdgs.		Count Rate		Cumulant - 2 Fit Data				Duration
	Rear Tilt	Front Translation	Ch 0	Ch 1	Y-Int	Decay Rate	Radius	Norm 2nd Cumulant	
	(divs)		(KHz)		(-)	(/ ms)	(nm)	(-)	(s)
1	17.38	15.09	208.031	177.093	0.927	1.81	43.5	0.1	120
2	17.4	15.13	208.077	186.57	0.912	1.75	44.8	0.098	
3	17.42	15.16	210.631	190.549	0.855	1.75	44.8	0.09	
4	17.44	15.26	26.435	183.656	0.754	1.69	46.5	0.087	
5	17.46	15.38	205.746	180.167	0.645	1.59	49.3	0.068	
6	17.48	15.52	205.841	177.327	0.548	1.51	51.9	0.019	
7	17.5	15.62	204.7	178.3	0.501	1.47	53.2	0.04	
8	17.52	15.7	202.04	177.072	0.46	1.46	53.9	0.012	
9	17.54	15.8	203.369	177.002	0.424	1.44	54.6	-0.0031	
10	17.56	15.93	202.79	177.148	0.386	1.44	54.6	0.015	
11	17.58	16.04	201.749	179.832	0.361	1.45	54.1	0.025	
12	17.6	16.13	195.251	171.168	0.34	1.45	54.1	0.032	
13	17.62	16.21	199.803	178.62	0.318	1.48	53	0.013	
14	17.64	16.34	196.216	173.101	0.274	1.42	54.6	0.015	
15	17.66	16.46	198.833	175.212	0.235	1.45	53.4	0.056	
16	17.68	16.53	193.531	175.696	0.199	1.5	51.9	0.0021	
17	17.7	16.62	199.85	181.352	0.183	1.51	53.4	0.0037	
18	17.72	16.73	199.481	181.348	0.165	1.52	53.2	0.05	
19	17.74	16.83	200.048	179.215	0.148	1.56	52	0.051	
20	17.76	16.98	199.703	172.815	0.115	1.49	54.4	0.0058	
21	17.78	17.12	198.324	165.617	0.0938	1.55	52.3	0.025	
22	17.8	17.15	198.824	167.822	0.0857	1.53	52.9	0.085	
23	17.82	17.27	197.991	167.167	0.0784	1.56	51.7	0.028	
24	17.84	17.35	198.092	168.733	0.0689	1.51	53.7	0.017	
25	17.86	17.43	194.26	165.638	0.0594	1.54	52.5	0.084	
26	17.88	17.55	184.951	166.035	0.0479	1.6	50.4	0.073	
27	17.9	17.61	202.533	164.105	0.0393	1.6	50.6	0.064	
28	17.92	17.69	202.644	165.217	0.038	1.51	53.7	0.11	
29	17.94	17.78	198.818	166.663	0.0373	1.37	59.2	-0.053	
30	17.36	14.95	201.12	173.852	0.828	1.82	44.4	0.1	
31	17.34	14.82	196.654	174.177	0.7	1.7	47.7	0.077	
32	17.32	14.76	199.788	171.203	0.627	1.66	48.6	0.07	
33	17.3	14.64	199.628	171.479	0.548	1.59	51	0.053	
34	17.28	14.49	201.606	170.952	0.481	1.52	53.3	0.0032	
35	17.26	14.35	201.157	167.865	0.419	1.53	53	0.015	
36	17.24	14.27	201.254	167.742	0.391	1.5	53.9	0.0054	
37	17.22	14.19	200.684	169.035	0.38	1.54	52.7	0.057	
38	17.2	14.1	199.9	169.625	0.359	1.52	53.2	0.03	
39	17.18	14	196.403	170.943	0.332	1.51	53.6	0.014	
40	17.16	13.89	195.639	167.083	0.298	1.53	53.1	0.015	
41	17.14	13.78	209.126	167.935	0.252	1.52	53.3	0.048	
42	17.12	13.68	206.438	173.83	0.229	1.47	55	0.012	
43	17.1	13.56	207.163	180.614	0.209	1.51	53.7	0.059	
44	17.08	13.46	190.542	164.299	0.189	1.48	54.8	0.0028	
45	17.06	13.37	206.962	176.109	0.171	1.5	53.9	-0.037	
46	17.04	13.28	207	175.973	0.151	1.5	54.1	-0.011	
47	17.02	13.17	208.819	178.025	0.13	1.49	54.2	0.019	
48	17	13.07	208.514	178.572	0.113	1.55	52.1	0.048	
49	16.98	12.97	208.082	177.696	0.102	1.41	57.6	-0.06	
50	16.96	12.87	207.34	176.482	0.0861	1.49	54.9	0.028	
51	16.94	12.76	208.54	176.857	0.0727	1.45	55.9	-0.085	

Exp 35 0.107 μm PSL; Square Cell; V.F.=0.1536%; θ=90°

Front Tilt = 16.82 divs Side Translation = 11.38 divs

S.No.	Top Fiber Mic. Rdgs.		Count Rate		Cumulant - 2 Fit Data				Duration
	Rear Tilt	Front Translation	Ch 0	Ch 1	Y-Int	Decay Rate	Radius	Norm 2nd Cumulant	
	(divs)		(KHz)		(-)	(/ ms)	(nm)	(-)	(s)
1	17.38	15.09	202.46	146.542	0.929	1.86	43.6	0.12	120
2	17.37	15.04	201.481	148.49	0.911	1.86	43.6	0.11	
3	17.36	14.99	200.699	149.327	0.897	1.82	44.5	0.092	
4	17.35	14.93	200.791	152.856	0.84	1.74	46.6	0.089	
5	17.34	14.875	200.464	152.893	0.769	1.7	47.7	0.079	
6	17.33	14.82	199.104	155.087	0.697	1.65	49	0.059	
7	17.32	14.77	200.437	155.084	0.644	1.63	49.7	0.05	
8	17.31	14.72	200.77	155.943	0.598	1.56	52	0.05	
9	17.3	14.675	199.72	154.311	0.566	1.54	52.4	0.029	
10	17.28	14.55	197.222	156.69	0.537	1.56	52	0.032	
11	17.26	14.435	197.049	153.845	0.431	1.52	53.3	0.03	
12	17.24	14.32	196.427	156.136	0.394	1.53	53.1	0.018	
13	17.22	14.24	193.837	154.976	0.374	1.52	53.2	-0.0084	
14	17.2	14.13	197.05	162.351	0.361	1.49	54.3	0.024	
15	17.18	14.02	193.231	162.129	0.325	1.49	54.2	0.0147	
16	17.16	13.92	199.749	152.991	0.289	1.51	53.8	0.017	
17	17.14	13.76	200.413	160.868	0.243	1.45	55.8	-0.024	
18	17.12	13.67	199.901	159.276	0.221	1.45	55.8	-0.049	
19	17.1	13.58	200.157	156.798	0.204	1.53	53	-0.004	
20	17.08	13.485	215.704	161.512	0.198	1.5	54	0.031	
21	17.06	13.38	202.454	155.406	0.17	1.48	54.7	0.0026	
22	17.04	13.28	201.806	160.849	0.15	1.48	54.5	0.059	
23	17.02	13.185	202.483	161.036	0.128	1.5	53.9	-0.0055	
24	17	13.09	204.405	161.157	0.113	1.55	52.2	0.066	
25	16.98	12.98	199.678	161.463	0.102	1.51	53.6	-0.046	
26	16.96	12.87	204.284	168.834	0.0901	1.43	56.8	0.032	
27	16.94	12.745	202.954	167.972	0.0703	1.48	54.8	0.023	
28	16.92	12.66	202.999	164.537	0.0602	1.44	56.1	0.039	
29	16.9	12.55	203.038	168.158	0.0525	1.47	54.9	0.00052	
30	16.88	12.44	202.617	169.252	0.0482	1.45	55.7	0.081	
31	16.86	12.34	202.443	165.49	0.0417	1.39	58.4	0.0094	
32	16.84	12.21	204.475	169.216	0.0326	1.27	63.7	-0.18	
33	17.39	15.09	203.606	158.31	0.926	1.88	43.4	0.11	
34	17.4	15.13	217.822	158.751	0.914	1.84	43	0.1	
35	17.41	15.19	195.343	170.429	0.879	1.79	43.9	0.094	
36	17.42	15.23	204.564	156.891	0.831	1.78	45.2	0.1	
37	17.43	15.27	207.059	164.23	0.779	1.71	45.5	0.099	
38	17.44	15.33	205.395	161.231	0.711	1.67	47.4	0.072	
39	17.45	15.36	205.031	158.894	0.667	1.62	48.4	0.086	
40	17.46	15.41	205.619	162.922	0.622	1.59	50	0.046	
41	17.47	15.475	205.534	155.876	0.566	1.59	51	0.034	
42	17.48	15.53	205.583	157.664	0.52	1.54	51	0.039	
43	17.5	15.59	205.655	166.964	0.495	1.52	52.5	0.017	
44	17.52	15.64	205.655	173.023	0.473	1.51	53.1	0.021	
45	17.54	15.69	206.319	174.042	0.453	1.5	53.5	0.04	
46	17.56	15.77	206.043	170.812	0.417	1.52	53.9	0.019	
47	17.58	15.85	205.963	170.151	0.385	1.5	53.4	0.026	
48	17.6	15.94	206.2	170.598	0.36	1.5	53.8	0.031	
49	17.62	16.015	206.538	171.63	0.346	1.51	54.1	0.0176	
50	17.64	16.13	206.67	173.901	0.321	1.52	53.6	0.031	
51	17.66	16.24	205.721	171.182	0.279	1.51	52.4	0.00031	
52	17.68	16.39	206.258	170.733	0.228	1.45	53.7	-0.015	
53	17.7	16.52	206.094	172.357	0.206	1.58	55.8	-0.045	
54	17.72	16.62	206.205	172.978	0.185	1.48	51.3	0.077	
55	17.74	16.69	199.575	172.765	0.177	1.51	54.8	0.063	
56	17.76	16.81	203.614	172.108	0.148	1.47	53.5	0.0068	
57	17.78	17	197.514	160.924	0.109	1.58	55	0.046	
58	17.8	17.08	196.733	159.376	0.0929	1.53	51.1	0.041	
59	17.82	17.19	197.168	157.778	0.0828	1.54	53	0.042	
60	17.84	17.26	198.895	159.627	0.0751	1.52	52.6	-0.0024	120
61	17.86	17.38	211.43	158.901	0.0577	1.54	53.3	0.016	300
62	17.88	17.55	198.946	157.23	0.0467	1.45	52.7	0.11	
63	17.9	17.6	198.256	162.343	0.0413	1.4	55.9	-0.085	
64	17.92	17.64	194.272	155.101	0.038	1.39	58.1	-0.19	

Exp 36 0.107 µm PSL; Square Cell; V.F.=0.4285%; θ=90°

Front Tilt = 16.82 divs Side Translation = 11.36 divs

S.No.	Top Fiber Mic. Rdgs.		Count Rate		Cumulant - 2 Fit Data				Dur.
	Rear Tilt	Front Translation	Ch 0	Ch 1	Y-Int	Decay Rate	Radius	Norm 2nd Cumulant	
	(divs)		(KHz)		(-)	(/ ms)	(nm)	(-)	(s)
1	17.38	15.09	159.185	121.339	0.898	4.72	17.4	0.24	120
2	17.39	15.09	155.641	124.974	0.897	4.59	17.9	0.23	
3	17.4	15.11	154.871	126.897	0.9	4.51	18.2	0.24	
4	17.41	15.135	155.08	128.474	0.844	4.44	18.5	0.24	
5	17.42	15.15	155.642	129.888	0.779	4.37	18.8	0.24	
6	17.43	15.18	155.142	129.989	0.707	4.23	19.4	0.24	
7	17.44	15.2	154.428	129.733	0.625	4.1	20	0.24	
8	17.45	15.24	154.683	129.366	0.48	3.69	22.3	0.24	
9	17.46	15.27	146.393	128.08	0.395	3.38	24.3	0.23	
10	17.47	15.365	144.711	128.211	0.263	2.84	28.9	0.21	
11	17.48	15.4	144.555	127.659	0.211	2.53	32.5	0.19	
12	17.49	15.43	152.068	129.778	0.179	2.33	35.1	0.16	
13	17.5	15.48	154.39	128.02	0.149	2.12	38.7	0.14	
14	17.51	15.56	151.185	127.796	0.122	1.88	43.6	0.08	
15	17.52	15.65	153.223	127.057	0.13	1.62	50.6	0.026	120
16	17.53	15.72	153.511	126.655	0.0916	1.59	51.6	0.028	300
17	17.54	15.74	156.71	123.715	0.0876	1.48	55.5	0.051	300
18	17.55	15.85	154.574	121.862	0.0776	1.5	54.6	-0.0059	
19	17.56	15.9	153.01	122.594	0.0753	1.55	53	0.046	
20	17.57	15.95	152.761	124.254	0.0745	1.54	53.9	-0.052	
21	17.59	16.02	153.27	126.17	0.0723	1.67	49.1	0.12	
22	17.61	16.08	154.609	127.651	0.068	1.67	49.2	0.082	
23	17.37	15.07	156.624	119.65	0.849	4.54	18	0.23	120
24	17.36	14.99	154.584	119.147	0.682	4.27	19.2	0.24	
25	17.35	14.925	156.251	120.793	0.504	3.92	20.9	0.23	
26	17.34	14.85	156.752	120.798	0.34	3.33	24.6	0.23	120
27	17.33	14.795	157.732	121.209	0.238	2.84	28.9	0.21	
28	17.32	14.75	159.071	121.544	0.19	2.49	32.9	0.21	
29	17.31	14.72	160.446	121.534	0.152	2.27	36.1	0.18	
30	17.3	14.66	160.945	122.021	0.126	1.96	41.9	0.14	
31	17.29	14.62	161.522	121.877	0.111	1.72	47.8	0.092	
32	17.28	14.5	149.53	120.894	0.0984	1.69	48	0.053	300
33	17.27	14.38	149.649	124.338	0.091	1.6	50.6	0.049	300
34	17.26	14.32	149.816	124.357	0.0839	1.59	50.8	0.015	
35	17.25	14.26	149.437	124.172	0.0799	1.5	54	-0.015	
36	17.24	14.195	149.623	123.411	0.0742	1.55	52.2	0.0058	
37	17.23	14.15	149.854	122.942	0.0704	1.55	52.1	-0.055	
38	17.22	14.105	149.715	122.639	0.0669	1.48	54.5	-0.066	
39	17.21	14.08	149.356	122.114	0.0637	1.52	53.2	0.0062	
40	17.2	14.03	149.004	122.113	0.0601	1.63	49.7	0.085	
41	17.19	13.98	149.609	121.526	0.0552	1.59	50.6	0.82	
42	17.17	13.895	149.594	121.385	0.0514	1.58	51.2	0.097	
43	17.15	13.82	149.759	120.828	0.0486	1.63	49.5	0.094	

Exp 37 0.107 µm PSL; Square Cell; V.F.=0.4285%; θ=90°
Front Tilt = 16.82 divs Side Translation = 11.36 divs

S.No.	Top Fiber Mic. Rdgs.		Count Rate		Cumulant - 2 Fit Data				Duration
	Rear Tilt	Front Translation	Ch 0	Ch 1	Y-Int	Decay Rate	Radius	Norm 2nd Cumulant	
	(divs)		(KHz)		(-)	(/ ms)	(nm)	(-)	(s)
1	17.38	15.09	152.55	117.071	0.89	4.6	17.6	0.24	120
2	17.39	15.11	152.481	117.802	0.889	4.59	17.8	0.23	
3	17.4	15.125	152.49	121.977	0.868	4.56	18.2	0.24	
4	17.41	15.14	149.488	124.004	0.821	4.45	18.3	0.24	
5	17.42	15.155	152.146	125.125	0.746	4.41	19	0.24	
6	17.43	15.195	151.947	125.178	0.653	4.25	19.7	0.24	
7	17.44	15.24	154.955	124.583	0.542	4.1	21.3	0.24	
8	17.45	15.28	152.368	126.548	0.425	3.8	23.4	0.23	
9	17.46	15.3	152.935	126.821	0.349	3.46	25.5	0.23	
10	17.47	15.34	148.78	126.786	0.273	3.17	27.9	0.22	
11	17.48	15.38	153.155	126.249	0.225	2.9	31.1	0.2	
12	17.49	15.41	153.078	124.754	0.182	2.6	34.4	0.2	
13	17.5	15.43	153.745	123.91	0.163	2.35	36.6	0.15	
14	17.51	15.5	153.309	124.132	0.133	2.21	41.3	0.097	240
15	17.52	15.6	153.765	125.321	0.109	1.96	46	0.081	
16	17.53	15.7	154.286	125.114	0.0924	1.76	47.9	0.056	
17	17.54	15.76	154.467	124.985	0.0853	1.69	52.1	0.013	
18	17.55	15.8	156.638	126.248	0.0833	1.55	51.6	-0.013	
19	17.56	15.85	157.488	126.803	0.0806	1.57	52.9	-0.027	
20	17.57	15.9	158.489	127.561	0.0798	1.53	50.6	0.0042	
21	17.58	15.94	159.408	128.186	0.0778	1.6	51.6	0.031	
22	17.59	15.98	159.652	127.103	0.0759	1.57	56.8	-0.038	
23	17.6	16.04	159.526	125.347	0.0733	1.59	50.6	0.056	
24	17.61	16.15	158.258	120.22	0.0655	1.6	52	-0.0036	
25	17.62	16.205	156.052	117.684	0.0617	1.56	51.4	0.011	
26	17.63	16.23	154.25	123.093	0.0615	1.57	53.5	-0.02	
27	17.64	16.28	156.716	124.967	0.0604	1.51	49.4	0.088	
28	17.65	16.31	157.742	125.814	0.0599	1.64	52.1	-0.064	
29	17.66	16.34	158.623	125.88	0.059	1.55	51.7	0.024	
30	17.67	16.38	159.961	125.546	0.0565	1.57	54.5	-0.011	
31	17.68	16.425	155.324	124.434	0.0528	1.49	51.5	0.00027	
32	17.69	16.6	159.499	124.284	0.0454	1.57	54.2	0.03	
33	17.7	16.65	161.66	123.826	0.0448	1.49	55.6	0.053	
34	17.71	16.7	161.512	122.943	0.0403	1.46	54.7	0.033	
35	17.72	16.74	156.837	126.113	0.0373	1.48	58.3	-0.094	
36	17.73	16.82	155.332	128.985	0.0369	1.39	52	0.05	
37	17.74	16.87	154.917	130.173	0.0367	1.56	54.3	0.039	
38	17.76	16.95	154.756	133.644	0.0338	1.49	53.2	0.05	
39	17.78	17.065	154.172	133.578	0.0306	1.52	57.8	-0.003	
40	17.8	17.13	154.882	135.562	0.0297	1.4	46.5	0.0073	
41	17.37	15.06	155.182	119.145	0.849	1.74	18.4	0.24	120
42	17.36	14.99	155.699	120.451	0.675	4.4	19.6	0.24	
43	17.35	14.93	156.459	121.652	0.507	4.14	21.3	0.24	
44	17.34	14.87	154.004	124.807	0.363	3.8	24.1	0.24	
45	17.33	14.82	157.647	122.102	0.27	2.97	27.3	0.23	
46	17.32	14.77	160.218	122.193	0.195	2.53	32	0.21	
47	17.31	14.7	160.977	123.331	0.147	2.13	38	0.14	
48	17.3	14.65	161.531	123.832	0.127	1.95	41.5	0.14	
49	17.29	14.61	159.91	128.212	0.116	1.8	45	0.092	
50	17.28	14.58	162.365	122.515	0.108	1.72	47	0.08	
51	17.27	14.53	168.417	122.185	0.104	1.63	49.6	0.032	
52	17.26	14.45	162.518	130.231	0.101	1.61	50.2	0.063	
53	17.25	14.35	157.092	127.323	0.0929	1.58	51.1	0.013	
54	17.24	14.25	155.71	127.576	0.0798	1.53	52.9	0.059	
55	17.23	14.18	155.474	126.383	0.0734	1.55	52.2	0.058	
56	17.22	14.1	150.461	121.354	0.0644	1.44	56	0.031	
57	17.21	14.04	150.831	120.777	0.0584	1.57	51.5	0.034	
58	17.2	13.99	151.61	120.824	0.0568	1.54	52.4	0.064	
59	17.19	13.925	157.879	119.949	0.0538	1.45	53	0.0091	
60	17.18	13.84	158.182	118.754	0.0501	1.53	50.1	0.046	
61	17.17	13.78	158.472	118.439	0.0487	1.38	55.4	-0.078	
62	17.16	13.71	158.205	117.027	476	1.49	51.4	0.033	
63	17.15	13.67	158.006	117.793	0.0465	1.48	51.8	0.063	
64	17.14	13.62	157.719	117.256	0.0442	1.48	51.7	0.066	
65	17.13	13.57	158.364	118.567	0.0433	1.4	54.7	-0.045	
66	17.12	13.53	158.342	119.359	0.0409	1.46	52.4	-0.03	

APPENDIX III

Flowing Case: Experimental Data

Table 6: Summary of the Flowing Fluid Experiments Discussed by Cambern (1999) and in this Thesis.

Experiment Number	Particle Diameter (μm)	Volume Fraction (% by weight)	Flow Rate (%)	Laser/Detector Angle (α) (deg)	Temperature (K)
58	0.107	Very Dilute	0, 50, 100	48	N/A
59	0.107	Very Dilute	0, 50, 100	40, 30, 20	N/A
60	0.204	Very Dilute	0, 50, 100	48	N/A
61	0.204	Very Dilute	0, 50, 100	40, 30, 20	N/A
69	0.107	0.066	25	48	N/A
70	0.107	0.066	25	48	N/A
71	0.107	0.066	50	48	N/A
72	0.107	0.066	50	48	N/A
73	0.107	0.066	75	48	296
74	0.107	0.066	75	48	296
75	0.107	0.066	100	48	296
76	0.107	0.066	100	48	296
77	0.107	0.198	0	48	295
78	0.107	0.198	0	48	295
79	0.107	0.198	25	48	N/A
80	0.107	0.198	25	48	N/A
81	0.107	0.198	75	48	N/A
82	0.107	0.198	75	48	N/A
83	0.107	0.198	100	48	295
84	0.107	0.198	100	48	295
86	0.107	0.198	25	48	295
87	0.107	0.198	25	48	295
90	0.107	0.198	0	40	295
91	0.107	0.198	50	40	295
93	0.107	0.198	0	48	295
94	0.107	0.198	50	48	295
95	0.107	0.198	100	48	295
96	0.107	0.198	0	40	296
97	0.107	0.198	50	40	296
98	0.107	0.198	100	40	296
99	0.107	0.198	0	30	295
100	0.107	0.198	50	30	295
101	0.107	0.198	100	30	295
102	0.107	0.198	0,100	30	295
103	0.098	0.32	0	48	296
104	0.098	0.32	100	48	296
105	0.098	0.86	0	48	296
106	0.098	0.86	100	48	296
108	0.098	0.86	0	30	296
109	0.098	0.86	100	30	296
111	0.203	0.2	0	48	296
112	0.203	0.2	100	48	296
113	0.203	0.2	0	30	296
114	0.203	0.2	100	30	296

Note: Detailed data for Experiments 59, 61, 90, 91, 96-102, 108, 109, 113, 114 appear in Table 7, and detailed data for the remaining experiments are given by Cambern (1999). The experiments not listed were those aborted for various reasons.

Table 7: Detailed Description of Experiments Described in Summary Table 6.

Exp 59 0.107μm PSL; V.F.=Very Dilute; α =40°, 30°, 20°

S.No.	Arm Angles		Count Rate		Cumulant - 2 Fit Data				Flow Rate
	α_L	α_D	Ch 0	Ch 1	Y-Int	Decay Rate	Radius	Norm 2nd Cumulant	
	(deg)		(KHz)		(-)	(/ ms)	(nm)	(-)	
1	40	40	69.559	0	0.938	3.13	55.3	0.0027	0%
2	40	40	0	59.341	0.969	3.09	56.2	0.03	0%
3	40	40	65.122	0	0.935	3.17	54.7	0.022	50%
4	40	40	0	59.303	0.959	3.1	55.9	0.0097	50%
5	40	40	77.609	0	0.951	3.2	54.2	0.018	100%
6	40	40	0	59.294	0.963	3.09	56.1	0.0022	100%
7	30	30	58.1	0	0.932	3.48	55.9	0.018	0%
8	30	30	0	51.561	0.957	3.47	56	0.016	0%
9	30	30	49.237	0	0.926	3.44	56.4	0.083	50%
10	30	30	0	47.207	0.963	3.5	55.5	0.024	50%
11	30	30	36.341	0	0.899	3.5	55.5	0.019	100%
12	30	30	0	46.967	0.962	3.56	54.5	0.032	100%
13	20	20	33.425	0	0.892	3.73	56.6	-0.0014	0%
14	20	20	0	27.541	0.948	3.7	57	0.018	0%
15	20	20	80.474	0	0.945	3.77	56	0.018	50%
16	20	20	0	56.337	0.963	3.78	55.9	0.02	50%
17	20	20	72.596	0	0.943	3.71	55.7	0.029	100%
18	20	20	0	53.566	0.968	3.79	55.7	0.018	100%

Exp 61 0.204 μm PSL; V.F.=Very Dilute; α =40°, 30°, 20°

S.No.	Arm Angles		Count Rate		Cumulant - 2 Fit Data				Flow Rate
	α_L	α_D	Ch 0	Ch 1	Y-Int	Decay Rate	Radius	Norm 2nd Cumulant	
	(deg)		(KHz)		(-)	(/ ms)	(nm)	(-)	
1	40	40	20.057	0	0.917	1.44	118	0.052	0%
2	40	40	0	23.159	0.944	1.45	117	0.053	0%
3	40	40	22.793	0	0.893	1.56	109	0.059	50%
4	40	40	0	25.344	0.945	1.59	107	0.042	50%
5	40	40	20.346	0	0.873	1.54	110	-0.0036	100%
6	40	40	0	24.285	0.939	1.56	109	0.034	100%
7	30	30	18.053	0	0.836	1.74	110	0.041	0%
8	30	30	0	22.278	0.924	1.72	111	0.053	0%
9	30	30	16.648	0	0.842	1.72	111	0.053	50%
10	30	30	0	21.542	0.937	1.71	111	0.045	50%
11	30	30	18.117	0	0.826	1.76	108	0.063	100%
12	30	30	0	21.821	0.925	1.72	110	0.054	100%
13	20	20	23.104	0	0.842	1.84	112	0.035	0%
14	20	20	0	23.575	0.914	1.91	109	0.036	0%
15	20	20	27.643	0	0.844	1.96	106	0.051	50%
16	20	20	0	23.771	0.909	1.91	108	0.025	50%
17	20	20	22.319	0	0.832	1.88	110	0.055	100%
18	20	20	0	23.593	0.921	1.91	108	0.066	100%

Exp 90 0.107 µm PSL; V.F.=0.198%; α =40°, Flow Rate = 0%

Front Tilt = 18.12 divs Side Translation = 12.27 divs

S.No.	op Fiber Mic. Rdgs.		Count Rate		Cumulant - 2 Fit Data				Duration
	Rear Tilt	Front Translation	Ch 0	Ch 1	Y-Int	Decay Rate	Radius	Norm 2nd Cumulant	
	(divs)		(KHz)		(-)	(/ ms)	(nm)	(-)	(s)
1	16.04	11.8	91.387	98.273	0.844	3.67	47	0.061	120
2	16.05	11.82	90.585	98.96	0.832	3.68	46.9	0.051	
3	16.06	11.85	90.389	99.438	0.807	3.63	47.5	0.06	
4	16.07	11.89	90.227	98.182	0.732	3.67	47	0.062	
5	16.08	11.93	89.913	99.523	0.653	3.65	47.2	0.059	
6	16.09	11.98	90.256	98.764	0.556	3.6	47.9	0.055	
7	16.1	12.02	89.976	98.218	0.457	3.59	48.1	0.05	120
8	16.11	12.05	90.02	98.167	0.377	3.58	48.2	0.044	240
9	16.12	12.09	89.948	99.154	0.29	3.53	48.9	0.034	300
10	16.13	12.14	89.869	97.977	0.194	3.52	49.1	0.016	
11	16.14	12.18	89.154	98.149	0.147	3.51	49.2	0.048	360
12	16.15	12.2	89.263	100.306	0.113	3.45	50.3	0.026	420
13	16.16	12.24	89.4	99.646	0.0757	3.42	50.5	-0.00018	480
14	16.17	12.28	89.643	99.93	0.0457	3.39	50.9	0.024	
15	16.18	12.32	89.573	100.117	0.0294	3.31	52.2	0.041	

Exp 91 0.107 µm PSL; V.F.=0.198%; α =40°, Flow Rate = 50%

Front Tilt = 18.12 divs Side Translation = 12.27 divs

S.No.	Top Fiber Mic. Rdgs.		Count Rate		Cumulant - 2 Fit Data				Duration
	Rear Tilt	Front Translation	Ch 0	Ch 1	Y-Int	Decay Rate	Radius	Norm 2nd Cumulant	
	(divs)		(KHz)		(-)	(/ ms)	(nm)	(-)	(s)
1	16.04	11.8	88.38	94.269	0.849	4.3	40.1	0.088	120
2	16.05	11.84	88.679	93.482	0.824	4.29	40.3	0.096	
3	16.06	11.87	88.644	93.48	0.778	4.26	40.5	0.092	
4	16.07	11.91	88.872	94.558	0.721	4.22	40.9	0.089	
5	16.08	11.95	88.57	93.961	0.631	4.22	40.9	0.083	
6	16.09	11.98	87.731	95.747	0.543	4.14	41.7	0.079	
7	16.1	12.01	88.571	94.752	0.453	4.11	42	0.076	
8	16.11	12.05	88.674	95.089	0.37	4.08	42.3	0.077	180
9	16.12	12.09	87.193	94.433	0.276	4.04	42.7	0.079	240
10	16.13	12.14	86.931	94.26	0.195	3.98	43.3	0.045	
11	16.14	12.17	86.593	93.987	0.142	3.94	43.7	0.066	300
12	16.15	12.21	86.51	94.238	0.101	3.81	45.4	0.018	
13	16.16	12.25	86.203	94.87	0.0664	3.71	46.6	-0.0084	480
14	16.17	12.29	86.075	93.987	0.0408	4.01	43.1	0.11	480

Exp 96 0.107 μm PSL; V.F.=0.198%; α =40°, Flow Rate = 0%
Front Tilt = 18.10 divs Side Translation = 12.28 divs

S.No.	Top Fiber Mic. Rdgs.		Count Rate		Cumulant - 2 Fit Data				Dur
	Rear Tilt	Front Translation	Ch 0	Ch 1	Y-Int	Decay Rate	Radius	Norm 2nd Cumulant	
	(divs)		(KHz)		(-)	(/ ms)	(nm)	(-)	(s)
1	16.04	11.8	116.694	147.202	0.9	3.58	48.2	0.045	120s
2	16.06	11.82	116.548	146.043	0.892	3.55	48.6	0.037	
3	16.08	11.95	116.211	146.35	0.652	3.57	48.4	0.046	
4	16.1	12.04	116.239	144.96	0.799	3.45	50	0.02	
5	16.12	12.11	116.627	148.563	0.756	3.41	50.6	0.031	
6	16.14	12.2	116.262	147.29	0.696	3.4	50.7	0.024	
7	16.16	12.28	116.468	146.504	0.65	3.34	51.7	0.02	
8	16.18	12.36	116.051	144.958	0.614	3.31	52.1	0.024	
9	16.2	12.44	115.942	144.47	0.591	3.26	52.9	0.0061	
10	16.22	12.51	116.613	146.305	0.557	3.28	52.6	0.021	
11	16.24	12.58	116.553	146.359	0.528	3.26	53	0.0087	
12	16.26	12.66	116.195	144.297	0.501	3.26	52.9	0.0076	
13	16.28	12.74	116.044	144.882	0.471	3.24	53.2	-0.0074	
14	16.3	12.82	116.502	145.549	0.446	3.24	53.2	0.014	
15	16.32	12.89	116.149	146.209	0.419	3.29	52.5	0.025	
16	16.34	12.98	116.192	145.98	0.396	3.23	53.4	-0.011	
17	16.36	13.05	116.457	146.748	0.374	3.27	52.8	0.025	
18	16.38	13.13	116.717	144.933	0.347	3.22	53.7	0.017	
19	16.4	13.21	116.514	144.686	0.326	3.21	53.8	0.011	
20	16.42	13.28	116.31	147.681	0.304	3.26	52.9	0.017	
21	16.44	13.35	116.687	144.598	0.288	3.18	54.3	0.0022	
22	16.46	13.43	116.989	143.801	0.267	3.29	52.4	0.031	
23	16.48	13.49	117.08	145.719	0.251	3.19	54.1	-0.012	
24	16.5	13.57	116.931	143.412	0.233	3.11	55.5	-0.02	
25	16.52	13.63	117.135	147.981	0.218	3.3	52.3	0.03	
26	16.54	13.71	118.904	150.445	0.204	3.14	55	-0.0081	
27	16.56	13.8	116.935	144.547	0.187	3.23	53.5	0.017	
28	16.58	13.86	116.795	145.675	0.174	3.22	53.6	0.0063	120s
29	16.6	13.93	117.037	145.878	0.164	3.2	53.9	0.051	180s
30	16.64	14.09	117.184	143.161	0.139	3.18	54.2	0.0065	180s
31	16.68	14.23	116.708	145.848	0.114	3.21	53.8	-0.014	
32	16.72	14.4	115.402	138.805	0.099	3.19	54.1	0.044	

Exp 97 0.107 μm PSL; V.F.=0.198%; α =40°, Flow Rate = 50%
Front Tilt = 18.10 divs Side Translation = 12.27 divs

S.No.	Top Fiber Mic. Rdgs.		Count Rate		Cumulant - 2 Fit Data				Duration
	Rear Tilt	Front Translation	Ch 0	Ch 1	Y-Int	Decay Rate	Radius	Norm 2nd Cumulant	
	(divs)		(KHz)		(-)	(/ ms)	(nm)	(-)	(s)
1	16.04	11.8	106.135	141.687	0.908	3.9	44.3	0.092	120
2	16.06	11.89	104.616	138.14	0.88	3.85	44.9	0.091	
3	16.08	11.97	106.871	139.956	0.851	3.68	46.2	0.061	
4	16.1	12.06	105.716	139.912	0.802	3.59	47.3	0.073	
5	16.12	12.14	104.719	142.615	0.752	3.44	49.3	0.049	
6	16.14	12.22	104.662	141.713	0.702	3.35	50.7	0.034	
7	16.16	12.29	105.87	139.364	0.664	3.28	51.8	0.033	
8	16.18	12.36	106.982	141.713	0.636	3.25	52.2	0.035	
9	16.2	12.44	106.552	140.4	0.602	3.21	52.9	0.037	
10	16.22	12.5	105.862	141.681	0.579	3.18	53.4	0.029	
11	16.24	12.57	104.834	141.328	0.548	3.16	53.7	0.023	
12	16.26	12.64	104.665	142.516	0.525	3.17	53.6	0.035	
13	16.28	12.72	105.287	143.094	0.498	3.13	54.2	0.021	
14	16.3	12.8	106.159	144.291	0.465	3.12	54.5	0.0062	
15	16.32	12.91	106.944	139.858	0.43	3.17	53.5	0.027	
16	16.34	12.97	107.136	142.655	0.409	3.17	53.6	0.02	
17	16.36	13.05	106.892	140.825	0.387	3.14	54.2	0.023	
18	16.38	13.12	107.011	141.086	0.362	3.17	53.6	0.044	
19	16.4	13.19	106.534	140.957	0.34	3.18	53.3	0.094	
20	16.42	13.25	106.476	140.722	0.319	3.1	54.8	0.019	
21	16.44	13.32	106.03	139.667	0.304	3.09	55	0.017	
22	16.46	13.39	104.808	139.582	0.28	3.17	53.6	0.052	
23	16.48	13.48	104.978	139.443	0.263	3.14	54.1	0.037	
24	16.5	13.55	104.45	138.734	0.245	3.17	53.6	0.026	
25	16.52	13.62	105.566	138.635	0.229	3.17	53.6	-0.06	
26	16.54	13.69	106.194	138.194	0.218	3.15	54	0.032	
27	16.56	13.75	106.383	136.691	0.205	3.21	52.8	0.065	120
28	16.58	13.84	106.81	135.636	0.189	3.18	53.5	0.054	180
29	16.6	13.9	106.874	135.013	0.174	3.16	53.7	0.051	
30	16.62	13.96	106.594	133.664	0.165	3.08	55.2	0.032	
31	16.64	14.03	105.636	133.969	0.152	3.11	54.6	-0.029	
32	16.68	14.2	105.028	138.606	0.128	3.13	54.2	0.028	240
33	16.72	14.36	104.447	140.442	0.108	3.24	52.5	0.07	
34	16.76	14.5	104.685	142.572	0.0921	3.13	54.3	-0.019	300

Exp 98 0.107 μm PSL; V.F.=0.198%; α =40°, Flow Rate = 100%
Front Tilt = 18.10 divs Side Translation = 12.27 divs

S.No.	Top Fiber Mic. Rdgs.		Count Rate		Cumulant - 2 Fit Data				Dur
	Rear Tilt	Front Translation	Ch 0	Ch 1	Y-Int	Decay Rate	Radius	Norm 2nd Cumulant	
	(divs)		(KHz)		(-)	(/ ms)	(nm)	(-)	(s)
1	16.04	11.8	104.365	138.133	0.911	4.66	36.5	0.17	120
2	16.06	11.89	104.371	137.725	0.896	4.54	37.4	0.17	
3	16.08	11.95	104.482	139.608	0.87	4.33	39.2	0.15	
4	16.1	12.03	104.346	141.807	0.822	4.1	41.5	0.12	
5	16.12	12.15	104.424	137.255	0.75	3.78	44.9	0.1	
6	16.14	12.21	104.297	140.075	0.708	3.61	47.1	0.069	
7	16.16	21.28	104.616	140.798	0.672	3.5	48.5	0.049	
8	16.18	12.37	104.189	139.604	0.628	3.34	50	0.035	
9	16.2	12.43	104.739	140.848	0.601	3.33	51.1	0.025	
10	16.22	12.5	103.0383	141.175	0.568	3.3	51.4	0.029	
11	16.24	12.57	104.403	141.33	0.535	3.24	52.4	0.02	
12	16.26	12.64	105.147	142.125	0.508	3.25	52.2	0.032	
13	16.28	12.74	105.512	140.435	0.464	3.23	52.5	0.014	
14	16.3	12.82	105.242	140.902	0.437	3.18	53.4	0.0039	
15	16.32	12.9	105.639	141.148	0.407	3.22	52.8	0.0097	
16	16.34	12.97	105.22	141.595	0.383	3.15	53.9	0.018	
17	16.36	13.04	105.64	140.162	0.356	3.2	53	0.016	
18	16.38	13.1	105.893	139.553	0.338	3.2	53	0.035	
19	16.4	13.19	105.784	138.682	0.307	3.21	53	0.032	
20	16.42	13.27	105.414	138.154	0.286	3.14	54.2	0.009	
21	16.44	13.34	105.823	137.828	0.266	3.14	54	-0.0029	
22	16.46	13.41	105.832	138.178	0.246	3.21	52.9	0.012	
23	16.48	13.47	103.486	131.984	0.233	3.12	54.4	-0.0009	
24	16.5	13.55	105.356	138.972	0.213	3.16	53.8	0.038	120
25	16.52	13.61	105.062	138.772	0.197	3.07	55.3	0.000083	180
26	16.54	13.7	105.114	138.684	0.181	3.14	54.1	0.0062	
27	16.56	13.76	104.137	137.657	0.168	3.07	55.4	-0.022	
28	16.58	13.83	104.456	135.691	0.154	3.11	54.6	0.028	
29	16.6	13.92	104.134	135.464	0.143	3.14	54	0.014	240
30	16.64	14.04	103.598	134.734	0.119	3.25	52.3	0.059	300
31	16.68	14.2	103.508	137.216	0.0987	3.18	53.5	0.043	
32	16.72	14.34	103.598	139.308	0.0826	3.08	55.2	0.082	
33	16.76	14.52	103.846	140.846	0.0675	3.18	53.4	0.065	

Exp 99 0.107 μm PSL; V.F.=0.198%; α =30°, Flow Rate = 0%

Front Tilt = 18.10 divs Side Translation = 12.31 divs

S.No.	Top Fiber Mic. Rdgs.		Count Rate		Cumulant - 2 Fit Data				Dur
	Rear Tilt	Front Translation	Ch 0	Ch 1	Y-Int	Decay Rate	Radius	Norm 2nd Cumulant	
	(divs)		(KHz)		(-)	(/ ms)	(nm)	(-)	(s)
1	16.05	11.78	104.365	129.735	0.893	3.92	50	0.032	120
2	16.05	11.78	0	129.89	0.971	3.92	50.1	0.035	0
3	16.05	11.78	105.33	0	0.948	3.97	49.5	0.024	0
4	16.05	11.78	105.624	131.476	0.896	4.16	47.1	0.021	50
5	16.05	11.78	104.291	132.198	0.902	4.98	39.4	0.13	100
6	16.05	11.78	104.383	129.786	0.894	3.88	50.6	0.028	120
7	16.07	11.85	105.538	131.719	0.877	3.91	50.2	0.029	
8	16.09	11.99	105.15	130.096	0.812	3.85	51	0.03	
9	16.11	12.06	105.287	130.784	0.75	3.82	51.4	0.024	
10	16.13	12.16	105.631	130.85	0.684	3.77	52	0.021	
11	16.15	12.23	105.855	130.394	0.633	3.75	52.4	0.027	
12	16.17	12.31	105.977	130.65	0.582	3.73	52.6	0.022	
13	16.19	12.38	106.051	131.521	0.537	3.73	52.6	0.021	
14	16.21	12.45	106.226	131.732	0.495	3.66	53.6	-0.0027	
15	16.23	12.53	105.314	132.091	0.451	3.7	53.1	0.018	
16	16.25	12.61	105.667	130.232	0.412	3.63	54	0.0019	
17	16.27	12.68	104.948	130.94	0.371	3.75	52.3	0.029	
18	16.29	12.76	104.932	130.308	0.337	3.67	53.5	-0.01	
19	16.31	12.84	100.365	131.693	0.301	3.65	53.8	-0.0044	
20	16.33	12.92	105.092	131.476	0.268	3.59	54.7	-0.038	
21	16.35	13	105.579	130.048	0.237	3.63	54.1	0.0087	
22	16.37	13.08	105.373	130.143	0.211	3.6	54.6	0.025	
23	16.39	13.16	104.325	130.938	0.184	3.64	53.9	0.019	180
24	16.43	13.3	104.377	131.21	0.144	3.71	52.8	0.0049	
25	16.47	13.44	104.417	131.11	0.11	3.71	52.9	0.058	240
26	16.51	13.59	104.55	130.285	0.085	3.8	51.6	0.038	300
27	16.55	13.74	104.667	131.42	0.062	3.67	53.5	-0.08	300

Exp 100 0.107 μm PSL; V.F.=0.198%; α =30°, Flow Rate = 50%
Front Tilt = 18.10 divs Side Translation = 12.31 divs

S.No	Top Fiber Mic. Rdgs.		Count Rate		Cumulant - 2 Fit Data				Dur
	Rear Tilt	Front Translation	Ch 0	Ch 1	Y-Int	Decay Rate	Radius	Norm 2nd Cumulant	
	(divs)		(KHz)		(-)	(/ ms)	(nm)	(-)	(s)
1	16.05	11.78	105.4	127.666	0.894	4.19	46.8	0.028	
2	16.07	11.87	106.77	130.643	0.877	4.14	47.5	0.027	120
3	16.09	11.97	108.25	130.113	0.83	4.05	48.4	0.037	
4	16.11	12.06	107.36	129.342	0.758	3.9	50.3	0.0045	
5	16.13	12.16	105.85	130.285	0.681	3.81	51.5	-0.014	
6	16.15	12.23	105.67	128.392	0.628	3.79	51.8	0.011	
7	16.17	12.3	105.6	130.337	0.587	3.69	53.2	-0.061	
8	16.19	12.38	106.07	129.652	0.539	3.7	53	0.014	
9	16.21	12.45	106.98	128.943	0.496	3.65	53.8	-0.0034	
10	16.23	12.53	107.44	130.135	0.449	3.62	54.2	-0.022	
11	16.25	12.6	107.89	129.314	0.413	3.67	53.5	-0.003	
12	16.27	12.68	108.18	129.143	0.372	3.69	53.2	0.02	
13	16.29	12.76	107.68	132.325	0.334	3.68	53.3	0.011	
14	16.31	12.85	107.77	130.038	0.299	3.67	53.4	-0.013	
15	16.33	12.93	107.52	129.283	0.268	3.67	53.6	-0.0029	
16	16.35	13	102.2	128.038	0.238	3.64	54	0.00074	
17	16.38	13.11	106.62	130.78	0.202	3.68	53.3	0.0058	180
18	16.41	13.22	106.04	130.261	0.172	3.65	53.7	-0.0053	
19	16.44	13.33	105.79	127.373	0.142	3.66	53.7	0.031	
20	16.47	13.42	106.12	129.628	0.121	3.59	54.7	0.0043	240
21	16.5	13.53	106.63	129.529	0.103	3.61	54.4	0.035	
22	16.54	13.67	107.71	129.561	0.08	3.55	55.3	-0.036	300
23	16.58	13.8	108.18	131.156	0.062	3.73	52.6	0.057	
24	16.62	13.96	108.52	129.898	0.048	3.68	53.4	0.0083	

Exp 101 0.107 μm PSL; V.F.=0.198%; α =30°, Flow Rate = 100%
Front Tilt = 18.10 divs Side Translation = 12.31 divs

S.No.	Top Fiber Mic. Rdgs.		Count Rate		Cumulant - 2 Fit Data				Dur
	Rear Tilt	Front Translation	Ch 0	Ch 1	Y-Int	Decay Rate	Radius	Norm 2nd Cumulant	
	(divs)		(KHz)		(-)	(/ ms)	(nm)	(-)	(s)
1	16.05	11.78	107.627	133.132	0.895	4.98	39.4	0.12	120
2	16.07	11.84	107.58	132.098	0.884	4.91	40	0.12	
3	16.09	11.91	107.059	132.738	0.853	4.75	41.3	0.11	
4	16.11	12.04	105.982	132.458	0.775	4.46	44	0.079	
5	16.13	12.12	106.103	131.873	0.697	4.2	46.7	0.04	
6	16.15	12.21	105.739	132.476	0.646	3.99	49.2	0.011	
7	16.17	12.29	105.558	131.627	0.584	3.84	51.1	-0.0035	
8	16.19	12.36	106.617	132.053	0.542	3.81	51.5	0.01	
9	16.21	12.43	105.409	131.463	0.501	3.75	52.4	-0.011	
10	16.23	12.51	105.398	132.026	0.455	3.7	53	-0.018	
11	16.25	12.58	106.308	134.244	0.416	3.67	53.5	-0.0061	
12	16.27	12.66	105.275	131.596	0.38	3.57	55	-0.01	
13	16.29	12.74	105.485	131.015	0.34	3.57	55	-0.018	
14	16.31	12.82	105.478	131.451	0.31	3.67	53.5	-0.0099	
15	16.33	12.9	105.576	131.74	0.275	3.66	53.6	0.0033	
16	16.35	12.97	105.705	127.666	0.246	3.64	53.9	-0.0047	
17	16.38	13.08	96.54	126.662	0.207	3.67	53.5	0.023	180
18	16.41	13.19	99.066	128.574	0.176	3.68	53.4	-0.0043	
19	16.44	13.29	99.119	127.862	0.147	3.7	53	0.014	240
20	16.47	13.39	99.18	127.455	0.123	3.45	56.8	0.052	
21	16.5	13.5	99.354	127.018	0.101	3.52	55.7	-0.00018	300
22	16.54	13.66	99.533	128.654	0.0787	3.74	52.5	0.052	
23	16.58	13.8	99.221	130.399	0.0614	3.51	56	-0.0017	
24	16.62	13.95	99.047	129.052	0.0474	3.87	50.8	0.11	

Exp 108 0.098 μm PSL; V.F.=0.86%; α =30°, Flow Rate = 0%
Front Tilt = 18.09 divs Side Translation = 12.30 divs

S.No.	Top Fiber Mic. Rdgs.		Count Rate		Cumulant - 2 Fit Data				Dur
	Rear Tilt	Front Translation	Ch 0	Ch 1	Y-Int	Decay Rate	Radius	Norm 2nd Cumulant	
	(divs)		(KHz)		(-)	(/ ms)	(nm)	(-)	(s)
1	16.03	11.72	145.411	200.579	0.9	4.51	43.6	0.08	120
2	16.05	11.8	140.552	198.264	0.858	4.44	44.2	0.072	
3	16.07	11.87	140.752	201.75	0.801	4.37	44.9	0.067	
4	16.09	11.95	140.385	198.798	0.728	4.28	45.9	0.053	
5	16.11	12.03	140.593	197.789	0.652	4.18	47	0.046	
6	16.13	12.11	140.416	199.039	0.579	4.11	47.8	0.033	
7	16.15	12.17	140.738	202.634	0.536	4.09	48	0.038	
8	16.17	12.25	141.567	202.411	0.481	4.06	48.3	0.031	
9	16.19	12.32	141.213	200.842	0.435	3.97	49.4	0.021	
10	16.21	12.34	141.93	200.919	0.394	3.95	49.7	0.035	
11	16.23	12.48	142.409	199.881	0.353	3.97	49.5	0.04	
12	16.25	12.55	134.251	186	0.318	3.97	49.5	0.021	
13	16.27	12.62	142.038	197.197	0.281	3.94	49.8	0.049	
14	16.29	12.72	142.75	192.989	0.248	3.88	50.6	0.035	
15	16.31	12.8	141.429	191.353	0.218	3.91	50.2	0.017	180
16	16.33	12.87	137.762	195.892	0.196	3.86	50.8	0.018	
17	16.35	12.97	140.882	192.268	0.167	4	49	0.04	
18	16.37	13.03	142.471	196.235	0.152	3.88	50.5	0.0053	240
19	16.39	13.11	142.448	193.509	0.131	4.05	48.5	0.052	
20	16.42	13.23	142.213	190.68	0.107	3.97	49.4	-0.017	
21	16.45	13.32	142.914	193.791	0.0907	3.85	51	0.024	300
22	16.48	13.42	143.285	192.085	0.0751	3.94	49.8	0.031	
23	16.52	13.54	142.965	194.062	0.0602	4.03	48.7	0.11	

Exp 109 0.098 μm PSL; V.F.=0.86%; α =30°, Flow Rate = 100%

Front Tilt = 18.09 divs Side Translation = 12.30 divs

S.No.	Top Fiber Mic. Rdgs.		Count Rate		Cumulant - 2 Fit Data				Dur
	Rear Tilt	Front Translation	Ch 0	Ch 1	Y-Int	Decay Rate	Radius	Norm 2nd Cumulant	
	(divs)		(KHz)		(-)	(/ ms)	(nm)	(-)	(s)
1	16.03	11.72	139.655	195.785	0.909	5.41	36.3	0.091	120
2	16.05	11.8	140.851	194.8	0.869	5.3	37	0.094	
3	16.07	11.87	141.027	202.947	0.809	5.09	38.6	0.085	
4	16.09	11.95	139067	193.602	0.744	4.81	40.8	0.051	
5	16.11	12.02	136.065	187.59	0.67	4.66	42.2	0.057	
6	16.13	12.1	140.567	195.351	0.603	4.44	44.2	0.047	
7	16.15	12.18	139.798	193.49	0.54	4.33	45.4	0.22	
8	16.17	12.25	146.463	192.697	0.443	4.23	46.4	0.032	
9	16.19	12.32	140.213	196.154	0.432	4.12	47.6	0.01	
10	16.21	12.39	140.565	194.628	0.413	4.12	47.7	0.0042	
11	16.23	12.47	140.25	194.017	0.374	4.03	48.7	0.049	
12	16.25	12.54	140.491	195.49	0.341	4.03	48.7	0.011	
13	16.27	12.62	141.058	201.588	0.31	4	49.1	-0.0027	
14	16.29	12.7	140.18	195.891	0.275	4.01	49	0.019	
15	16.31	12.74	139.995	195.636	0.242	3.93	49.9	0.026	180
16	16.33	12.88	139.248	195.17	0.212	4.07	48.2	0.0066	
17	16.35	12.95	140.526	195.463	0.196	3.88	50.6	0.012	
18	16.37	13.04	141.181	194.679	0.172	3.87	50.7	0.0069	
19	16.39	13.12	141.07	193.645	0.152	3.86	50.9	0.014	
20	16.42	13.24	141.039	194.63	0.127	3.88	50.6	0.059	240
21	16.45	13.34	141.75	194.969	0.108	4.03	48.7	0.0064	
22	16.48	13.45	142.727	192.53	0.0913	3.79	51.8	-0.041	300
23	16.51	13.56	143.085	192.021	0.0789	3.61	54.4	-0.041	
24	16.03	11.72	139.912	0	0.968	5.69	34.5	0.12	120
25	16.03	11.72	0	200.886	0.967	5.17	38	0.084	

Exp 113 0.203 μm PSL; V.F.=0.20%; α=30°, Flow Rate = 0%
Front Tilt = 18.10 divs Side Translation = 12.34 divs

S.No.	Top Fiber Mic. Rdgs.		Count Rate		Cumulant - 2 Fit Data				Dur
	Rear Tilt	Front Translation	Ch 0	Ch 1	Y-Int	Decay Rate	Radius	Norm 2nd Cumulant	
	(divs)		(KHz)		(-)	(/ ms)	(nm)	(-)	(s)
1	16.03	11.71	98.199	0	0.952	2.11	93	0.063	120
2	16.03	11.71	0	134.959	0.966	2.04	96	0.048	
3	16.03	11.69	98.345	134.158	0.898	2.05	95.6	0.047	
4	16.05	11.76	98.762	135.18	0.865	2.04	96	0.051	
5	16.07	11.83	98.528	134.658	0.806	2.01	97.5	0.052	
6	16.09	11.9	98.404	134.829	0.731	2	98.1	0.031	
7	16.11	11.98	98.823	134.766	0.659	1.96	100	0.037	
8	16.13	12.11	98.976	134.699	0.552	1.9	104	0.033	
9	16.15	12.18	99.142	133.374	0.499	1.9	104	0.027	
10	16.17	12.25	101.175	138.09	0.45	1.89	104	0.02	
11	16.19	12.29	98.633	133.836	0.422	1.88	104	0.0096	
12	16.21	12.37	99.037	133.843	0.393	1.86	106	0.029	
13	16.21	12.33	98.834	127.724	0.392	1.88	104	0.021	
14	16.23	12.45	99.226	133.873	0.356	1.84	107	0.015	
15	16.23	12.41	98.744	127.555	0.359	1.89	104	0.04	
16	16.25	12.49	96.169	131.135	0.332	1.88	104	0.035	
17	16.27	12.57	99.294	129.602	0.305	1.85	106	0.053	
18	16.27	12.57	99.361	128.424	0.305	1.84	107	0.0047	180
19	16.29	12.66	99.269	132.486	0.282	1.87	105	0.039	
20	16.29	12.64	99.161	128.83	0.286	1.83	107	0.014	
21	16.32	12.85	99.479	132.665	0.247	1.86	106	0.026	
22	16.32	12.87	99.048	126.073	0.234	1.84	107	-0.0026	
23	16.35	12.97	99.429	124.82	0.218	1.86	106	0.024	240
24	16.38	13.08	99.577	129.688	0.194	1.89	104	0.033	
25	16.41	13.19	99.778	131.222	0.177	1.81	108	0.0038	
26	16.41	13.2	99.714	129.101	0.173	1.83	107	-0.019	
27	16.45	13.34	99.663	129.494	0.152	1.83	107	0.0024	
28	16.47	13.41	99.743	129.418	0.143	1.8	109	-0.0092	
29	16.5	13.5	99.505	129.584	0.13	1.81	109	0.011	300
30	16.53	13.61	99.735	128.922	0.113	1.82	108	-0.082	120
31	16.53	13.61	99.496	128.056	0.118	1.81	108	0.00082	240
32	16.56	13.71	99.242	129.166	0.108	1.77	99.9	0.058	240
33	16.59	13.8	99.344	128.998	0.0974	1.78	111	-0.04	240

Exp 114 0.203 μm PSL; V.F.=0.20%; α=30°, Flow Rate =100%
Front Tilt = 18.10 divs Side Translation = 12.34 divs

S.No.	Top Fiber Mic. Rdgs.		Count Rate		Cumulant - 2 Fit Data				Dur
	Rear Tilt	Front Translation	Ch 0	Ch 1	Y-Int	Decay Rate	Radius	Norm 2nd Cumulant	
	(divs)		(KHz)		(-)	(/ ms)	(nm)	(-)	(s)
1	16.03	11.71	98.401	0	0.965	3.51	55.9	0.18	120
2	16.03	11.71	0	134.06	0.981	3.02	65	0.16	
3	16.03	11.71	98.481	134.44	0.909	3.07	63.9	0.16	
4	16.05	11.79	98.224	130.57	0.854	2.96	66.3	0.15	
5	16.07	11.88	98.401	132.25	0.777	2.77	70.9	0.14	
6	16.09	11.95	98.107	133.76	0.696	2.58	76.1	0.11	
7	16.11	12.04	97.907	133.35	0.593	2.36	83.2	0.065	
8	16.13	12.12	98.106	135.54	0.524	2.32	88.9	0.045	
9	16.15	12.19	98.147	135.98	0.473	2.1	93.3	0.015	
10	16.17	12.27	95.904	131.14	0.429	2.02	97.4	0.026	
11	16.19	12.34	98.341	135.49	0.39	1.96	100	-0.0088	
12	16.21	12.42	97.826	133.88	0.354	1.89	104	-0.048	
13	16.23	12.5	98.046	132.07	0.32	1.94	101	0.017	
14	16.25	12.56	97.89	134.39	0.296	1.91	103	-0.00061	180
15	16.27	12.61	98.252	135.29	0.28	1.85	106	-0.039	
16	16.29	12.72	98.232	134.89	0.252	1.84	107	-0.042	240
17	16.31	12.84	98.027	132.81	0.225	1.84	107	-0.023	
18	16.33	12.87	97.819	133.26	0.217	1.81	108	0.002	
19	16.35	12.95	97.24	130.73	0.194	1.87	105	-0.006	
20	16.37	13.05	96.005	128.47	0.181	1.85	106	-0.011	300
21	16.39	13.12	95.431	124.69	0.17	1.8	109	-0.05	
22	16.42	13.2	90.749	119.58	0.144	1.82	108	-0.0098	

APPENDIX IV

Flowing Case: Plots of Y-intercept Versus Tilt Angle Mapping

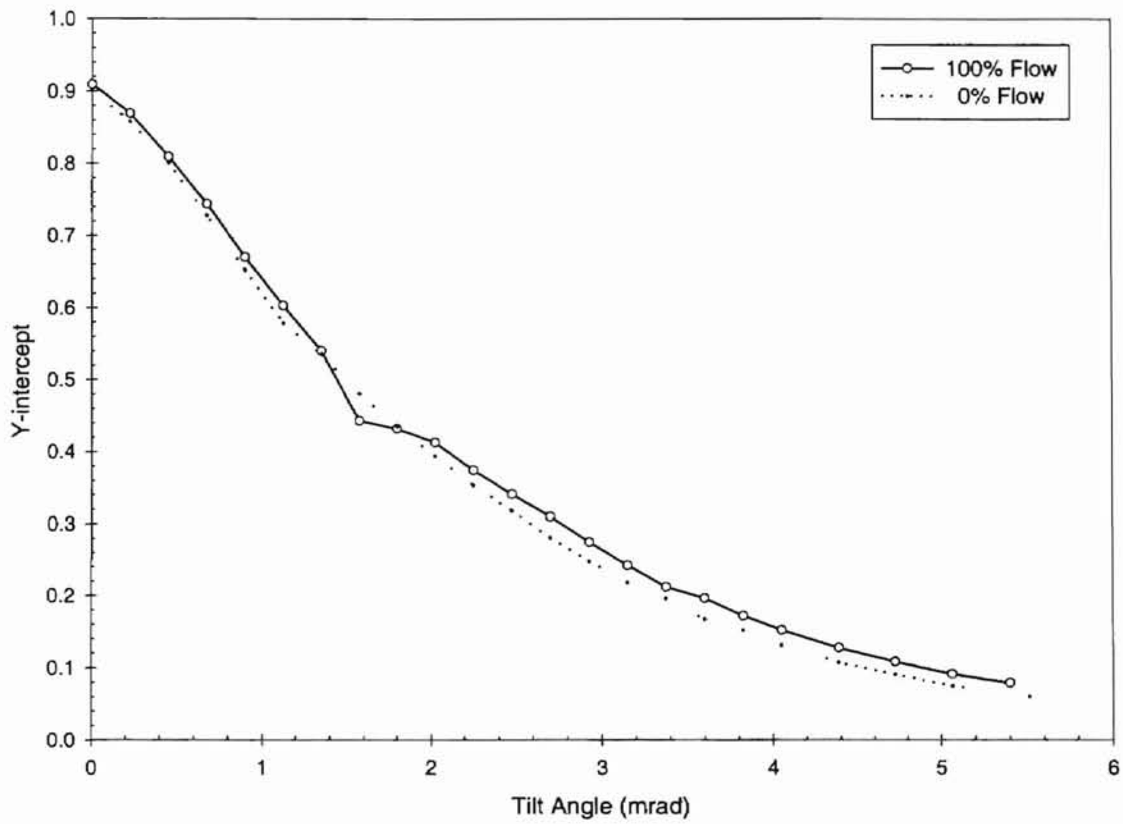

Figure 47: Y-intercept versus tilt angle mapping for 0.098 μm particles for the flowing case. The volume fraction is 0.86 percent. The angle α is 30° (corresponding scattering angle is 136°). Two different flow rates are compared here, viz., 0% and 100% flow. Data corresponds to experiments 108 and 109.

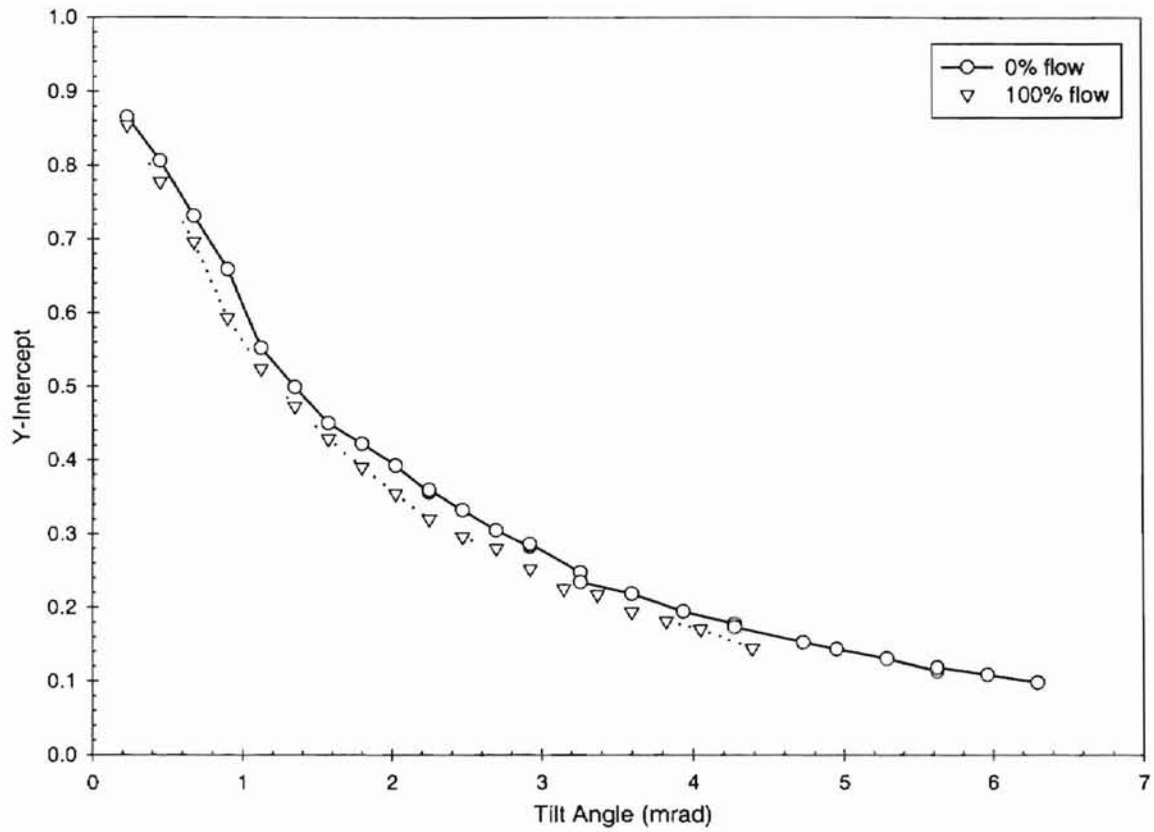

Figure 48: Y-intercept versus tilt angle mapping for 0.203 μm particles for the flowing case. The volume fraction is 0.20 percent. The angle α is 30° (corresponding scattering angle is 136°). Two different flow rates are compared here, viz., 0% and 100% flow. Data corresponds to experiments 113 and 114.

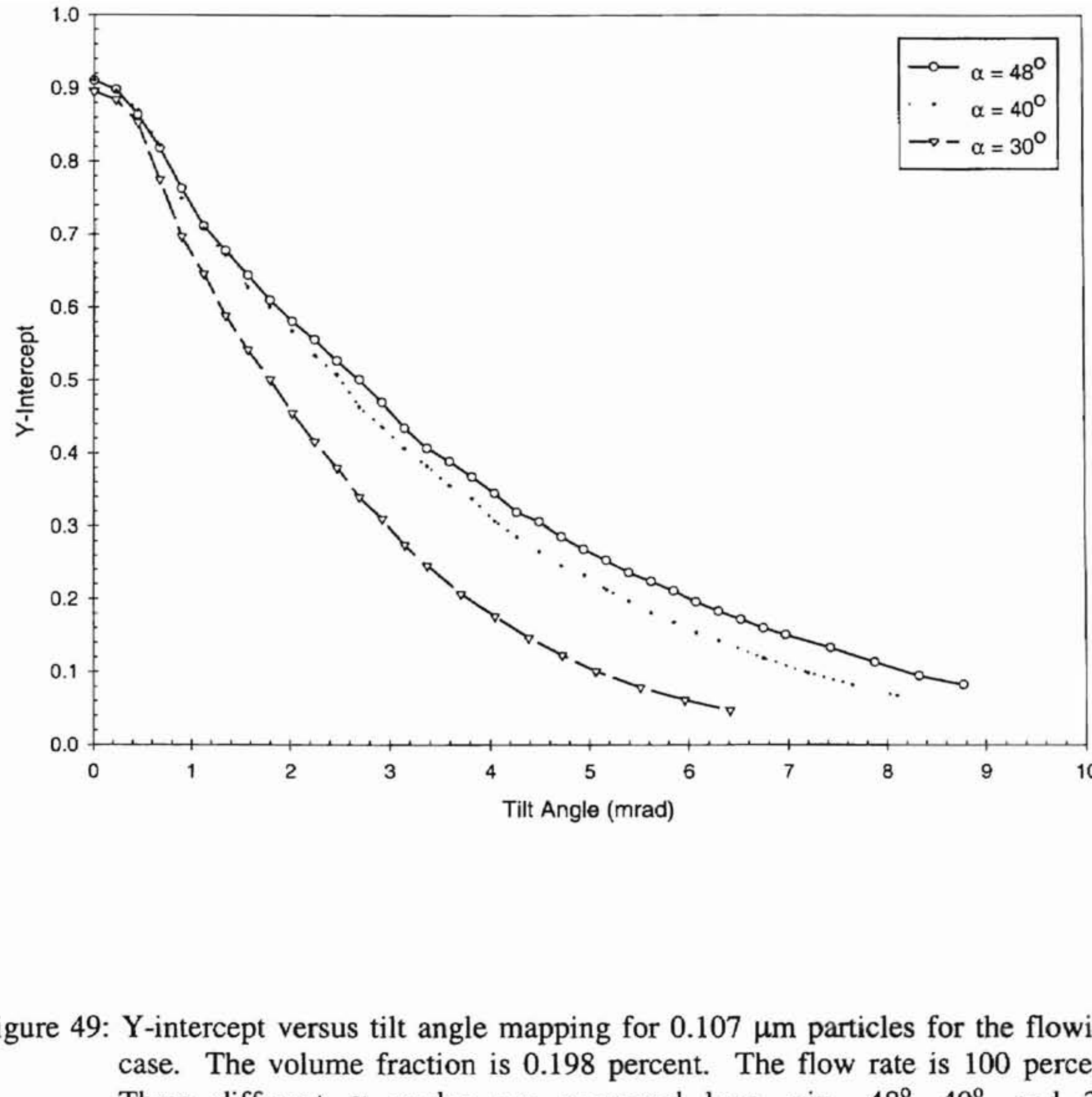

Figure 49: Y-intercept versus tilt angle mapping for 0.107 μm particles for the flowing case. The volume fraction is 0.198 percent. The flow rate is 100 percent. Three different α angles are compared here, viz., 48°, 40°, and 30° (corresponding scattering angles are 112°, 122°, and 135°). Data corresponds to experiments 95, 98, and 101.

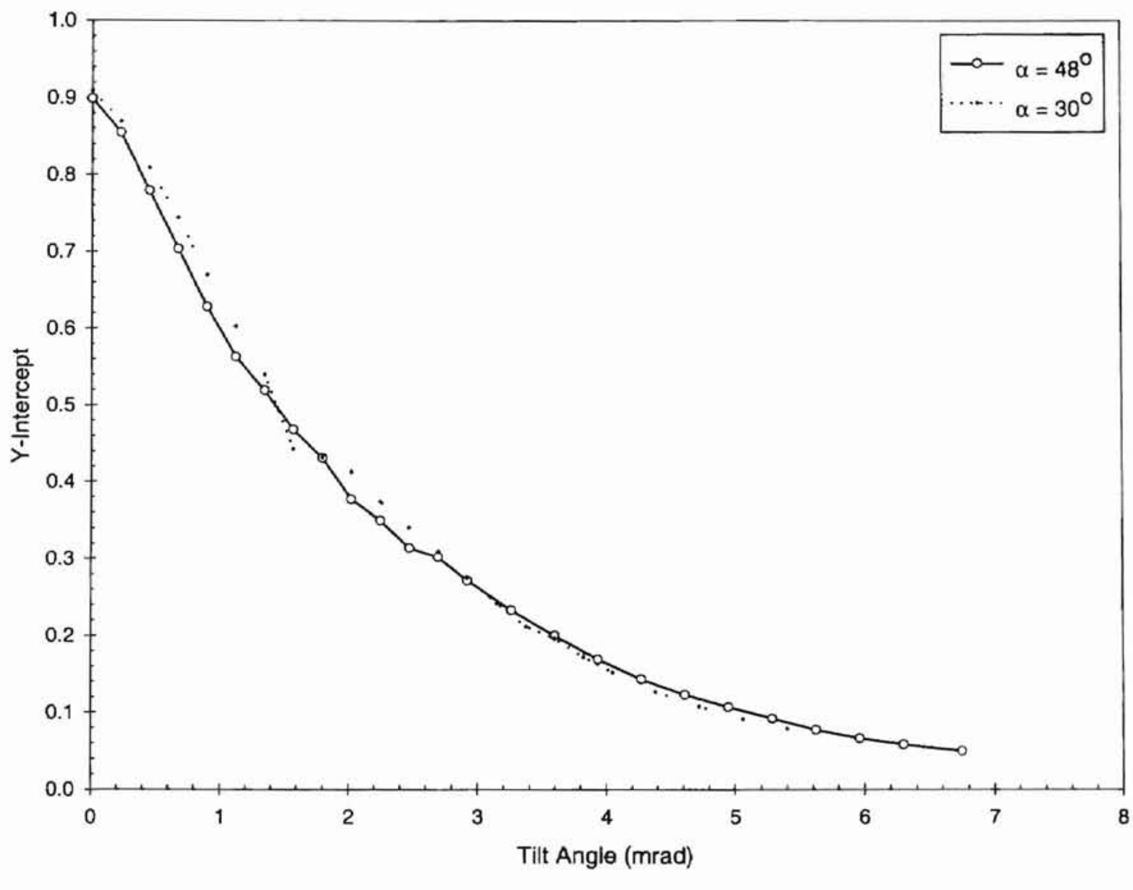

Figure 50: Y-intercept versus tilt angle mapping for 0.098 μm particles for the flowing case. The volume fraction is 0.86 percent. The flow rate is 100 percent. Two different α angles are compared here, viz., 48° and 30° (corresponding scattering angles are 112° and 135°). Data corresponds to experiments 106 and 109.

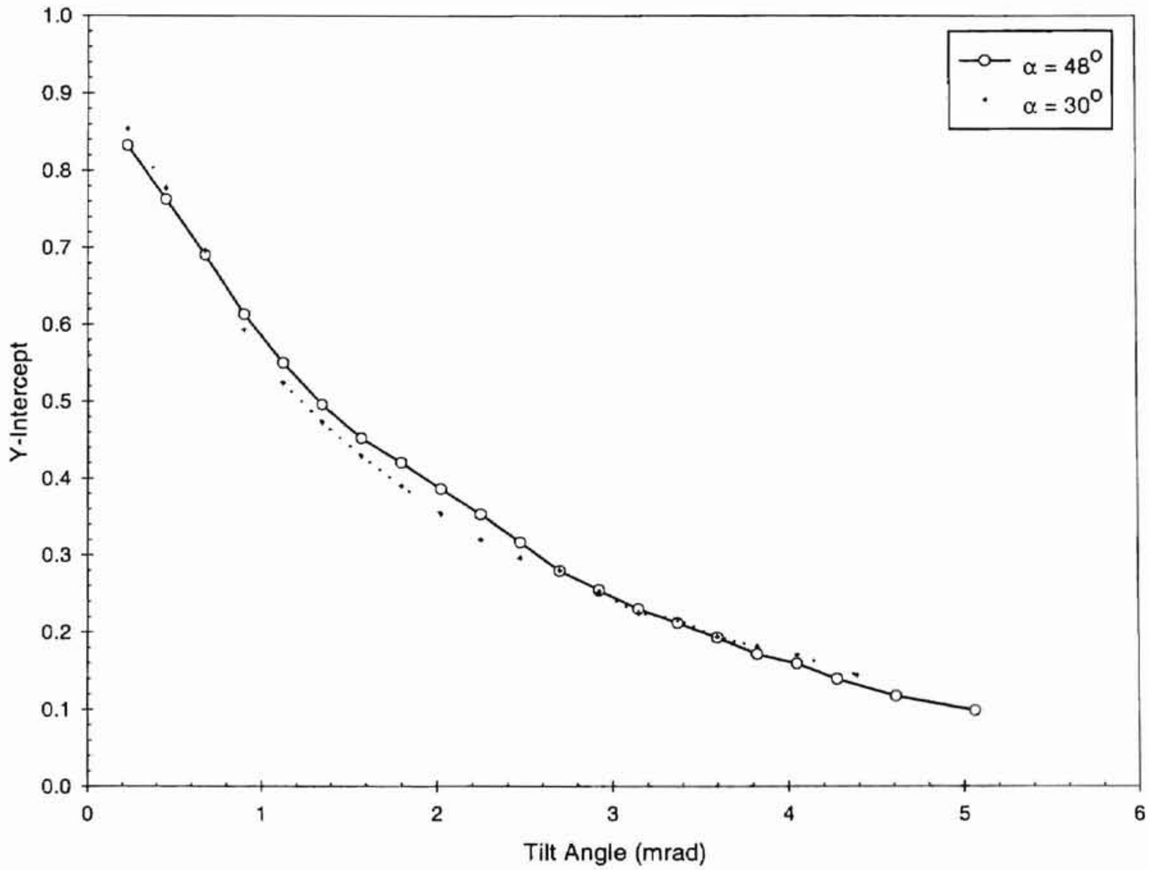

Figure 51: Y-intercept versus tilt angle mapping for 0.203 μm particles for the flowing case. The volume fraction is 0.20 percent. The flow rate is 100 percent. Two different α angles are compared here, viz., 48° and 30° (corresponding scattering angles are 112° and 135°). Data corresponds to experiments 112 and 114.

APPENDIX IV

Program to Run the Stepper Motors for the Laser and Detector Arms in the Flowing Experimental Setup

```
/* ########################################################################

                    STEPPER MOTOR DRIVER PROGRAM

  WRITTEN BY SANJAY SUNDARESAN ON 12/9/1998 - EDITED LAST 02/02/1999

                    FILE MOTOR.C

######################################################################## */

#include <stdio.h>    // INCLUDE STANDARD C LIBRARIES
#include <math.h>
#include <conio.h>

void motor_control (int,int);  // DECLARING THE MOTOR CONTROL FUNCTION

void main (void)        // MAIN PROGRAM DRIVER FUNCTION STARTS
{
    int dirntop, dirnbottom;
    float degreestop, degreesbottom, reftopmot, refbotmot, stepstop, newstepstop,
          stepsbottom, newstepsbottom;
    FILE *topmot, *botmot;        // DECLARING INPUT FILES

    topmot = fopen("topmotd.dat","r");     // OPEN FILES IN READ MODE
    botmot = fopen("botmotd.dat","r");

    fscanf(topmot,"%f",&reftopmot);  // READ REFERENCE DEGREES FOR
    fscanf(botmot,"%f",&refbotmot);  // TOP & BOTTOM MOTORS FROM FILE

    fclose(topmot);             // CLOSES FILES
    fclose(botmot);

    topmot = fopen("topmotd.dat","w");  // OPENS FILES IN WRITE MODE
    botmot = fopen("botmotd.dat","w");

     // PRINT TO SCREEN AND GET VALUES

    printf("\n ************************************************ \n");
    printf("DIRECTION CONVENTIONS:LEFT OF REFERENCE IS NEGATIVE \n
");
```

```
printf("\n                RIGHT OF REFERENCE IS POSITIVE \n");
printf("\n ************************************************** \n");

printf("\n       TOP (DETECTOR ARM) STEPPER MOTOR ");
printf("\n Enter the position in degrees required [negative please]: \n");
scanf("%f",&degreestop);        // READ DEGREES TOP
printf("\n ************************************************ \n");
printf("\n       BOTTOM (LASER ARM) STEPPER MOTOR ");
printf("\n Enter the position in degrees required [positive please]: \n");
scanf("%f",&degreesbottom);  // READ DEGREES BOTTOM
printf("\n ************************************************ \n");

// CALCULATES THE NUMBER OF STEPS REQD. @ 0.9 DEG/STEP
// FOR TOP (DETECTOR ARM)

stepstop = (degreestop - reftopmot) / 0.9;
if (stepstop >= 0.0)
    stepstop = stepstop + 0.5;
else if (stepstop < 0.0)
    stepstop = stepstop - 0.5;
        newstepstop = stepstop;

if (stepstop <= 0)     // IF NEEDED TO REACH A MORE NEGATIVE ANGLE,
{                      // GO CLOCKWISE
    stepstop = -1 * stepstop;
    dirntop = 2;
}
else if (stepstop > 0)      // IF NEEDED TO REACH A LESSER NEGATIVE
    dirntop = 3;            //  ANGLE, GO COUNTERCLOCKWISE

// FOR BOTTOM (LASER ARM)
stepsbottom = (degreesbottom - refbotmot) / 0.9;
if (stepsbottom >= 0.0)
   stepsbottom = stepsbottom + 0.5;
else if (stepsbottom < 0.0)
   stepsbottom = stepsbottom - 0.5;
newstepsbottom = stepsbottom;
if (stepsbottom <= 0)    // IF NEEDED TO REACH A LESSER POSITIVE
{                        // ANGLE, GO CLOCKWISE
   stepsbottom = -1 * stepsbottom;
   dirnbottom = 12;
}
else if (stepsbottom > 0)        // IF NEEDED TO REACH A MORE
   dirnbottom = 8;      // POSITIVE ANGLE, GO COUNTERCLOCKWISE

// CALL THE STEPPER MOTOR CONTROL FUNCTION
motor_control(stepstop,dirntop);        // TOP MOTOR
```

```
        motor_control(stepsbottom,dirnbottom);        // BOTTOM MOTOR

        // THE NEW POSITIONS BECOME THE REFERENCE
        newstepstop = (int)newstepstop;
        newstepsbottom = (int)newstepsbottom;
        reftopmot = reftopmot + (newstepstop * (float)0.9);
        refbotmot = refbotmot + (newstepsbottom * (float)0.9);

        // REWRITE THE NEW POSITIONS TO THE FILES
        fprintf(topmot,"%f",reftopmot);
        fprintf(botmot,"%f",refbotmot);

        fclose(topmot);                               // CLOSES FILES
        fclose(botmot);
}

/* ################################################################ */

//      CONTROL FUNCTION THAT DRIVES THE STEPPER MOTORS

void motor_control (int steps, int dirn)
{
        int stepcount = 1;
        long pulsecount;        // CREATES A SQUARE WAVE MOTION TO MAKE
                                // THE MOVEMENT SMOOTH
        _outp(0x2a3,0x80);      // DECLARING THE OUTPUT TO DATA
                                // ACQUISITION BOARD FUNCTION

// GIVING IT THE DIGITAL INPUT/OUTPUT PORT ADDRESS
        while (stepcount <= steps)
        {
             _outp(0x2a0, dirn);        // SENDS A HIGH PULSE
             for (pulsecount = 1; pulsecount <= 110000; pulsecount++); // MAINTAINS
                                                                        // A HIGH PULSE
             _outp(0x2a0,0);            // SENDS A LOW PULSE
             for (pulsecount = 1; pulsecount <= 110000; pulsecount++); // MAINTAINS
                                                                        // A LOW PULSE
              stepcount = stepcount + 1;
        }
}

/* ################################################################ */
```

VITA

Sanjay Sundaresan

Candidate for the Degree of

Master of Science

Thesis: MULTIPLE SCATTERING SUPPRESSION APPLIED TO PARTICLE SIZING IN NON-FLOWING AND FLOWING MEDIA

Major Field: Mechanical Engineering

Biographical:

Personal Data: Born in Calcutta, India, November 08, 1976. The son of Sundaresan Viswanathan and Vimala Sundaresan.

Education: Graduated from the University of Kerala, Trivandrum, India in May 1993; received Bachelor of Engineering degree in Mechanical Engineering from Manonmaniam Sundaranar University, Tirunelveli, India in May 1997. Completed the requirements for the Master of Science Degree at Oklahoma State University in December 1999.

Experience: Seagate Technology Inc., Mechanical Design Engineer (July 1999 / Present).

Professional Memberships: Associate Professional Member of the American Society of Mechanical Engineers, Member of The Honor Society of Phi Kappa Phi.